Stony Brook University

Doctoral Dissertation

Waveguide quantum electrodynamics, ultracold matter waves, and complex analysis: a modern study of spontaneous emission

---

Author:
Alfonso Lanuza

Supervisor:
Prof. Dominik Schneble

A dissertation submitted to the Graduate School
in partial fulfillment of the requirements for the degree of
Doctor of Philosophy in Physics
in the
Department of Physics and Astronomy

Ultracold atoms lab

August 2024

Committee Recommendation

Alfonso LANUZA

We, the dissertation committee for the above candidate for the Doctor of Philosophy degree, hereby recommend acceptance of this dissertation.

Dominik SCHNEBLE – Dissertation Advisor
Professor, Department of Physics and Astronomy

Tzu-Chieh WEI – Chairperson of Defense
Professor, Yang Institute of Theoretical Physics
and Department of Physics and Astronomy

Jesús PÉREZ RÍOS – Committee Member
Assistant Professor, Department of Physics and Astronomy

Francesco CICCARELLO – External Committee Member
Associate Professor, Department of Physics and Chemistry,
University of Palermo

This dissertation is accepted by the Graduate School.

Celia MARSHIK
Dean of the Graduate School

STONY BROOK UNIVERSITY

Abstract

Atomic, molecular, and optical physics
Department of Physics and Astronomy

Doctor of Philosophy in Physics

Waveguide quantum electrodynamics, ultracold matter waves, and complex analysis: a modern study of spontaneous emission

by Alfonso LANUZA

The use of matter waves in lieu of photons constitutes a new and promising platform for studying waveguide quantum electrodynamics (wQED). In wQED, one or more quantum emitters (QEs) are coupled to a waveguide that propagates photons. The matter-wave analog switches the roles of matter and light by making use of ultracold atoms trapped in state-dependent optical lattices with the capacity to act as QEs (in the form of lattice wells) or waveguides for the atoms (in the form of lattice tubes). By modifying their internal state with a microwave, the atoms can be trapped in the wells or freely travel along the tubes as spontaneously emitted matter waves.

The introduction of this experimental platform addresses multiple needs in wQED, establishing a pathway for fundamental studies of light-matter interactions: it provides a tunable geometry with identical equally-spaced QEs, controllable initial states, no emitter decay to modes outside of the waveguide, methods to measure the quantum state of both emitters and the emission, and a coupling between the QEs and the waveguide that can be varied between the weak and strong regime. But most remarkably, as matter waves are several orders of magnitude slower than photons, they are an ideal candidate for the real-time measurement of the so-called "non-Markovian dynamics", that break the assumption that QEs radiate waves that are irreversibly lost to the waveguide. The slow matter waves can indeed be reabsorbed by the same or an adjacent QE before they escape, or even become bound to the emitters in a dynamical equilibrium between being emitted and reabsorved.

This dissertation integrates recent experimental advancements in matter-wave wQED with a theoretical framework that employs complex analytical techniques to characterize these and other wQED systems.

To my beloved family

"The shortest path between two truths in the real domain passes through the complex domain."

-Jacques Hadamard [1]

"...in the same way we will not consider the spaces or the shortest lines, but those which can be traveled most easily, most conveniently and in the shortest time."

-Pierre de Fermat, about the study of light [2]

Contents

List of Figures

List of Abbreviations

1D	**One**-**D**imensional
APS	**A**merican **P**hysical **S**ociety
BEC	**B**ose-**E**instein **C**ondensate
BH	**B**ose-**H**ubbard
BHM	**B**ose-**H**ubbard **M**odel
BIC	**B**ound **S**tate **I**n the **C**ontinuum
BS	**B**ound **S**tate
BW	**B**loch **W**ave
BZ	**B**rillouin **Z**one
cQED	**c**avity **Q**uantum **E**lectro**d**ynamics
DoS	**D**ensity **o**f **S**tates
FGR	**F**ermi’s **G**olden **R**ule
GWF	**G**aussian **W**annier **F**unction
HOL	**H**armonic **O**scillator **L**ength
IT	**I**nverse **T**ransform
LHS	**L**eft-**H**and **S**ide
LP	**L**ower **P**olariton
M	**M**arkovian
MI	**M**ott **I**nsulator
MOT	**M**agneto-**O**ptical **T**rap
MW	**M**atter **W**ave
PDR	**P**arabolic **D**ispersion **R**elation
p	**p**ole
qBIC	**q**uasi-**B**ound **S**tate **I**n the **C**ontinuum
QE	**Q**uantum **E**mitter
QED	**Q**uantum **E**lectro**d**ynamics
RHS	**R**ight-**H**and **S**ide
SB	**S**ingle **B**and
SBU	**S**tony **B**rook **U**niversity
SDOL	**S**tate-**D**ependent **O**ptical **L**attice
SE	**S**chrödinger **E**quation
SF	**S**uper**F**luid
SP	**S**inusoidal **P**otential
sR	**s**ub**R**adiant
SR	**S**uper**R**adiant
TDS	**T**imed **D**icke **S**tate
TM	**T**oeplitz **M**atrix

TSE	**T**ransformed **S**chrödinger **E**quation
ToF	**T**ime **o**f **F**light
TOP	**T**ime-**O**rbiting **P**otential
UP	**U**pper **P**olariton
wQED	**w**aveguide **Q**uantum **E**lectro**d**ynamics
WS	**W**igner-**S**eitz
WWH	**W**eisskopf-**W**igner **H**amiltonian
XODT	**crossed O**ptical **D**ipole **T**rap

Physical Constants and Characteristic Quantities

Atomic mass of ^{87}Rb	$m = 1.443\,153\,015\,5(2) \times 10^{-25}\,\mathrm{kg}$
Bloch period	$\tau_B = 2\pi\hbar/mgd = 1.186(2)\,\mathrm{ms}$
Bohr radius	$a_0 = 5.291\,772\,109\,03(80) \times 10^{-11}\,\mathrm{m}$
Gravitational acceleration	$g = 9.80(3)\,\mathrm{m/s^2}$
Interemitter distance	$d = \lambda_z/2 = 3.9505(1) \times 10^{-7}\,\mathrm{m}$
Metastable “blue” hyperfine state of ^{87}Rb	$\lvert b\rangle = \lvert F = 2, m_F = 0\rangle$
Metastable “red” hyperfine state of ^{87}Rb	$\lvert r\rangle = \lvert F = 1, m_F = -1\rangle$
Optical trap frequency	$\omega_z = 2\pi \times 0.082(8)\,\mathrm{kHz}$
Recoil energy	$E_\mathrm{r} = \hbar\omega_\mathrm{r} = 2.4367(1) \times 10^{-30}\,\mathrm{J}$
Recoil frequency	$\omega_\mathrm{r} = \hbar k_\mathrm{r}^2/2m = 2\pi \times 3.6774(2)\,\mathrm{kHz}$
Recoil momentum	$k_\mathrm{r} = 2\pi/\lambda_z = 7.9524(2) \times 10^{6}\,\mathrm{m}^{-1}$
Reduced Planck’s constant	$\hbar = 1.054\,571\,817 \times 10^{-34}\,\mathrm{J\,s}$ (exact)
State-selective laser wavelength	$\lambda_z = 7.9010(2) \times 10^{-7}\,\mathrm{m}$
Trapping laser wavelength	$\lambda_\perp = 1.064(1) \times 10^{-6}\,\mathrm{m}$

Acknowledgements

First, I would like to extend my deepest gratitude to my advisor, Dominik Schneble, whose mentorship and guidance have been instrumental in my growth as a researcher. From the very beginning, Dominik has given me the freedom to explore and develop as a scientist in a way that felt natural to me, while also encouraging my theoretical interests. His exceptional clarity on a wide array of atomic physics and ultracold atom concepts and techniques, along with his characteristic attention to detail, has been invaluable and continues to influence my work. Dominik's presence in the lab has been a constant source of support, always keeping me focused and eager to discuss results, even in their preliminary stages. I am profoundly grateful that Dominik took a chance on me, helping me develop as a full-fledged physicist.

I'm so thankful to my senior labmates, Michael Stewart (or Mike) and Joonhyuk Kwon, who taught me how to operate an ultracold atoms laboratory, and to my fellow Ph.D. labmates, Youngshin Kim and Hongyi Huang, who shared much of this journey with me. From the first time that I entered the lab, Mike's sketches, mixed doodles, and handwritten integrals caught my eye and instilled a sense of familiarity in me, playing a significant role in my decision to join the lab. Mike has a like-minded sense of beauty in mathematics and their physical expression in the lab, a talent for teaching and mentoring borne from his empathy and experience, and his research style has been a firm guide for my own. This also extends to his interaction with Joon, who is a fantastic experimentalist. Joon's ability to navigate the chaos of the lab as if it were the most natural thing in the world is fascinating, which he compliments with a comparable amount of hard work and perseverance. Youngshin has been my Joon. I cannot imagine a better labmate: Youngshin's vast and interdisciplinary knowledge, his hard work, brightness, and efficiency make him an ideal researcher. I cannot think of something he cannot do fast yet meticulously. Furthermore, when you take Youngshin outside of his comfort zone (the lab) you can enjoy a surprisingly adventurous and funny friend, as I did between alligators and spaceships in Orlando or between Roman mosaics, Archimedes heritage, flash floods, and even volcano eruptions in Sicily. I can see many of his good traits being passed down to Hongyi, who is also a well-rounded researcher and a good friend. Hongyi's inquisitive mind, dedication, and disposition make him an excellent learner who has quickly become a reliable leading figure in the lab.

I thank Prof. Tzu-Chieh Wei and Yabo Li for systematically dissecting new papers with us. I am thankful to Martin G. Cohen for his constant disposition to help. To my friend Gabriel Cardoso and his Ph.D. advisor Prof. Alexandre Abanov, thank you for always being open to discussing far-out ideas. I am very grateful to Prof. Ángel Ballesteros (University of Burgos) and Dr. Alejandro González Tudela (Institute of Fundamental Physics, CSIC, Madrid) for their recent support and advice. To the other AMO professors Harold J. Metcalf, Jesús Pérez Ríos, Thomas Weinacht, Eden Figueroa, and Thomas Allison, as well as their students, thank you for composing such an engaging community, where helping each other with worldwide top-notch experiments can be interleaved with sharing a Friday meal, a barbecue, a walk in the park, a violin concert, playing soccer, laughing together or procrastinating collectively.

To all the other friends that I was lucky to make during this long journey: my undergrad friends, the ones who started the Ph.D. with me, the ones who joined along the way, my housemates, my Fulbright fellows, past office mates, and neighbors... you deserve my thanks the most but I cannot mention you all. You are just too many! I only hope that this life intertwines our paths once more.

I extend my heartfelt gratitude to the members of my dissertation committee: Dominik, Tzu-Chieh, Jesús, and Francesco Ciccarello (University of Palermo). Their comprehensive review of this manuscript, drawing on their vast and diverse expertise, has been invaluable.

Last but not least, I would like to thank my lovely family for their unconditional support.

During my Ph.D. time, I have been supported by several sources. In particular, I would like to thank the U.S. National Science Foundation (Grants No. PHY-1912546, and PHY-2208050) and the Ramón Areces Foundation (co-sponsoring a Spain-US Fulbright Grant).

Chapter 1

Introduction

The history of light [3] unfolds through different civilizations and epochs, starting with the ancient Greeks[1] who laid the groundwork for later advancements in optics and astronomy. The Islamic Golden Age[2] saw significant advancements by scholars like Alhazen in optics, including the principles of reflection and refraction. Starting in the 16th century, the Scientific Revolution brought about pivotal discoveries by figures such as Copernicus, Kepler, Descartes, Fermat, Huygens, and Newton, shaping our comprehension of light. Whether light behaved as a particle or a wave was a central point of contention between scholars, with the latter consolidating its prominence in the second half of the 19th century after Maxwell's theory and Hertz's experiments on electromagnetic waves. The 20th century ushered in revolutionary theories in physics, including quantum mechanics and relativity, further illuminating the very nature of light. The developments that followed the elucidation of the wave-particle duality of light, such as the discovery of laser technology, entanglement, and the exploration of optical fibers for communication revolutionized both fundamental physics and practical applications in optics and photonics. Each era built upon the knowledge of its predecessors, culminating in a comprehensive understanding of light across various disciplines.

1.1 A quantum theory of light

The concept of a black body in a radiative equilibrium was introduced by Gustav Kirchhoff in 1860 based on rather simple arguments. Remarkably, this feat preceded the discovery of the electromagnetic nature of light, that light carries energy and momentum or that accelerated charges emit and absorb radiation. It wasn't until 1900 that Planck found a formula that perfectly describes the full black-body spectrum [4], even at ultraviolet frequencies. He did so by modeling the walls of the cavity as a collection of one-dimensional harmonic oscillator antennas that possessed not a continuous but rather a discrete set of energies. As he would later describe it, this was "an act of desperation" [3] that, however, marked the birth of quantum mechanics. The idea that the same phenomenon could be expected if the radiation inside the black body was an ideal gas of free particles with an energy proportional to their frequency came from a young Albert Einstein just 5 years

---

[1] 800 BC to 200 AD, centered in Athens and then Alexandria but also extending to Anatolia, Syria, and Egypt.

[2] 8th to 13th centuries, with centers in Baghdad and Cordoba.

later. His explanation of the photoelectric effect [5] was meant as an argument to reinforce this conclusion, thus fathering the concept of a light quantum. The modern term "photon" was later coined by Gilbert N. Lewis in 1926 [6], although its precise meaning differed from Einstein's light quantum and is still a source of controversy [7].

In 1927, Paul Dirac took another foundational step in the quantization of light [8] by introducing the idea that every frequency mode in an electromagnetic wave can be interpreted and quantized as a simple harmonic oscillator. Soon after, Weisskopf and Wigner [9] used Dirac's newfound theory to calculate exponential decay rates in spontaneous emission processes. In early semiclassical models, the idea of an energetic vacuum that could 'jostle' an excited atom into emitting a photon was considered the fundamental source of noise and dephasing [3].

In 1935, Einstein, Podolsky, and Rosen [10] raised concerns about the seemingly paradoxical no-separability of quantum mechanical states. Their proposal questioned the completeness of quantum mechanics and several theories, known as "hidden variable theories" [11], aimed to amend this. However, John Bell thought otherwise and came up with a famous set of inequalities [12] that any theory of hidden variables –unlike quantum mechanics– should satisfy. A version of these inequalities [13] was violated for the first time with photons emitted in an atomic cascade of calcium [14]. In recent times, photon entanglement has led to multiple developments such as the creation of photonic cat states [15] or, remarkably, computational advantage in photon-based quantum computers over regular ones [16].

In 1946, Purcell observed an enhancement in the decay rate of atoms by placing them in a cavity featuring a modified vacuum [17]. Moreover, by sharing the same vacuum, nearby emitters no longer emit independently, but collectively. This realization allowed Dicke in 1954 to predict that a collection of nearby excited atoms can "superradiate a burst of light" [18]. Another dramatic consequence of the quantum vacuum was the discovery Casimir force [19] that two neutral conducting plates feel due to their modification of the quantum vacuum. Nowadays, cavity quantum electrodynamics (cQED) is a thriving field, with famous contributions from Walther [20], Haroche [21], Kimble [22], or Wineland [23].

In 1956, R. Hanbury Brown and R. Q. Twiss demonstrated an interferometer that they originally developed to measure the tiny angular size of stars against artificially created light by a mercury arc [24]. Unlike conventional interferometers that focus on measuring the phase correlations of two light paths, Hanbury Brown and Twiss measured the correlations in intensity finding positive correlations (photon bunching) when the detectors were close to one another. This experiment raised debate on the quantum statistics of photonic sources, with important contributions from multiple physicists such as Roy J. Glauber or Leonard Mandel [25] who later used these ideas to develop a quantum theory of optical coherence [26, 27] that could describe the quantum state and corresponding statistics of the newfound laser light. This technological development, achieved first in 1955 by Gordon *et al.* [28] in an ammonia maser (microwave amplification by stimulated emission of radiation), was extended [29, 30] to the optical domain, thus obtaining a laser (light amplification by stimulated emission of radiation). The invention of the laser has revolutionized many areas, such as spectroscopy [31], interferometry [32], remote sensing [33], atomic manipulation [34], or the investigation of non-linear optical phenomena [35, 36], finding applications in practically every empirical science.

1.2 Quantum electrodynamics in waveguides

The electromagnetic vacuum in cQED is discretized by the harmonics within the cavity plates. Consequently, if the cavity is perfectly isolated, the decay dynamics of atoms inside the cavity exhibit periodic behavior: the emitted photon reflects off the cavity mirrors and is subsequently reabsorbed by the atom. In contrast, atoms in free space experience irreversible decay due to their coupling with a three-dimensional continuum. A hybrid approach, achieving strong coupling to an open quantum system with minimal dissipation, can be realized by confining light with mirrors in two transverse directions while leaving the remaining dimension open, thereby creating a waveguide.

Understanding spontaneous emission in modified vacua is particularly intriguing when the electromagnetic fields form a band structure, as energy bands possess both continuous and discrete characteristics. Although V. P. Bykov pioneered these concepts in 1975 [37], they did not gain widespread recognition in the West –presumably due to the Cold War– until decades later through the works of Sajeev John [38–43].

These photonic band structures are present in photonic crystals [44], such as waveguides with a periodic index of refraction. When one quantum emitter resonates inside one of the band gaps, the emitted photon cannot propagate [45] and remains localized around the emitter as an evanescent wave. This photon-emitter bound state is robust to dephasing [46] and, if it is sufficiently large to overlap with another emitter, the photon can be reabsorbed, providing a dissipation-free mechanism for interactions between quantum emitters [47, 48].

Initially motivated by applications in laser technologies, these systems have garnered significant fundamental interest, leading to the emergence of a distinct field known as waveguide quantum electrodynamics (wQED). Current research topics in this field include the role of the waveguide's dimensionality [49], the presence of one [50] or multiple energy bands [51], topological effects [52], emission by "giant atoms" [53–55], the influence of emitter arrangements [51, 56, 57], the delay of radiation traveling between emitters [58–63], and multi-photon dynamics [47, 50, 61, 63–70].

1.3 Experimental platforms

There are several experimental platforms for the research of wQED [71]. Every platform has strong and weak points, but they form a substantially complete picture of the field together. Here we describe them briefly.

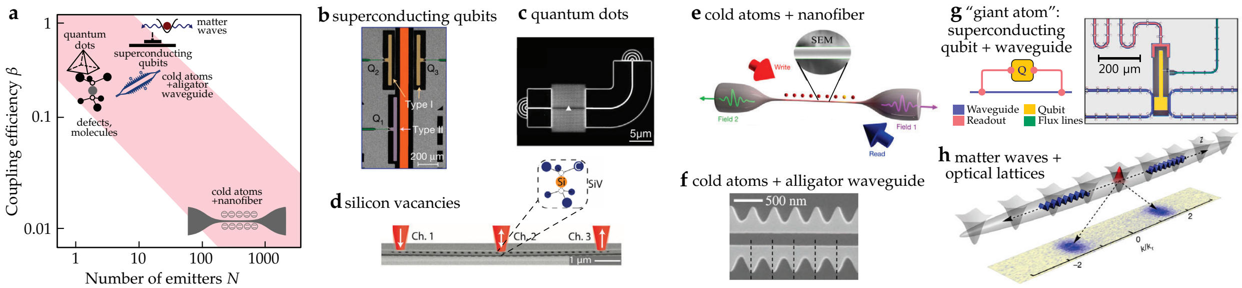

FIGURE 1.1: **a,** Comparison of a waveguide coupling efficiency β and number of emitters N for *different platforms of waveguide quantum electrodynamics*. **b-h,** Schematics of different platforms. Figure panels **a**-**h** are respectively reproduced from Refs. [71–78] with permissions from A. N. Poddubny, the APS, Springer Nature, and the American Association for the Advancement of Science; the matter-wave platform (**h**) is contextualized by including it in **a**.

- *Superconducting qubits* [79]. They are made with superconducting electrical circuits carrying Cooper pairs at microwave frequencies. Contrary to popular belief, the main reason why superconducting circuits are cooled at $\sim 10\,\mathrm{mK}$ to reduce thermal noise and decoherence, rather than to make them superconducting [80]. Quantum emitters or qubits in this platform consist of LC circuits with a Josephson junction. The waveguide can be implemented with either microwave transmission lines [77] or surfaces hosting acoustic waves (phonons) [81]. They have the advantages of tunable couplings, individual qubit control, high coupling efficiencies[3] ($\beta \simeq 0.999$), and site resolution for measurements and state preparation. Moreover, liberties in the design of the circuit allow to couple the quantum emitters at several points along the waveguide, effectively realizing 'giant atoms' [77]. Their disadvantages are their noise, decoherence time, and that qubits are not entirely identical.

- *Quantum dots* [73, 82, 83]. This platform consists of depositing nanoscopic semiconducting particles on a nanophotonic waveguide. The particles -known as quantum dots- are small enough to discretize the energy levels of the electrons they host, acting as artificial atoms capable of absorbing and emitting single photons. The dot cannot absorb two photons or more due to Coulomb blockade. Quantum dots count with relatively high coupling efficiency to the waveguide ($\beta \simeq 0.99$), but producing identical quantum dots with a precise and regular placement along the waveguide is technically challenging. Furthermore, the states of the quantum dots cannot be directly manipulated or detected as they need to be accessed through the waveguide.

- *Vacancies in diamond waveguides*. Using focused ion beams, Silicon [74] or Germanium [84] vacancies can be implanted along a diamond waveguide. These diamond defects act as quantum emitters for the light. Vacancies are less tunable in frequency

---

[3] The coupling efficiency β of a QE is the ratio between the decay into modes inside the waveguide and the total decay of the QE, which also includes radiation outside the waveguide and the homogeneous nonradiative decay rate [71].

than quantum dots and present poorer coupling efficiencies ($\beta \sim 0.5$), but they are more uniform as all share a common molecular structure. Inhomogeneities still exist from the stochastic bunching of defects, changing the local environment of the vacancies.

- *Cold atoms*. A gas cloud of individual alkali atoms (like ^{87}Rb or ^{133}Cs) can be optically trapped near a fiber [75] or an alligator waveguide [76]. The trapping potential is done with strong lasers that are off-resonance with the atoms, so they don't partake in single-photon emission or absorption processes. Lowering the temperature in these systems helps trap the atoms and reduce their Doppler shift. Although these systems have the lowest coupling efficiencies ($\beta \sim 0.1$ or 0.01), thousands of atoms can act as perfectly identical quantum emitters. Moreover, an evanescent field optical lattice for the atoms can be conducted through the fiber [85] to tune the distance between atoms. These properties make the platform a strong candidate for the study of collective radiative effects such as inter-emitter retardation [86] or superradiant bursts [87].
- *Matter waves*. This platform switches the roles of matter and light, as if making full use of wave-particle duality, and employs optical-lattice wells as quantum emitters, optical-lattice tubes as waveguides, and atomic matter waves as radiation (see FIG. 1.1**h**). It was first proposed by de Vega *et al.* [88], further developed in Refs. [89, 90] and implemented by Krinner *et al.* [78] in our ultracold atoms lab at SBU. This platform stands out for having perfect coupling efficiency ($\beta = 1$), no thermal noise, extremely slow dynamics, a versatile control over the initial quantum states, being fully tunable (even while the experiments are taking place and over multiple parameter regimes), and simultaneously capturing the states of emitters and radiation. On the downside, atom-atom interactions limit the coherence of the experiments. All these properties make the matter-wave platform more suitable for studying non-Markovian dynamics [78, 91, 92].

1.4 About this dissertation

The aim of this work is three-fold. Firstly, we give a cursory explanation of the *matter-wave platform* to later present the results of our experiments. Secondly, we aim to describe and develop complex analytical techniques that allow an exact description of wQED systems. Thirdly, we seek a uniform and systematic analysis of wQED phenomena while tracing back their physical origins whenever possible.

This dissertation is structured as follows. Chapter 2 is dedicated to describing in depth the matter-wave platform. In 2.1 we explain how to ultracool atoms and in 2.2 we explain in detail how to execute wQED experiments using them. Chapter 3 is dedicated to the theory behind wQED. In 3.1, we present the Markovian emitter, in 3.2 we explain coupling-induced non-Markovain effects, we study the role of the emitter size in 3.3 and photonic band structure in 3.4, in 3.5 we look at array effects from multiple emitters, and in 3.6 we investigate the effects of multiple excitations. Chapter 4 is reserved for conclusions.

Chapter 2

Creation and manipulation of ultracold matter waves

In his doctoral dissertation of 1924 [93] and inspired by Planck and Einstein's ideas on the dual wave-particle nature of light, Louis De Broglie hypothesized wave-like properties for particles, challenging the classical view of matter. Experiments like electron diffraction [94, 95] soon confirmed his idea, solidifying wave-particle duality as a pillar of quantum mechanics.

Bose and Einstein's theoretical work [96] on bosonic statistics in 1924-25 laid the groundwork for Bose-Einstein condensates (BECs). These exotic states, where bosons colloquially occupy the same quantum state at ultracold temperatures, remained experimentally elusive for decades. Six decades later, pioneering laser cooling techniques [97] paved the way for the first BEC of rubidium atoms in 1995, achieved by Cornell and Wieman [98] and shortly thereafter by Ketterle [99] with sodium. These landmark experiments opened a new era, allowing for the manipulation of ultracold matter at the quantum level.

2.1 Preparation of a Bose-Einstein condensate

In this section, we explain in broad terms how we prepare BECs in our ultracold atoms lab, which is to date the only lab that has realized the matter-wave platform for wQED. This is by no means the state of the art in Bose-Einstein condensation [100–103], but it serves as an introduction to the elements involved in these experiments. For further technical details, see Ref. [104] or past PhD dissertations from our group [105–108].

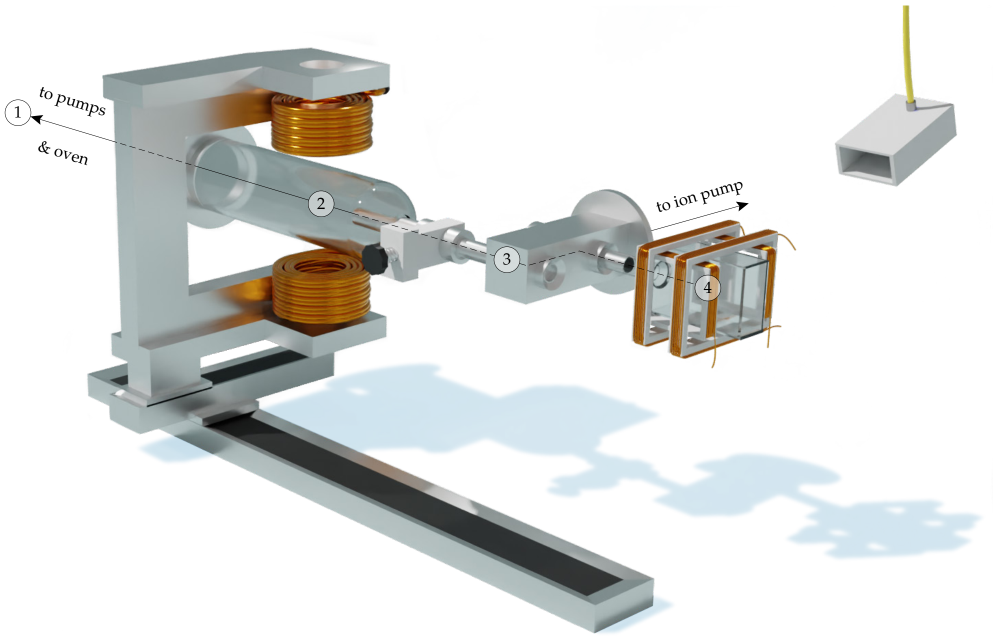

FIGURE 2.1: *Ultracooling process inside the vacuum chamber*. A broken ampoule with solid ^{87}Rb inside an oven (1) fills the vapor cell (2) with sublimated rubidium gas. A magneto-optical trap starts the cooling process, which continues after transport (3) to the ultra-high vacuum of the science cell (4), where evaporative cooling takes place until a BEC is formed. Adapted from [104]; the components are not to scale.

The cooling procedure consists of the following steps (see FIG. 2.1):

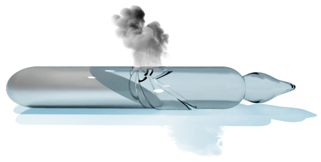

① The rubidium oven is a part of the vacuum chamber with a ^{87}Rb ampoule that was broken after creating the vacuum. ^{87}Rb sublimates at room temperature, but additional heating can be applied through small coils wrapped in aluminum foil for additional control of the vapor pressure ($\sim 10^{-8}$ mbar).

② The rubidium gas fills the vapor cell, where two large coils made of hollow-core copper tubing and six laser beams are activated to produce a magneto-optical trap (MOT). The coils run a strong current in anti-Helmholtz configuration and filtered water for cooling. The beams have the circular polarizations indicated in the right figure. Around 10^{10} atoms are trapped and Doppler-cooled to a few 100 µK in the MOT. Then, the coils are temporarily switched off to further cool the rubidium to $\sim$ 50 µK through optical molasses (Doppler and Sisyphus cooling).

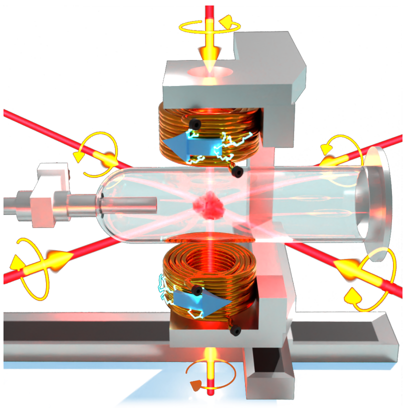

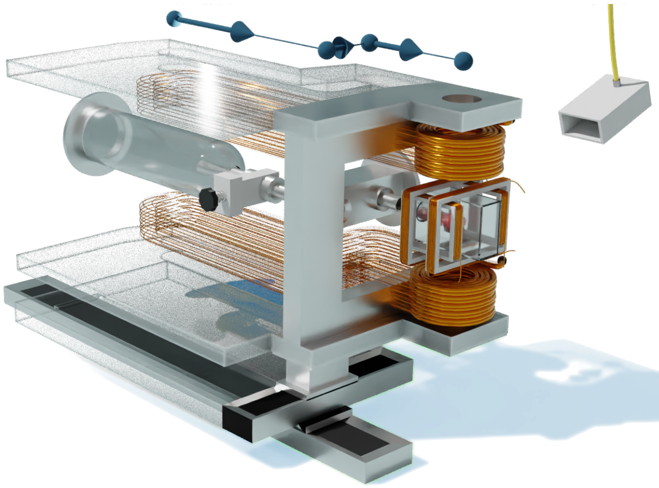

③ The rubidium cloud is transferred into a quadrupole magnetic trap and mechanically transported to the science cell, which is kept at an ultra-high vacuum ($\sim 10^{-12}$ mbar) and has additional coils used to realize a magnetic time-orbiting potential (TOP), and for fine control of the static magnetic bias field. In the TOP trap, the atomic cloud is brought close to quantum degeneracy using radio-frequency evaporation.

④ Inside the science cell, the atoms are transferred to a crossed optical dipole trap (XODT), created with two strong orthogonal laser beams. With a wavelength $\lambda_\perp$ of 1064 nm, the laser beams are detuned off resonance with the ^{87}Rb absorption spectrum so that they neither heat nor disturb the internal level structure of the atoms, but they are strong enough to hold the atoms in place by creating a harmonic trapping potential of frequency $\omega_z \sim 2\pi \times 60\,\mathrm{Hz}$. Then, the cloud is evaporatively cooled below the critical temperature (~100 nK) by lowering the depth of the XODT. Typically around 2×10^5 atoms or less survive this process.

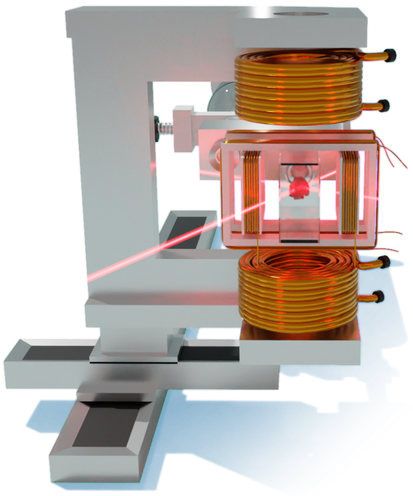

The temperature and momentum distribution of the atoms are measured through time-of-flight (ToF) pictures, which consist of absorption images of the atomic cloud as it falls and expands after switching off the XODT. The Bose-Einstein condensation is characterized by the appearance of a strong peak at zero momentum in the ToF pictures (see FIG. 2.2).

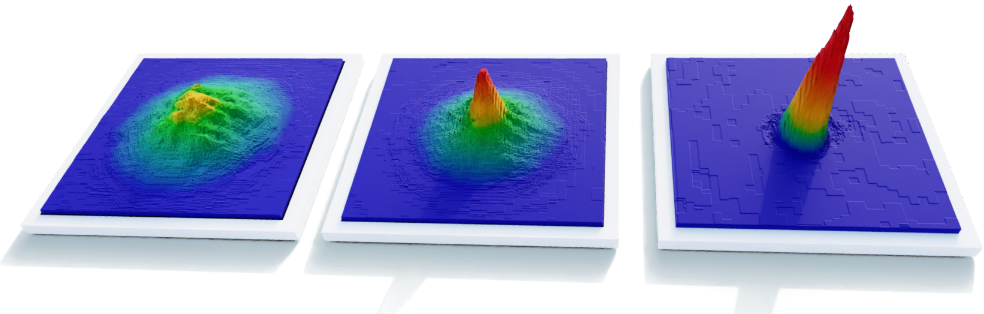

T=410 nK T=200 nK T=30 nK

FIGURE 2.2: *Bose-Einstein condensation*. ToF pictures of the ^{87}Rb atomic cloud at different temperatures. A purely thermal distribution (left) transforms into a bimodal distribution (center) with the appearance of a strong central peak, which represents the BEC and dominates the distribution at ultracold temperatures (right).

2.2 Experiments on matter-wave emission

2.2.1 State preparation

Depending on the particular experiment, the preparation of the initial state changes. In most cases, one starts by retroreflecting the XODT beams. This produces an optical lattice of vertical tubes that confine the atoms in 1D and increases the harmonic confinement ω_z. Then, an additional state-dependent optical lattice (SDOL [109]) is activated along the z direction. At a wavelength $\lambda_z = 790.0\,\mathrm{nm}$, ^{87}Rb atoms in the "blue" internal state $|b\rangle = |F=2, m_F=0\rangle$ do not feel the SDOL at all, while atoms that are in a "red" internal state $|r\rangle = |F=1, m_F=-1\rangle$ get trapped in the wells of a potential of the form $s_a E_\mathrm{r} \sin^2(k_\mathrm{r} z)$, where $E_\mathrm{r} = \hbar\omega_\mathrm{r} = (\hbar k_\mathrm{r})^2/2m$ is the recoil energy and $k_\mathrm{r} = 2\pi/\lambda_z$ is the recoil momentum of the lattice [51]. Tuning this wavelength, one can also generate a positive ($s_b E_\mathrm{r} \sin^2(k_\mathrm{r} z) > 0$) or negative ($s_b < 0$) potential for the blue atoms.

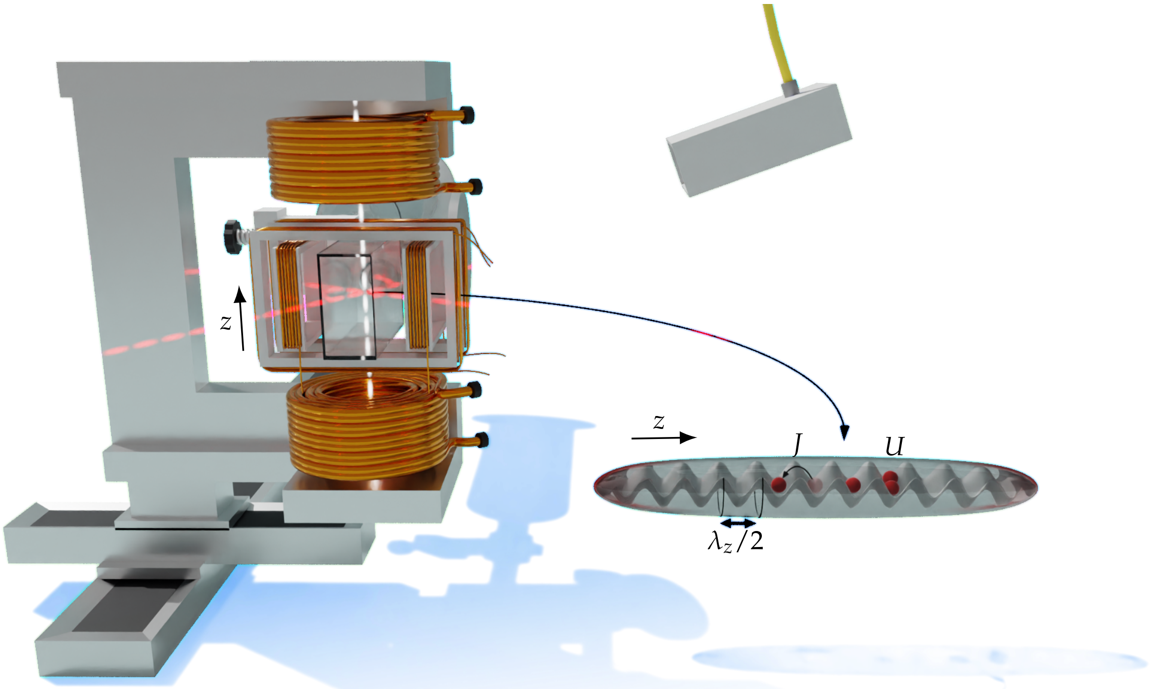

FIGURE 2.3: *Preparation of the QEs*. Optical lattices produce a Bose-Hubbard model inside isolated vertical tubes (typically represented horizontally) for the $|r\rangle$ hyperfine state of ^{87}Rb atoms.

This results in a 1D Bose-Hubbard model for the red atoms (see FIG. 2.3),

$$\hat{H}_\mathrm{BH} = \sum_j -\hbar J \hat{a}_j^\dagger \hat{a}_{j+1} - \mu \hat{n}_j + \frac{1}{2} U \hat{n}_j (\hat{n}_j - 1), \tag{BHM}$$

where $\hat{a}_j^{(\dagger)}$ is the annihilation (creation) operator of a red atom in lattice site j and $\hat{n}_j = \hat{a}_j^\dagger \hat{a}_j$ is the associated number operator [110]. The hopping rate and interaction energy for a

SDOL of depth $s_a \gg 1$ are

$$J = \frac{4\omega_\mathrm{r}}{\sqrt{\pi}} s_a^{3/4} e^{-2\sqrt{s_a}} \qquad \text{and} \qquad U = 4\sqrt{2\pi}\frac{\lambda_z a_{rr}}{\lambda_\perp^2} E_\mathrm{r} s_a^{1/4} s_\perp^{1/2}, \tag{2.1}$$

where the scattering length a_{rr} for $|r\rangle$-$|r\rangle$ collisions in ^{87}Rb is about a hundred times the Bohr radius a_0 [106]. Hence, by controlling the depth s_a of the SDOL and the depth $s_\perp$ of the transverse lattice (measured in its own recoil units) we can control J and U independently.

These lattice sites will represent quantum emitters in our experiment. In the case of bringing the BHM to a Mott-insulating regime with a single atom per site, the state of the system

$$\prod_j \hat{a}_j^\dagger |0\rangle \tag{2.2}$$

simulates a fully inverted array of QEs [92]. In the superfluid regime with negligible interactions ($U \ll J$), the M atoms distribute (each) uniformly over the N lattice sites in a macroscopically-populated timed Dicke state [111]

$$M!^{-1/2} \left(\hat{a}_{\phi,N}^\dagger\right)^M |0\rangle \qquad \text{where} \qquad \hat{a}_{\phi,N}^\dagger = N^{-1/2} \sum_{j=\lfloor 1-N/2 \rfloor}^{\lfloor N/2 \rfloor} e^{i\phi j} \hat{a}_j^\dagger \tag{TDS}$$

of zero phase lag ($\phi = 0$). This phase lag can be further controlled via Bloch oscillations: switching off the XODT momentarily for time t_B, the atoms feel the gravitational acceleration g but cannot fall due to the SDOL holding them in place. They do, however, acquire a lattice momentum $q = -2k_\mathrm{r} t_B / \tau_B$ where $\tau_B = 2\pi\hbar/(mgd) = 1.2\,\mathrm{ms}$ is the Bloch period and $d = \lambda_z/2$ is the interemitter distance. This establishes a constant phase lag $\phi = qd$ between the emitters that can be timed to the phase delay experienced by the matter waves traveling from one emitter to another [92].

Another possibility is to investigate the single excitation case by sieving off most of the atoms. For this purpose, $\sim 82\%$ atoms in the Mott insulating regime are transferred to an auxiliary hyperfine state $|F = 2, m_F = 1\rangle$ before removing them with resonant light on the D$_2$ cycling transition ($F = 2 \rightarrow F' = 3$) [78]. The remaining atoms are stochastically localized in single lattice sites with a low probability of having neighboring atoms nearby. Labeling the occupated site as $j = 0$ results in the state

$$\hat{a}_0^\dagger |0\rangle . \tag{2.3}$$

2.2.2 Time evolution

In experiments on matter-wave emission, time starts and stops by switching on and off the microwave (see FIG. 2.4). This is because the microwave couples the $|r\rangle$ and $|b\rangle$ states

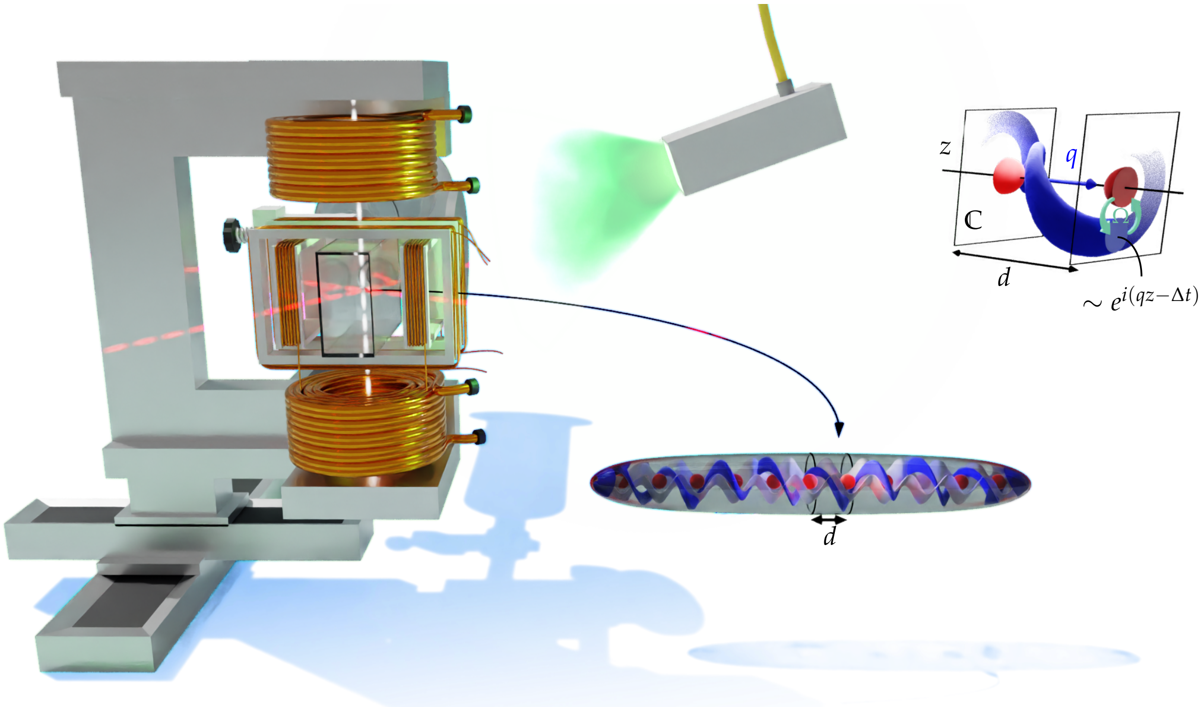

FIGURE 2.4: *Experiments on matter-wave emission.* A microwave antenna radiates (represented as a green light) over the science cell, inducing Rabi oscillations of frequency Ω between the red and blue states. In the illustrated case, microwave radiation with $\Omega = 0.6\omega_\mathrm{r}$ and detuned by $\Delta = 2.25\omega_\mathrm{r}$ has been acting for 200 µs on a timed Dicke state $\hat{a}^\dagger_{1.5k_\mathrm{r},11}\left|0\right\rangle$ (red balls) trapped in a SDOL of depths $s_a = 8$ and $s_b = 0$. The resulting radiation (in blue) is strongly directional and similar to a plane wave of momentum $q = 1.5k_\mathrm{r}$. The top-right inset shows the marked unit cell of the system amplified; the transverse section of the radiation represents its phase on the complex plane $\mathbb{C}$ resulting in a characteristic corkscrew shape. This shape helps visualizing how for a quantum plane wave a phase rotation (speed shades in the inset) is equivalent to having a linear momentum (blue arrow).

so that a red atom can become blue and be spontaneously emitted from the SDOL lattice well and a blue wave can become red and be spontaneously absorbed by the wells. This makes the lattice wells an ideal array of matter-wave QEs that are identical and equispaced. Since an atom needs to absorb a single microwave photon to be emitted, the microwave frequency detuning Δ from the resonance between the hyperfine states (including zero-point energies induced by different potentials) takes the role of emitter energy, $\hbar\Delta$. Similarly, the microwave power affects the Rabi frequency Ω of the $|r\rangle$-$|b\rangle$ oscillations, resulting in a vacuum coupling

$$g_{j,q} = \Omega \left\langle \varphi_j \middle| \psi_q \right\rangle / 2 \tag{2.4}$$

that accounts for the overlap between the Wannier state $\left|\varphi_j\right\rangle$ of the j-th red lattice site and the blue Bloch wave $\left|\psi_q\right\rangle$ of lattice-momentum q in the extended zone scheme, $q \in$

$(-\infty, +\infty)$. This establishes a Weisskopf-Wigner Hamiltonian

$$\hat{H}/\hbar = \sum_j \Delta \hat{a}_j^\dagger \hat{a}_j + \sum_q \omega_q \hat{b}_q^\dagger \hat{b}_q + \sum_{j,q} (g_{j,q} \hat{a}_j^\dagger \hat{b}_q + g_{j,q}^* \hat{b}_q^\dagger \hat{a}_j) \tag{WWH}$$

for the emission of matter waves whose dispersion relation ω_q depends on the blue lattice depth s_b. We adopt the convention of Bloch waves being normalized (even when they represent plane waves) to a single Brillouin zone (BZ), resulting in the explicit form $\sum_q \equiv \int_{-\infty}^{+\infty} \frac{\mathrm{d}q}{2k_\mathrm{r}}$ for the sum of modes [51]. We make the experiment insensitive to the residual harmonic confinement of the XODT by restricting the evolution times to be lower than 3 ms, corresponding to the quarter trap period $\pi/(2\omega_z)$.

A useful alternative to suddenly turning the microwave on is to do so adiabatically and excite an isolated state. In our system, these states correspond to evanescent matter waves bound to the QEs and for weak couplings ($0 < \Omega \ll \min_q |\Delta - \omega_q|$) their frequency, that dwells in the gaps of the dispersion relation ω_q, can be approximated by Δ. The adiabatic theorem [112] then states that the adiabatic excitation of these states is possible if

$$\dot{\Omega}/\Omega \ll \min_q |\Delta - \omega_q|. \tag{2.5}$$

In practice, however, a perfectly slow increase in parameters is never possible due to limiting factors like fluctuations of the magnetic field, drifts in laser power, or heating due to atomic interactions. Therefore, small contributions from other states are to be expected. As these manifest as oscillating deformations of the bound state distribution, a practical way to measure the bound states is to measure them after various holding times, corroborate that the distribution doesn't evolve significantly (an unequivocal sign that we have excited an eigenstate) and time-average the resulting distribution to minimize the effect of these deformations. This idea, proposed by the author and implemented in [91], serves a double purpose without increasing the amount of data-taking since averaging over multiple measurements is required anyway to reduce experimental uncertainties.

2.2.3 Measurement

To measure the state of the system, the existing optical lattices might be turned off suddenly for the sake of measuring the momentum distribution of the atoms in a ToF picture. This results in the matter waves' diffraction, manifesting as various separated peaks for Bloch matter waves $|\psi_q\rangle$. Doing so in a short pulse (Kapitza–Dirac diffraction [113]) is particularly useful for calibrating the lattice depths (s_a, s_b, and $s_\perp$) and, in case of them being too small, the process of switching on and off the lattices can be repeated periodically (Talbot-enhanced interferometry [114]) for higher accuracy.

Alternatively, the lattice depths can be reduced adiabatically to maintain the lattice momentum q of a Bloch wave up to the point when the lattice is no more and the lattice momentum becomes a linear momentum. The subsequent ToF picture reveals a single peak centered at q. This technique is known as "band mapping" and it allows taking ToF pictures in lattice-momentum space.

To further distinguish the internal state of the atoms, the quadrupole coils produce a magnetic field gradient that results in Stern-Gerlach separation [115] of the hyperfine states during ToF. Since the different hyperfine states of ^{87}Rb are energetically separated by a magnetically-induced Stark shift [116], these measurements can be complemented with microwave pulses that distribute the atomic population over unused hyperfine states for precise *in situ* magnetometry [117]. Furthermore, the ToF absorption imaging is also state-selective, to be able to separately detect $|r\rangle$ and $|b\rangle$ atoms[1].

---

[1] For more details, see method sections of either of Refs. [78, 92, 118].

Chapter 3

Waveguide quantum electrodynamics

Waveguide QED, which focuses on the interaction between photons propagating in a waveguide and localized quantum emitters [71], represents a novel paradigm for light-matter interactions within an open quantum system in which strong coupling, emitter size, bath structure, and delays can break the radiative conditions that emitters usually encounter in free space. This chapter studies these characteristics, which intertwine the excitations of the quantum emitters and the guided radiation modes to form complex photonic dynamics.

The work described in this chapter is derived from publications [51, 70, 90, 92, 118] produced by our group during my doctoral research. It is also influenced by earlier works from our group, specifically Refs. [78, 90]. Portions of the text in this chapter resemble or may replicate the original text from Refs. [51, 70] and the Appendix "Spectral structure and bound states in the continuum (BIC)" in [92] which were devised, calculated, and originally written by me. This replication is done with permission from all the co-authors.

3.1 The Markovian emitter

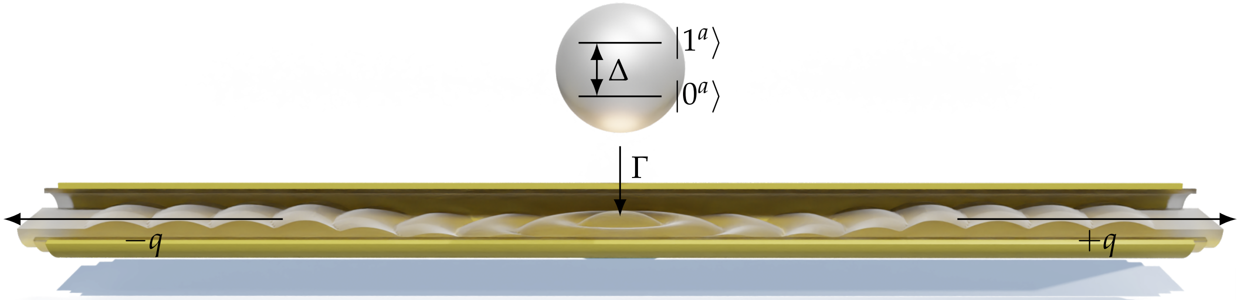

FIGURE 3.1: A *Markovian emitter* of energy $\hbar\Delta$ decays at rate Γ by emitting waves of quasimomentum $\pm q$ in a waveguide.

An early achievement of the quantum theory of light was the capacity to compute spontaneous decay rates [9], which escaped semiclassical theories. Here we review how this was achieved by considering a single quantum emitter of excitation energy $\hbar\Delta$ with a coupling g to a 1D waveguide that guides q-modes with a dispersion relation ω_q. The dynamical evolution of the system is given by the WWH for a single emitter,

$$\hat{H}/\hbar = \Delta \hat{a}^\dagger \hat{a} + \sum_q \left(\omega_q \hat{b}_q^\dagger \hat{b}_q + g\hat{a}\hat{b}_q^\dagger + g\hat{a}^\dagger \hat{b}_q \right) \tag{3.1}$$

where $\hat{a}^\dagger \equiv \hat{a}_0^\dagger$ and $\hat{a}_j^\dagger = |1_j^a\rangle \langle 0|$ are fermionic creation operators and $\hat{b}_q^\dagger = |1_q^b\rangle \langle 0| + \sqrt{2}|2_q^b\rangle\langle 1_q^b| + ...$ are bosonic ones. $\hat{H}$ conserves the number of excitations, simplifying the analysis tremendously. In particular, expanding the state of the system in a sub-basis for a single excitation

$$|\Psi(t)\rangle = A(t)\hat{a}^\dagger |0\rangle + \sum_q B_q(t)\hat{b}_q^\dagger |0\rangle \,, \tag{3.2}$$

the Schrödinger equation

$$i\hbar \frac{\partial}{\partial t} |\Psi\rangle = \hat{H} |\Psi\rangle \tag{SE}$$

in terms of these coefficients takes the form

$$\begin{cases} i\dot{A} = \Delta A + g\sum_q B_q \\ i\dot{B}_q = \omega_q B_q + gA \end{cases} \tag{3.3}$$

with $A(0) = 1$ and $B_q(0) = 0$ for an spontaneous emission process.

Working in terms of the corotating coordinates $e^{i\Delta t}A$ and $e^{i\omega_q t}B_q$, this can be rewritten as

$$\frac{\partial}{\partial t}\left(e^{i\Delta t}A(t)\right) = -\sum_q g^2 \int_0^t e^{i(\Delta-\omega_q)(t-t')} e^{i\Delta t'} A(t')\mathrm{d}t'. \tag{3.4}$$

The Weisskopf-Wigner approximation consists of replacing $e^{i\Delta t'}A(t') \to e^{i\Delta t}A(t)$ on the RHS and is based on the assumption that this corotating coordinate doesn't change significantly during the interval $t' \in [0,t]$. This is a type of Markovian approximation because the dynamics at t are considered to depend only on the conditions at t, and not on the whole trajectory of $A(t')$ for all $0 \le t' \le t$. This is often colloquially expressed as *the system not having memory of the past* and is also associated with the irreversibility of the spontaneous emission process.

With this approximation, the equation becomes

$$\frac{\partial}{\partial t}\left(e^{i\Delta t}A(t)\right) = -2\pi g^2 e^{i\Delta t} A(t) \sum_q e^{i(\Delta-\omega_q)t/2} \frac{t\,\mathrm{sinc}((\Delta-\omega_q)t/2)}{2\pi} \tag{3.5}$$

or in terms of the density of states,

$$\rho(\omega) = 2\mathrm{d}q(\omega)/\mathrm{d}\omega, \tag{DoS}$$

it becomes

$$\frac{\partial}{\partial t}\left(e^{i\Delta t}A(t)\right) = -\frac{\pi g^2 e^{i\Delta t}A(t)}{2k_{\mathsf{r}}}\int_{\omega_{\mathbb{R}}}\frac{e^{i(\Delta-\omega)t/2}t\,\mathrm{sinc}((\Delta-\omega)t/2)}{\pi}\rho(\omega)\mathrm{d}\omega, \tag{3.6}$$

where $\omega_{\mathbb{R}}$ spans the whole frequency spectrum of the waveguide. The fraction in the integrand is a nascent Dirac delta as $t \rightarrow \infty$. This means, that if Δ is resonant with the interior of the continuum $\omega_{\mathbb{R}}$ and t is large enough for this fraction to be strongly localized in a part of the bath that has a fairly uniform density of states, then the integral can be approximated by $\rho(\Delta)$ to obtain

$$\frac{\partial}{\partial t}\left(e^{i\Delta t}A(t)\right) = -\frac{\pi g^2\rho(\Delta)}{2k_{\mathsf{r}}}e^{i\Delta t}A(t). \tag{3.7}$$

The solution for this equation is

$$A(t) = e^{-(\Gamma/2+i\Delta)t} \tag{3.8}$$

with a decay rate

$$\Gamma = \frac{\pi g^2\rho(\Delta)}{k_{\mathsf{r}}}. \tag{FGR}$$

This is known as *Fermi's golden rule* [119]. Reintegrating in (3.3) the field amplitudes of the modes,

$$B_q(t) = g\frac{e^{-(\Gamma/2+i\Delta)t} - e^{-i\omega_q t}}{\Delta-\omega_q-i\Gamma/2}, \tag{3.9}$$

which has an asymptotic Lorentzian emission spectrum

$$|B_q(t)|^2 \xrightarrow{t\to\infty} \frac{g^2}{(\Delta-\omega_q)^2+\Gamma^2/4} \tag{3.10}$$

centered at Δ with full width at half maximum Γ. These properties are compared with experimental data in FIG. 3.2.

The Markovian approximation, although broadly used (sometimes in very creative ways [120]), leads to paradoxes [59] when used outside its range of applicability. One can see such contradictions for instance by comparing Eqns. (3.3), which gives $\frac{\partial}{\partial t}\left(e^{i\Delta t}A(t)\right) = 0$ at $t = 0$, with (3.7), which predicts a non-vanishing value.

In fact, the violation of the Markovian approximation at very short decay times can be reasoned in multiple ways: let's say that a single emitter is weakly coupled to a single band, tuned deeply inside of the band continuum. These conditions allow for the application of the Markovian approximation. At sufficiently short times, however, the time-energy uncertainty principle will not allow the emitter to resolve the band from a single state; so the initial dynamics will follow a simple Rabi oscillation between two states [91]. In a reciprocal picture, if the photonic band is created by a coupled-cavity array [50, 55,

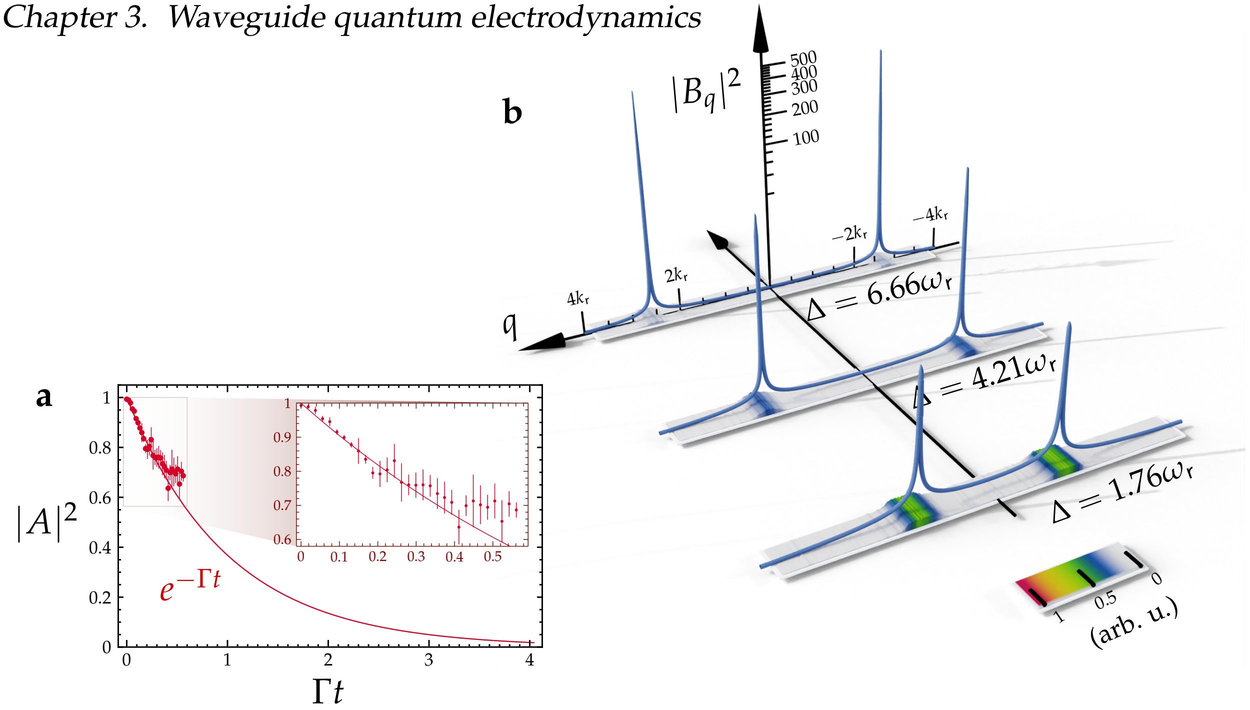

FIGURE 3.2: *Markovian emission* of atomic matter waves from a single QE. **a,** The predicted decay (solid line) is exponential. The data (points and error bars from [91]) correspond with matter-wave decay to the center of an approximately-single band ($s_a = 20$ and $s_b = 2.5$) of half-width $2J = 2\pi \times 0.92\,\text{kHz}$. The coupling $g = 0.36J$ implies via (FGR) a decay rate $\Gamma = 2g^2/\omega_r$ that fits well with the observation. **b,** Asymptotic Lorentzian emission profiles (blue lines, from Eqn. (3.10)) into free space ($s_a = 30$ and $s_b = 0$) at different detunings. Below them are the corresponding ToF pictures taken after applying a microwave with Rabi frequency $\Omega = 2\pi \times 1.5\,\text{kHz}$ for $t = 0.4\,\text{ms}$ [78].

121–123], at very short emission times the radiation has not noticed the presence of neighboring cavities, so the initial dynamics is a cavity-dressed Rabi oscillation.

The slow propagation of matter waves makes them suitable for measuring this violation at short times, which was first demonstrated in [124] with ultracold atoms in accelerating optical lattices and later seen more clearly in [91] with the matter-wave platform for wQED. More recently [125], a competing platform with acoustic waves [126] has also observed this effect.

The Markovian approximation simplifies enormously the dynamics, but understanding when or how the approximation is applicable is very difficult. For instance, in Sec. 3.4 we discuss a system with strong Markovian traits in a strongly non-Markovian parameter regime. Moreover, it has been argued recently [127] that "non-Markovianity is physically undecidable and extremely counterintuitive, since its features can change at any time, without precursors". Simple examples of this can be achieved by placing a mirror at some distance from a Markovian emitter [58], making a loop in the waveguide, or similarly coupling the waveguide to a ring resonator [128]. Then the emitter decay is Markovian until the emission comes back to it and is partially reabsorbed. We approach these difficulties by solving the decay dynamics exactly, gaining an integral understanding of the wQED systems.

3.2 Effects of strong coupling

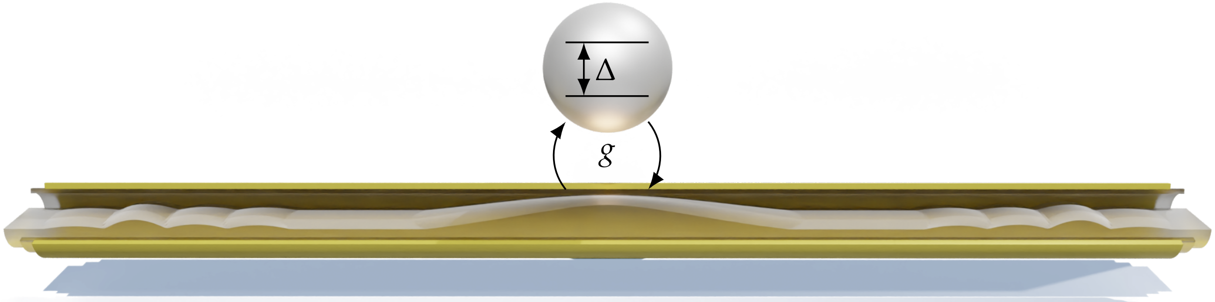

FIGURE 3.3: A *strongly coupled emitter* ($g > \Delta > 0$) whose coupling exceeds the detuning from the edge of a PDR can not only emit waves but also bind them.

As the coupling g increases, the validity of the Markovian approximation is compromised when g becomes comparable to the detuning from the nearest continuum edge, as the edge starts participating in the decay dynamics due to power-broadening. The dispersion relation in waveguides around these edges is typically parabolic

$$\omega_q = \omega_{\mathrm{r}} \left(q/k_{\mathrm{r}}\right)^2, \tag{PDR}$$

and exactly so for our case of reference of matter waves moving in free space ($s_b = 0$). These edges ($\omega = 0$ in this case) have a diverging DoS

$$\rho(\omega) = \frac{k_{\mathrm{r}}}{\sqrt{\omega\omega_{\mathrm{r}}}}, \tag{3.11}$$

which is incompatible with the application of FGR at $\Delta = 0$.

The most extended method [45, 88–90, 129, 130] to go beyond the Markovian approximation starts by Laplace-transforming Equations (3.3). Here, we will be consistent with Refs. [70] and use a tilde to denote the Wick-rotated Laplace transform of a function, $\tilde{f}(\omega) = -i\mathcal{L}\{f\}(-i\omega)$. This choice is motivated by Ref. [51] and mainly differs from the broadly used [45, 88–90, 129, 130] Laplace transform $\mathcal{L}\{f\}(s) = \int_0^\infty f(t)e^{-st}\mathrm{d}t$ in the change of variable $\omega = is$, that brings this complex variable closer to its physical meaning of a frequency. Indeed, with this choice the inverse transformation is given by

$$f(t) = -\frac{1}{2\pi i}\int_{-\infty+i0^+}^{+\infty+i0^+} \tilde{f}(\omega)e^{-i\omega t}\mathrm{d}\omega, \tag{IT}$$

which is closer-looking to a Fourier transform but has a displaced integration contour that avoids all the complex singularities of $\tilde{f}(\omega)$ on the real line. Transforming (3.3) reads as

$$\begin{cases} \omega\tilde{A} - 1 = \Delta\tilde{A} + \sum_q g\tilde{B}_q \\ \omega\tilde{B}_q = \omega_q\tilde{B}_q + g\tilde{A}, \end{cases} \tag{3.12}$$

which can be directly solved as

$$\begin{cases} \tilde{A} = \frac{1}{\omega-\Delta+i\tilde{G}(\omega)} \\ \tilde{B}_q = \frac{g}{\left(\omega-\omega_q\right)\left(\omega-\Delta+i\tilde{G}(\omega)\right)}, \end{cases} \tag{3.13}$$

where

$$\tilde{G}(\omega) = \sum_q \frac{ig^2}{\omega - \omega_q} \qquad \text{if } \omega \notin \omega_{\mathbb{R}} \tag{3.14}$$

is the transformed bath correlation function[1] [51, 89, 90]. For the PDR, this simply becomes

$$\tilde{G}(\omega) = \frac{-\pi i g^2}{2\sqrt{-\omega\omega_{\rm r}}}. \tag{3.15}$$

In this type of analysis, the location of the branch cuts in the complex plane is crucial (see FIG. 3.4**a**). We will use the square roots that have the branch cut to the left of the origin (more specifically $\arg\sqrt{\omega} \in (-\pi/2, \pi/2]$ for all $\omega \in \mathbb{C}$), which requires careful use of the multiplicative properties of this function (e.g. $\sqrt{-\omega}\sqrt{\omega_{\rm r}} = \sqrt{-\omega\omega_{\rm r}} \neq i\sqrt{\omega\omega_{\rm r}}$).

Since the initial state is a localized one, simulating the system for short evolution times is not a problem. The complication is to know the evolution at large times ($\omega_{\rm r}t \gg 1$) or the asymptotic dynamics ($\omega_{\rm r}t \to \infty$), for which the IT has a poor choice of integration contour because the integrated is rapidly oscillating and slowly decaying. A smarter choice of contour requires to analytically continue $\tilde{A}(\omega)$ in a way that the horizontal branch cut $[0, +\infty)$ becomes the vertical $[0, -i\infty)$. In this case, this can easily be done by the replacement $\sqrt{-\omega\omega_{\rm r}} \to (1-i)\sqrt{-i\omega\omega_{\rm r}/2}$ in (3.15). Despite the abuse of language, we use again $\tilde{A}(\omega)$ to denote the new function. Then the residue theorem can be used to readapt the integration contour to the singularities of $\tilde{A}(\omega)$ (see FIG. 3.4**a**) resulting in the expression

$$A(t) = \sum_{\rm p} \frac{e^{-i\omega_{\rm p}t}}{1 - \frac{\pi(1+i)g^2}{4\omega_{\rm p}\sqrt{-2i\omega_{\rm p}\omega_{\rm r}}}} + \int_0^\infty \frac{g^2(1-i)\sqrt{2\gamma\omega_{\rm r}}}{4\gamma\omega_{\rm r}(\Delta+i\gamma)^2 + i\pi^2 g^4} e^{-\gamma t}\,{\rm d}\gamma, \tag{3.16}$$

where p runs over the "upper" poles of $\tilde{A}(\omega)$ (i.e. the ones on the relevant Riemann sheet, not the ones beyond the vertical branch cut), that we assume to be simple and not belonging to the cut $[0, -i\infty)$. The advantage of this integral expression is that it has excellent convergence properties, due to the quadratic increase $\sqrt{2\gamma\omega_{\rm r}}$ at small γ and the exponential decrease $e^{-\gamma t}$ at large γ. Furthermore, the convergence only improves as t grows until a series expansion of the algebraic part of the integrated leads to

$$A(t) \xrightarrow{t\to\infty} \sum_{\rm p} \frac{e^{-i\omega_{\rm p}t}}{1 - \frac{\pi(1+i)g^2}{4\omega_{\rm p}\sqrt{-2i\omega_{\rm p}\omega_{\rm r}}}} - \frac{(1+i)\omega_{\rm r}^{1/2}}{\sqrt{2}\pi^{3/2}g^2t^{3/2}}. \tag{3.17}$$

---

[1] Despite our choice of labels, in the Green's function formalism for wQED [68] $\tilde{A}(\omega)$ is closely related to the QE Green's function, whereas $\tilde{G}(\omega)$ is closer to the definition of a self-energy, in which the excited QE emits a photon only to reabsorb it immediately.

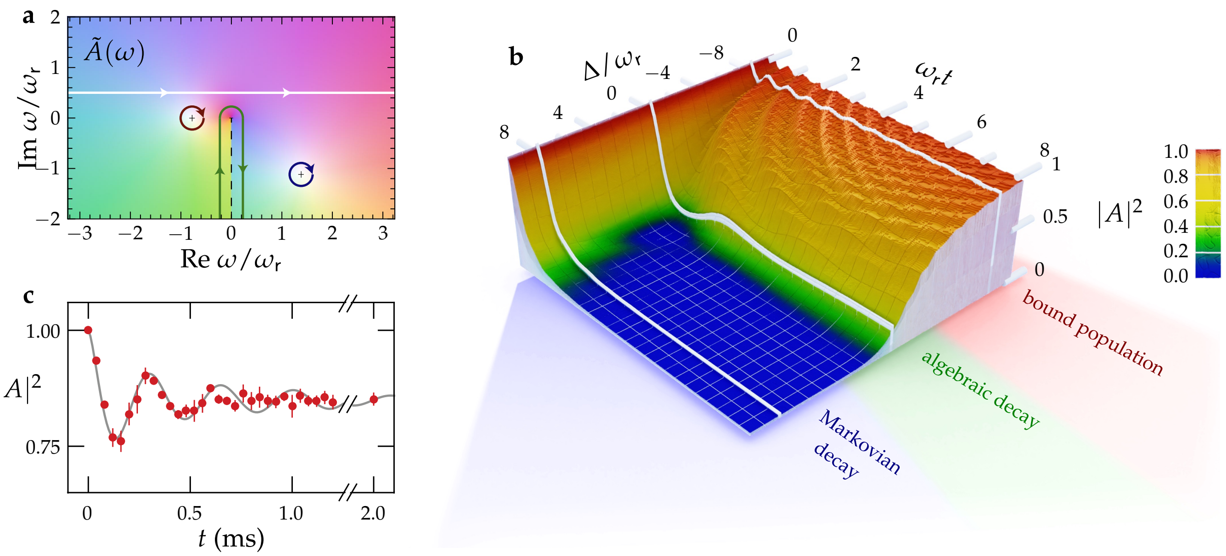

FIGURE 3.4: *Non-Markovian decay of a single emitter coupled to a* PDR. **a,** Domain coloring plot of $\tilde{A}(\omega)$ for $g = \Delta = \omega_r$. The integration contour of the IT (white solid line) can be readapted to circle around the bound state frequency (in dark red), the continuum edge (dark green), and the exponentially-decaying state (dark blue). **b,** Decay curves $|A(t)|^2$ of the emitter at coupling $g = \omega_r$ and variable detunings. Highlighted as white lines are cases $\Delta = -8\omega_r$ at which the contribution of the bound state is dominating, $\Delta = 0$ with dynamics dominated by the continuum edge, and $\Delta = 8\omega_r$ which is roughly exponential decaying. Figure readapted from [90]. **c,** Decay data (in red) of a single initially populated emitter radiating matter-waves into free space ($s_a = 30$ and $s_b = 0$) at parameters $\Omega = 2\pi \times 3.0(3)$ kHz and $\Delta = -2\pi \times 1.7(3)$ kHz. The curve (in gray) corresponds to the theory for a single emitter [90], for the fitting parameters $\Omega = 2\pi \times 2.79(4)$ kHz and $\Delta = -2\pi \times 2.08(3)$ kHz. Figure panel **b** is adapted from [90] and **c** is reproduced from Ref. [78] with permission from Springer Nature.

This indicates that the poles $\omega_p \in \mathbb{R}$ are undecaying, i.e. they represent bound states (BSs), the ones with $\operatorname{Im}\omega_p < 0$ are exponentially decreasing in time, as in the Markovian limit, the ones with $\operatorname{Im}\omega_p > 0$ are not physical, so if they exist they are located in the "lower" Riemann sheet[2], and the edge of the continuum –responsible for the integral in (3.16)– represents algebraic decay of order 3/2. Although all these elements participate together in the dynamics, as we vary Δ (see FIG. 3.4**b**) the dominant role goes to the singularity that is most resonant with the detuning.

In particular, if $0 < g/\omega_r \ll \Delta/\omega_r$ then $A(t) \simeq e^{-i\omega_p t}$ with $\omega_p \simeq \Delta - i\frac{\pi g^2}{2\sqrt{\Delta\omega_r}}$, recovering the Markovian approximation of Section 3.1.

---

[2] See FIG. 3.18 for an example.

The simple functional dependence of $\tilde{A}(\omega)$ allows for counting the number of poles as a function of g and Δ. According to (3.13), these poles are the roots of the polynomial

$$(\omega_\mathrm{p} - \Delta)^2 \omega_\mathrm{p} + \frac{\pi^2 g^4}{4\omega_\mathrm{r}}; \tag{3.18}$$

so there are at maximum 3 poles. The polynomial changes sign for $\omega_\mathrm{p} \in (-\infty, 0)$, so there must be a pole in this gap[3]. This argument also holds for the denominator $\omega - \Delta + i\tilde{G}(\omega)$, which increases monotonically, so always one (and only one) of said poles is an upper pole, i.e. it represents an atom-photon bound state [37, 40] in the gap. The polynomial is always positive for $\omega_\mathrm{p} \in [0, +\infty)$, so there are no bound states in the continuum [131]. Therefore if the remaining two poles are real, they are negative and do not contribute physically. If they are complex, they must be complex conjugates because the coefficients of the polynomial are real. In this case, only the one with a negative imaginary part can be an upper pole, since the other would imply an exponential growth –rather than a decay– in (3.16). This growth cannot be physical because $|A| > 1$ violates the conservation of the norm of the quantum state (due to the Hermiticity of the Hamiltonian). A little bit of analysis reveals that for $\Delta = -\frac{1}{2} g \sqrt[3]{\pi^2 g/\omega_\mathrm{r}}$ the Markovian pole intersects the branch cut at $i\Delta \in (0, -i\infty)$ and becomes an upper pole for $\Delta > -\frac{1}{2} g \sqrt[3]{\pi^2 g/\omega_\mathrm{r}}$.

An analogous analysis can be done for $\tilde{B}_q$ (see FIG. 3.12**c**), but looking at (3.13) we quickly realize that the singularities are the same as for $\tilde{A}$ with the exception of a real pole at ω_q, that does not represent a bound state but an emitted wave of quasimomentum q that has entirely left the emitter. This is no coincidence. The function $\omega - \Delta + i\tilde{G}(\omega)$ is a fundamental characteristic of this system and it would appear in one form or another regardless of the basis chosen for the single-excitation sector.

To understand this better, notice that the transformed Schrödinger Eqn. (3.12) takes the form

$$\omega \left|\tilde{\Psi}\right\rangle - \left|\Psi(0)\right\rangle = \hbar^{-1}\hat{H}\left|\tilde{\Psi}\right\rangle \tag{TSE}$$

in a basis-independent notation. The solution is

$$\left|\tilde{\Psi}\right\rangle = \left(\omega\hat{\mathbb{1}} - \hat{H}/\hbar\right)^{-1}\left|\Psi(0)\right\rangle. \tag{3.19}$$

Determinants of infinite matrices are not generally well defined, but if the Hamiltonian was finite-dimensional, the Cramer's rule for the inverse would allow us to identify $\det\left(\omega\hat{\mathbb{1}} - \hat{H}/\hbar\right) \propto \omega - \Delta + i\tilde{G}(\omega)$. So, in many ways, we can think of this function as the characteristic polynomial of the Hamiltonian restricted to the single-excitation sector, which is basis invariant.

To further find the spatial properties of the bound states, we can solve the eigenvalue equation

$$\omega\left|\Psi\right\rangle = \hbar^{-1}\hat{H}\left|\Psi\right\rangle. \tag{3.20}$$

---

[3] In consistency with [51], I will use the term 'gap' to refer to any energetically-forbidden connected region of the dispersion relation, including the unbounded region below a PDR.

The formal similarities with the TSE can be used, as we will see in Sec. 3.6.7, to recycle the solution (3.13) from the transformed field amplitudes. This is particularly useful for higher excitation numbers [70] where the solution becomes extremely long and involved, but for one emitter with one excitation the solution simply reads

$$B_q = \frac{gA}{\omega - \omega_q}, \tag{3.21}$$

where A can be computed (or not) as a normalization factor and ω is the frequency of the bound state that we computed above. Given the PDR, this is a Lorentzian dependence in momentum space and an exponentially localized state in position space[4]

$$B_x = \sum_q \frac{gA}{\omega - \omega_q}\sqrt{\frac{k_\mathrm{r}}{\pi}}e^{iqx} = -\frac{gA}{2}\sqrt{\frac{\pi k_\mathrm{r}}{-\omega\omega_\mathrm{r}}}e^{-\sqrt{-\omega/\omega_\mathrm{r}}|k_\mathrm{r}x|} \tag{3.22}$$

(notice that $\sqrt{-\omega/\omega_\mathrm{r}} > 0$ since the bound-state frequency is negative). This distribution can be seen as an evanescent plane wave[5] $B_x \propto e^{\pm iq(\omega)x}$ with a complex momentum $q(\omega) = k_\mathrm{r}\sqrt{\omega/\omega_\mathrm{r}}$.

The first direct picture of such a bound state was taken in 2018, with the matter-wave platform [78] via adiabatic generation of the state. The state was further proven to be bound to the emitter by showing that it does not fall when the center of the weak harmonic trap is displaced. The data from this paradigmatic experiment (which preceded the author's time in the lab) is presented in FIG. 3.5.

3.3 Effects of the emitter size

Quantum emitters have a size a_{QE} that is typically much smaller than the wavelength of the emitted radiation ($ka_{QE} \ll 1$), motivating their treatment as point-like[6]. This approximation is responsible for a sharp vertex at the center of the bound state (see Eqn. (3.22)) that is often represented in the literature (see e.g. the introductory figures in [47, 50, 122]), while one can argue that the evanescent wave only decays exponentially after leaving the reach of the emitter . The implementation of giant atoms ($ka_{QE} \sim 1$) with superconducting qubits [77] has demonstrated that artificial systems can also break this approximation. While a creative proposal has been made to realize giant atoms [134] in the matter-wave platform via a fast shift of the optical lattices, the size of the emitter in the experiments described in Sec. 2.2

$$k_\mathrm{r}a_{QE} = s_a^{-1/4} \tag{HOL}$$

---

[4] In this chapter we will use the x coordinate to denote space to avoid confusion with a generic complex number, although we remind that the matter-wave experiments were conducted in the vertical z direction (see Sec. 2.2).

[5] Our use of the term *"evanescent wave"* is reserved for functions of the form $e^{\pm iqx}$, which differs slightly from the use given in [90], which we study in the next section.

[6] This is commonly known as the *dipole approximation* in quantum optics [132, 133].

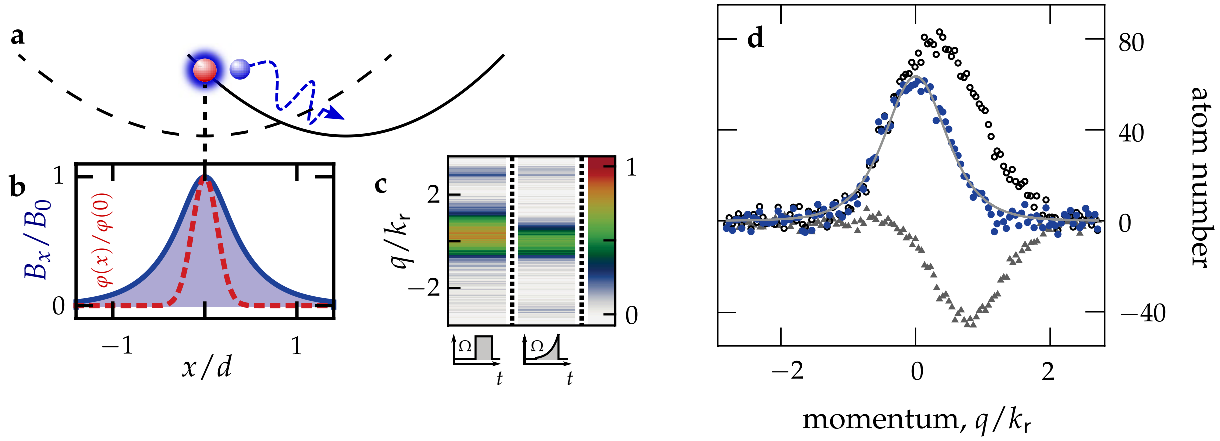

FIGURE 3.5: *Evanescent matter waves bound to a QE.* **a,** Illustration of separation of evanescent and propagating waves along the weakly confining tube axis. As the harmonic confinement (black curve) shifts its equilibrium position (from the dashed to the solid lines), matter waves that are bound to the emitter remain locked in place, whereas emitted waves accelerate toward the new equilibrium position. **b,** Spatial form of the rescaled field amplitudes for the $|r\rangle$ atoms (red dashed Gaussian $\varphi(x)$, $s_a = 30$) and the evanescent $|b\rangle$ atoms (blue, solid doubly-decaying exponential B_x, $s_b = 0$) for the created bound state. **c,** ToF pictures displaying raw emission data for a sudden (left) and adiabatic (right) turn-on of the microwave coupling with $\Omega = 2\pi \times 3.0(3)$ kHz and $\Delta = -2\pi \times 2.2(3)$ kHz. **d,** After processing the data and averaging over 50 runs, the atomic distribution of the $|b\rangle$ atoms emitted adiabatically (filled blue dots) fits well with the expectation $\propto |B_q|^2$ (gray solid line, originally predicted in [90]) for a $\Delta_\mathrm{fit} = -2\pi \times 2.1(1)$ kHz. The analogous measurement of the atomic distribution for a sudden microwave turn-on (empty dots) is composed of both bound and radiated waves. The difference between the two data sets (triangles) has an average momentum $0.80(1)\hbar k_\mathrm{r}$ whereas the expected for an atom free from the influence of the QE is $0.83(7)\hbar k_\mathrm{r}$. Figure reproduced from Ref. [78] with permission from Springer Nature.

is not that 'gigantic' but still comparable to the de Broglie wavelength of the emitter radiation.

For a deep red lattice ($s_a \gg 1$), the wavefunction of an atom that is resting at the parabolic bottom of one of the lattice wells

$$s_a E_\mathrm{r} \sin^2(k_\mathrm{r} x) \approx s_a E_\mathrm{r} (k_\mathrm{r} x - \pi j)^2 \tag{3.23}$$

is approximately a Gaussian Wannier function [90]

$$\varphi_j(x) = \frac{1}{\pi^{1/4} a_{QE}^{1/2}} \exp\left(-\frac{(x - dj)^2}{2a_{QE}^2}\right) \tag{GWF}$$

where we have identified the emitter size a_{QE} with the harmonic oscillator length (HOL). The effects of the emitter size enter the WWH through the momentum dependence of the coupling $g_{j,q}$. Combining the harmonic approximation with $s_b = 0$, Eqn. (2.4) yields[7]

$$g_{j,q} = \Omega \sqrt{\frac{k_{\mathrm{r}} a_{QE}}{2\pi^{1/2}}} \exp\left(-\frac{1}{2} q^2 a_{QE}^2\right) e^{iqdj}. \tag{3.24}$$

Here, a broad Gaussian envelope embeds the effects of the emitter size a_{QE} and becomes constant only in the limit $a_{QE} \to 0$. Intuitively, if the wave performs multiple oscillations within the emitter, it will self-interfere suppressing its coupling to the emitter. In contrast, the complex phase e^{iqdj} can be 'gauged out' if there is a single emitter by taking the natural choice of placing the coordinate origin at the emitter (for which we omit the subscript $j = 0$), but if multiple emitters are considered it plays a crucial role by encoding the phase retardation that a wave of momentum q experiences traveling between $j + 1$ adjacent emitters.

For the case analyzed in the previous section, the finite emitter size has two main repercussions. The transformed bath correlation function

$$\tilde{G}(\omega) = \sum_q \frac{i|g_q|^2}{\omega - \omega_q} = -i\sqrt{\pi}\Omega^2 k_{\mathrm{r}} a_{QE} e^{-(k_{\mathrm{r}} a_{QE})^2 \frac{\omega}{\omega_{\mathrm{r}}}} \frac{\operatorname{erfc}\left(k_{\mathrm{r}} a_{QE} \sqrt{-\omega/\omega_{\mathrm{r}}}\right)}{4\sqrt{-\omega\omega_{\mathrm{r}}}} \tag{3.25}$$

(where $\operatorname{erfc}(x) = 2/\sqrt{\pi} \int_x^\infty \exp\left(-y^2\right) \mathrm{d}y$ is the complementary error function) makes the analysis of the spectrum a lot more complicated but without qualitative changes. This situation contrasts with the multi-emitter case (see Sec. 3.5), in which even a small emitter size can drastically affect the spectrum at a qualitative level.

Secondly, the distribution of the bound states is also affected by this q-dependent change in coupling. As illustrated in FIG. 3.5**b**, such BSs have a $|r\rangle$ part with spatial amplitude $A\varphi(x)$ that is proportional to the GWF, and a $|b\rangle$ part whose amplitude is

$$B_x = \textstyle\sum_q \frac{g_q A}{\omega - \omega_q} \sqrt{\frac{k_{\mathrm{r}}}{\pi}} e^{iqx} =$$
$$-\frac{\pi^{1/4}}{4} A\Omega k_{\mathrm{r}} \sqrt{\frac{a_{QE}}{-2\omega\omega_{\mathrm{r}}}} \exp\left(\frac{-\omega}{2\omega_{\mathrm{r}}} k_{\mathrm{r}}^2 a_{QE}^2 - k_{\mathrm{r}} x \sqrt{\frac{-\omega}{\omega_{\mathrm{r}}}}\right) \operatorname{erfc}\left(\frac{-x}{\sqrt{2} a_{QE}} + k_{\mathrm{r}} a_{QE} \sqrt{\frac{-\omega}{2\omega_{\mathrm{r}}}}\right) + (x \leftrightarrow -x). \tag{3.26}$$

Integrals in (3.25) and (3.26) are not simple, yet crucial for the analytic continuations. The procedure to solve both integrals is oddly similar and outlined in FIG. 3.6. The above formula is best understood as the convolution

$$B_x \propto \varphi(x) * e^{-\sqrt{-\omega/\omega_{\mathrm{r}}}|k_{\mathrm{r}} x|} \tag{3.27}$$

between the Gaussian emitter and the evanescent wave from (3.22). The evanescent wave dresses the QE with a smooth hood wrapping around it and an exponential skirt falling off it (see FIG. 3.5**b**).

---

[7] Differences with the value listed in Ref. [90] stem from the different choice in normalization for the plane waves.

Systematic studies of the dependence of matter-wave emission on the emitter size have not so far been realized. The main difficulty is technical, as the fourth root in (HOL) greatly reduces the sensitivity of a_{QE} on the depth of the SDOL, which has limited power in itself[8].

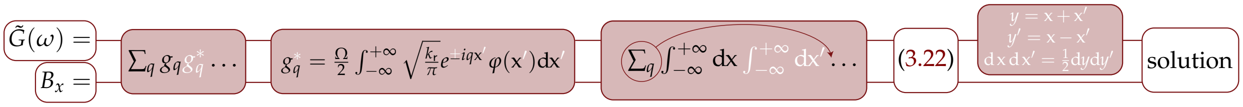

FIGURE 3.6: Schematics of the intermediate steps omitted in the integrals (3.25, in black and white) and (3.26, in black). Ideas based on Ref. [51].

3.4 Effects of a band structure

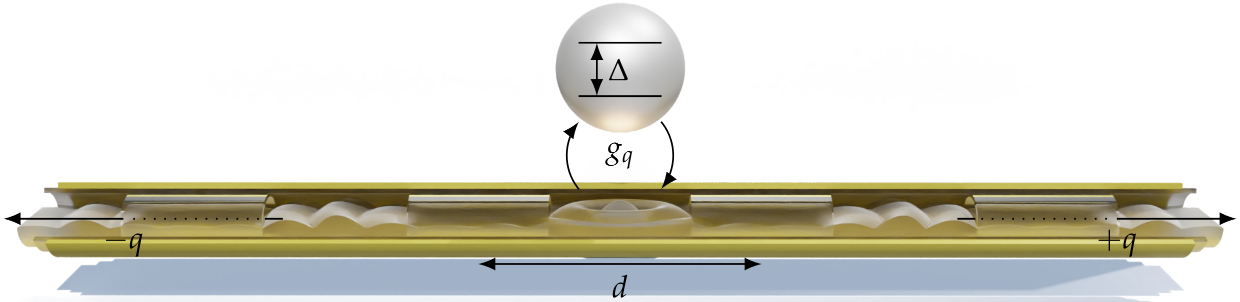

FIGURE 3.7: A single QE coupled to a *structured medium*. The periodic change in the index of refraction causes a band structure for the photons traveling through the waveguide.

A central topic in the study of waveguide-QED systems [45, 129, 135–137], are the drastic modifications to the emission process caused by manipulating the mode distribution of the radiation [37, 39, 138]. It is of particular interest when the mode spectrum contains forbidden regions (gaps) and allowed bands as it encompasses both the aspects of the continuum, like in the case of free space, and the aspects of discrete spectra, such as emission into a cavity.

The difficulty of a multiband analysis has led to the use of different assumptions. Creatively, Ref. [37] assumed a waveguide with an index of refraction that is piece-wise constant (see FIG. 3.7). Since the resulting Bloch waves are piece-wise plane waves, this system can be analyzed exactly.

Another assumption could be to consider an emitter that is only spectroscopically resonant with one band edge. In this case, the latter can be approximated with the parabolic

---

[8] The achieved SDOL depth was $s_a \leq 30$ in previous experiments [78, 91, 92, 118].

dispersion relation (PDR), matching the analysis of previous sections. This is also naturally the case for matter waves emitted into free space [78, 88, 90].

Lastly, another common approach [50, 70, 91, 139] is to consider the potential for the waves to be so deep that only hopping (of rate J) between neighboring sites is possible. Then the dispersion relation becomes a single band

$$\omega_q = -2J\cos(qd) \tag{SB}$$

with DoS

$$\rho(\omega) = \frac{2k_{\mathrm{r}}}{\pi\sqrt{4J^2-\omega^2}} \tag{3.28}$$

and a lattice momentum $q \in (-k_{\mathrm{r}}, k_{\mathrm{r}}]$ restricted to one BZ.

In this section, we show what we consider to be an elegant approach that allows for a common efficient treatment of generic band structures in and beyond the real line, as far as a 1D periodic potential induces them. Then we will describe emission into such a band structure. This section mostly adheres to the findings presented in [51].

3.4.1 Lattice functions on the complex plane

Imaginary numbers were born and named after something that cannot be real, yet they have very physical consequences. And complex analysis is, oddly, the simplest of analyses. The band structure of a periodic system is a striking example of it, since it seems to be composed of an infinite number of bands $\{\omega_n(q)\}_{n=1}^{\infty}$ that, when extended to the complex momentum plane, unveil as fragments of a common function (see FIG. 3.8).

It is, in fact, a necessity to evaluate different lattice-related functions in the complex frequency plane for the use of the IT. This is challenging since some of these functions, such as the lattice momentum $q(\omega)$, are multivalued and some others, such as the Bloch waves $\psi_{q(\omega)}(0)$, are physically defined only up to a phase factor. In this subsection we develop an efficient way of doing so via an infinite-product representation. These apply to any 1D potential, although we will focus on the sinusoidal potential

$$V_b(x) = s_b E_{\mathrm{r}} \sin^2(k_{\mathrm{r}} x) \tag{SP}$$

for $|b\rangle$ matter waves for the sake of concreteness. Furthermore, we warn the reader that although mathematically we interpret the recoil units (E_{r}, ω_{r}, and k_{r}) as the natural units of the problem, in practice they change with s_b as the wavelength of the SDOL is tuned out of the magic condition $s_b = 0$ [109]. Their values should therefore be calculated on a case-to-case basis and will differ slightly from those in the List of Physical Constants and Characteristic Quantities.

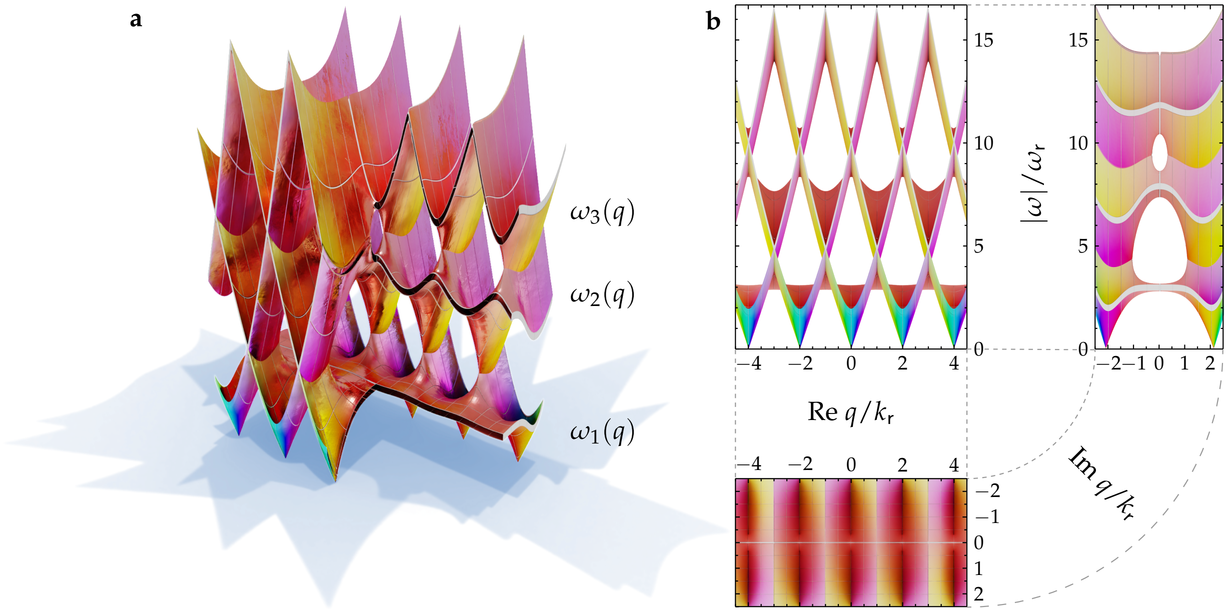

FIGURE 3.8: Analytic continuation to complex quasimomenta ($q \in \mathbb{C}$) of the *band structure* induced by a sinusoidal potential (SP) of depth $s_b = 10$. **a,** Domain coloring plots of the three lowest energy bands. The height corresponds to the absolute value of the function, hue is directly proportional to the argument of the function (red for a positive number and blue for a negative), saturation decreases with the absolute value, and brightness is one. The choices of lighting and texture serve aesthetic purposes. A section has been removed for clearer visualization of the bands on the real line. **b,** Front, lateral, and top view of the same figure for a quantitative description.

We start by analyzing the band structure of the matter-wave vacuum using a standard textbook formula [140],

$$\cos\frac{\pi q(\omega)}{k_\mathrm{r}} = \frac{\cos\left(\pi\sqrt{\frac{\omega}{\omega_\mathrm{r}} - \frac{s_b}{2}} + \arg\, t(\omega)\right)}{|t(\omega)|} \equiv T(\omega), \tag{3.29}$$

relating the lattice momentum $q(\omega)$ to the transmission coefficient $t(\omega)$ for a plane wave of frequency ω going through the isolated potential barrier described by $V_b(x)$ for $x \in [0, d]$ and 0 otherwise (see FIG. 3.9**a**). The function $T(\omega)$ is a convenient way of folding the band structure into a simpler function akin to a polynomial of infinite degree[9]. For instance, the single band (SB) approximation being sinusoidal is equivalent to approximating $T(\omega)$ as being linear.

Importantly, we will see that $t(\omega)$ does not need to be evaluated explicitly, but instead just some special points of $T(\omega)$ will be necessary for the analysis, as they fully determine the physical properties of the system. These special points, shown in Fig. 3.9**b**, are the energies where $T(\omega)$ takes zero, unity, or extreme values. In particular, the energies with $|T| = 1$ correspond to the band edges of the dispersion relation, which host Bloch waves

---

[9] Formally, $T(\omega)$ is an entire function: a holomorphic function with no complex singularities.

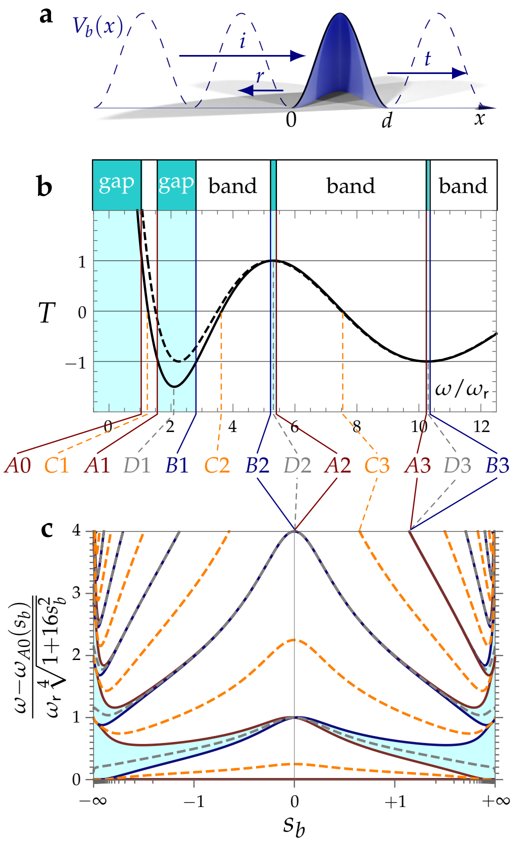

FIGURE 3.9: *Characteristic frequencies of a band structure* induced by a sinusoidal potential (SP). **a,** The potential $V_b(x)$ (dashed line) defines a barrier (filled area) that either reflects (r) or transmits (t) an incident (i) wave. **b,** The function $T(\omega)$ (solid black line; example with $s_b = 2.5$) determines band edges (ω_{An} and ω_{Bn}), zeroes ω_{Cn} and extrema ω_{Dn}. The corresponding asymptotic expression, $\cos(\pi\sqrt{\omega/\omega_\mathrm{r} - s_b/2})$, is shown as a black dashed line. **c,** Diagram of these characteristic energies (with the same color code as in **a**) above the ground frequency $\omega_{A0}(V_b)$ in units of a frequency scale $\omega_\mathrm{r}\sqrt[4]{1+16s_b^2}$ chosen to match the recoil energy when there is no lattice and the harmonic-approximation frequency split when the lattice is very deep. The abscissa s_b is presented in arctangent scale. Figure panels **b** and **c** reproduced from Ref. [51] with permission from the APS.

carrying an integer multiple of the recoil momentum and definite parity. Correspondingly, we label the band edges with even Bloch waves (Mathieu cosines) as $\{\omega_{An}\}_{n=0}^{\infty}$ and those with odd waves (Mathieu sines) as $\{\omega_{Bn}\}_{n=1}^{\infty}$ [141]. Finally, we label the zeroes $\{\omega_{Cn}\}_{n=1}^{\infty}$ and the extrema $\{\omega_{Dn}\}_{n=1}^{\infty}$.

The ordering of these energies for different potential depths, shown in Fig. 3.9**c**, is easily understood for free-space motion $s_b = 0$ and the limit $s_b \to \pm\infty$, as the lattice spectrum becomes that of a quantum harmonic oscillator. We note that flipping $s_b \mapsto -s_b$ (as experimentally done in [91], see Fig. 3.12**c**) leaves the band structure unchanged, but swaps the parity of the edges belonging to every other energy gap. Physically, this transformation is equivalent to displacing the emitter by half a lattice period $d/2$.

With these definitions, we can efficiently perform an analytical extension of several functions into the complex energy plane by using infinite products. For instance, consider $T(\omega)$. Since $t(\omega) \to 1$ as $|\omega| \to \infty$, the asymptotic expression for this function readily follows from Eqn. (3.29), and already resembles $T(\omega)$ quite well (see Fig. 3.9**b**). A perfect match can be achieved if one “corrects” the zeroes of the approximation by first dividing through them and then multiplying with the actual zeroes of $T(\omega)$, which gives

$$T(\omega) = \cos\left(\pi\sqrt{\frac{\omega}{\omega_\mathrm{r}} - \frac{s_b}{2}}\right)\prod_{n=1}^{\infty}\frac{\omega - \omega_{Cn}}{\omega - \frac{s_b}{2} - \left(n - \frac{1}{2}\right)^2\omega_\mathrm{r}}. \tag{3.30}$$

This identity is in fact guaranteed by Liouville's theorem of complex analysis [142] (given that $T(\omega)$ has no complex singularities), since the quotient between the two sides of the equation is, by construction, an entire function that tends to 1.

Equation (3.30) in return allows for the analytic extension both of the lattice momentum, via $q(\omega) = \frac{k_{\mathrm{r}}}{\pi} \arccos T(\omega)$, and of the energy bands $\omega_n(q) = T_n^{-1}(\cos(qd))$. In particular, we note that $q(\omega_{Dn})$ are the complex branch points where the n and $n+1$ bands cross (see FIG. 3.8**a**).

An analogous reasoning can be applied for analytical extensions of other lattice functions such as $\rho(\omega)$, $\psi_{q(\omega)}(0)$, $\psi'_{q(\omega)}(0)$ or $e^{iq(\omega)d}$. Since at extreme energies ($|\omega| \to \infty$) an atom traveling through the lattice potential $V_b(x)$ behaves like a free particle subject to the average constant potential $s_b E_{\mathrm{r}}/2$, it is straightforward to find their asymptotic expressions, which can again be corrected further via infinite products. In the case of the density of states (DoS), this results in

$$\rho(\omega) = k_{\mathrm{r}} \sqrt{\frac{1}{\omega_{\mathrm{r}}(\omega - \omega_{A0})} \prod_{n=1}^{\infty} \frac{(\omega - \omega_{Dn})^2}{(\omega - \omega_{An})(\omega - \omega_{Bn})}}. \tag{3.31}$$

For the Bloch waves $\psi_{q(\omega)}(0)$ evaluated at the emitter position $x = 0$, the asymptotic value for high energy is $\sqrt{k_{\mathrm{r}}/\pi}$, and the value has to vanish at the odd band edges ω_{Bn} due to parity. Furthermore, given that the LHS of (3.40) is analytic for all ω outside the bands, the singularities of $\psi^2_{q(\omega)}(0)$ in this region have to be simple poles matching the zeroes ω_{Dn} of the DoS. This leads to the expression

$$\psi_{q(\omega)}(0) = \sqrt{\frac{k_{\mathrm{r}}}{\pi} \prod_{n=1}^{\infty} \frac{(\omega - \omega_{Bn})}{(\omega - \omega_{Dn})}} \tag{3.32}$$

and similarly

$$\psi'_{q(\omega)}(0) = i k_{\mathrm{r}}^{3/2} \sqrt{\frac{\omega - \omega_{A0}}{\pi \omega_{\mathrm{r}}} \prod_{n=1}^{\infty} \frac{(\omega - \omega_{An})}{(\omega - \omega_{Dn})}}. \tag{3.33}$$

We note that Eqns. (3.32,3.33) can be used as initial conditions in the Mathieu equation to evaluate the Bloch wave at any other point through $\psi_{q(\omega)}(x) = \psi_{q(\omega)}(0) C(\omega, x) + i\psi'_{q(\omega)}(0) S(\omega, x)$ where C (S) is an entire function in both of their arguments, (anti-) symmetric in x corresponding to the unnormalized Mathieu cosine (sine) function.

We can also focus on the phase retardation which is analytically given by $e^{iq(\omega)d} = T(\omega) \pm i\sqrt{1 - T^2(\omega)}$. Although we have an analytic way of evaluating $T(\omega)$ as an infinite product (Ref. [51]), a direct substitution of this formula wouldn't be satisfactory, as it does not treat the imaginary part of the complex exponential in the same footing as the real one.

To fix this, we propose the following expansion instead,

$$\begin{aligned} e^{iq(\omega)d} = {} & \cos\left(\pi\sqrt{\frac{\omega}{\omega_\mathrm{r}} - \frac{s_b}{2}}\right) \prod_{n=1}^{\infty} \frac{\omega - \omega_{Cn}}{\omega - \frac{s_b}{2} - \left(n - \frac{1}{2}\right)^2 \omega_\mathrm{r}} \\ & + i \sin\left(\pi\sqrt{\frac{\omega}{\omega_\mathrm{r}} - \frac{s_b}{2}}\right) \sqrt{\frac{\omega - \omega_{A0}}{\omega - s_b\omega_\mathrm{r}/2}} \prod_{n=1}^{\infty} \sqrt{\frac{(\omega - \omega_{An})(\omega - \omega_{Bn})}{(\omega - s_b\omega_\mathrm{r}/2 - n^2\omega_\mathrm{r})^2}} \end{aligned} \tag{3.34}$$

which is a beautiful combination of two famous Euler formulas,

$$e^{ix} = \cos x + i \sin x \quad \text{and} \quad \sin x = x \prod_{n=1}^{\infty} \left(1 - \frac{x^2}{n^2\pi^2}\right) \tag{3.35}$$

"the most remarkable formula in mathematics" [143] and his celebrated solution to the Basel problem [144]. We note that (3.34) indicates that the "real" part is holomorphic, but the "imaginary" part has a square-root branch cut at every band edge. Arguably, the most intriguing part of this formula is that it would be impossible to derive it analytically by substituting the previous one, as a cut-off in the considered gaps for the expression of $T(\omega)$ would still lead to infinite branch points in $\sqrt{1 - T^2(\omega)}$, which is not the case in the formula above.

Finally, we point out a mathematical peculiarity and arguably the strangest way to compute π. By directly comparing the DoS expressed as an infinite product (3.31) and in the SB limit (3.28) one obtains an expression of the number π as a product of the band edges

$$\pi = \lim_{s_b \to \infty} 2\sqrt{\frac{\omega_\mathrm{r}}{(\omega_{A1} - \omega)} \prod_{n=1}^{\infty} \frac{(\omega - \omega_{An})(\omega - \omega_{Bn})}{(\omega - \omega_{Dn})^2}} \qquad \forall \omega \in (\omega_{A0}, \omega_{A1}) \tag{3.36}$$

where the convergence is particularly good at $\omega = \omega_{C1}$. Moreover, an $\omega \in (\omega_{A0}, \omega_{A1})$ satisfying this identity always exists for all $s_b \in \mathbb{R}$ due to the Mean Value Theorem. Albeit using this identity to compute π is impractical, its violation for all ω in the ground band of a band structure proves that the structure cannot be associated with a periodic potential.

3.4.2 Integrating quasimomenta

For either the awe or bewilderment of his readers, Bykov proposed in his seminal paper [37] an intricate integration contour in the complex q-plane that enables direct, exact integration. Bykov's path carefully winds around the complex band crossings $q(\omega_{Dn})$ exploring all levels of FIG. 3.8**a**. Here we show that, just as the lattice functions greatly simplify when evaluated in the complex ω-plane, so does Bykov's contour.

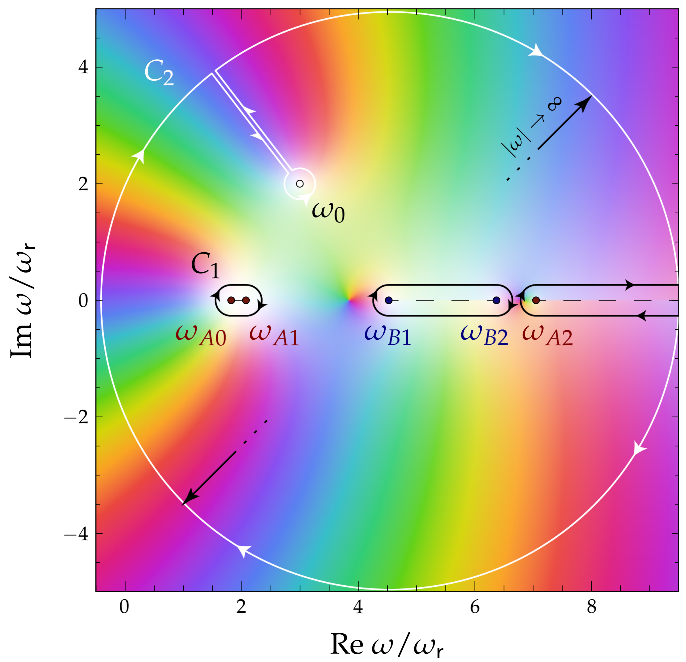

FIGURE 3.10: Domain coloring plot of (3.37) RHS's *integrand* on the complex ω-plane for values $s_b = 5$, $x_1 = x_2 = 1/(3k_{\mathrm{r}})$, $n = 1$, and $\omega_0 = 3 + 2i$. The equivalent integration contours C_1 (in black) and C_2 (in white) are outlined, although in reality, they extend infinitely. Figure adapted from Ref. [51].

We are referring to integrals of the form

$$\int_{-\infty}^{+\infty} \frac{\psi_q^*(x_1)\psi_q(x_2)}{\omega_0 - \omega_q} e^{inqd} \mathrm{d}q = \oint_{C_1} \frac{\psi_{q(\omega)}(-x_1)\psi_{q(\omega)}(x_2)}{2(\omega_0 - \omega)} e^{inq(\omega)d} \rho(\omega) \mathrm{d}\omega \tag{3.37}$$

where C_1 are simply contours circling the bands $\omega_{\mathbb{R}}$ (see Fig. 3.10), $\omega_0 \notin \omega_{\mathbb{R}}$, and the functions on the ω-plane are continuations with $\omega_0 \notin \omega_{\mathbb{R}}$ as branch cuts[10]. The integration contour can be changed to a contour C_2 that circles around ω_0 and around ∞. At diverging frequencies, the free-particle approximation of the integrand

$$\frac{\psi_{q(\omega)}(-x_1)\psi_{q(\omega)}(x_2)}{2(\omega_0 - \omega)} e^{inq(\omega)d} \rho(\omega) \approx \frac{ik_{\mathrm{r}}^2 e^{-k_{\mathrm{r}}(x_2+nd-x_1)\sqrt{s_b/2-\omega/\omega_{\mathrm{r}}}}}{2\pi(\omega - \omega_0)\omega_{\mathrm{r}}\sqrt{s_b/2 - \omega/\omega_{\mathrm{r}}}} \tag{3.38}$$

is strongly suppressed if $x_1 \leq x_2 + nd$, leaving only the contribution of the residue at ω_0. If $x_1 > x_2 + nd$, we can just conjugate the integral in q and then apply the same procedure. The result can be succinctly written as

$$\begin{aligned} &\int_{-\infty}^{+\infty} \frac{\psi_q^*(x_1)\psi_q(x_2)}{\omega_0 - \omega_q} e^{inqd} \mathrm{d}q = \\ &\qquad - \pi i \psi_{q(\omega_0)}(-x_1)\psi_{q(\omega_0)}(x_2)\rho(\omega_0) e^{inq(\omega_0)d} H(x_2 + nd - x_1) + \begin{pmatrix} x_1 \leftrightarrow x_2 \\ n \leftrightarrow -n \end{pmatrix}, \end{aligned} \tag{3.39}$$

with $H(x) = 0, 1/2, 1$ if $x <, =, > 0$ (respectively) denoting the Heaviside step function.

---

[10] Notice that this is a different convention to the one taken in Sec. 3.4.1, so there is again a slight abuse of notation.

A particularly useful case of this identity for $x_1 = x_2 = nd = 0$ is

$$\sum_q \frac{|\psi_q(0)|^2}{\omega - \omega_q} = -\frac{\pi i}{2k_\mathrm{r}}\rho(\omega)\psi^2_{q(\omega)}(0). \tag{3.40}$$

Moreover, these ideas can be extended to other integrals but we spare the reader from hearing about them as they won't be required for our analysis.

3.4.3 Emission into a lattice

Both, the PDR and SB approximations tend to be accompanied by a constant coupling g in the point-like emitter limit. This is not always well justified, especially so when more than two band-edges are taken into account. This is because of the existence of edges that host odd Bloch waves (see FIG. 3.9**c**). Since the parity of these Bloch waves is opposite to the parity of the QE at the center, the overlap between both cancels out exactly, regardless of the emitter size.

Thus, it is again necessary to consider momentum-dependent couplings g_q. In the case of a point-like GWF emitting matter waves, the coupling strength

$$g_q = \Omega\pi^{1/4}\sqrt{a_{QE}/2}\,\psi_q(0) \tag{3.41}$$

results from approximating the Bloch wave as constant across the QE in (2.4).

The transformed bath correlation function

$$\tilde{G}(\omega) = \sum_q \frac{i|g_q|^2}{\omega - \omega_q} = \frac{\Omega^2\pi^{3/2}a_{QE}}{4k_\mathrm{r}}\rho(\omega)\psi^2_{q(\omega)}(0) \tag{3.42}$$

then follows from (3.40). Capping the infinite products (3.31,3.32) with a cut-off $\Lambda \in \mathbb{N}$ in the number of gaps considered, we can re-express it as

$$\tilde{G}(\omega) = \kappa\sqrt{\Pi_{B/A}(\omega)} \tag{3.43}$$

where

$$\kappa = k_\mathrm{r}a_{QE}\frac{\Omega^2}{4}\sqrt{\frac{\pi}{\omega_\mathrm{r}}}, \qquad \Pi_{B/A}(\omega) = \Pi_B(\omega)/\Pi_A(\omega) \tag{3.44}$$

and

$$\Pi_A(\omega) = \prod_{n=0}^{\Lambda}(\omega - \omega_{An}), \qquad \Pi_B(\omega) = \prod_{n=1}^{\Lambda}(\omega - \omega_{Bn}). \tag{3.45}$$

We note that in practice it is enough to consider very low cut-offs (like $\Lambda = 2$ or $\Lambda = 3$) since the gaps both close and become off-resonant very fast (see FIG. 3.9**c**).

To find the poles of the IT for $\tilde{A}(\omega)$, we multiply the denominator from Eqn. (3.13) with its algebraic conjugate; the poles then correspond to zeroes of the polynomial

$$(\omega-\Delta)^2\Pi_A(\omega)+\kappa^2\Pi_B(\omega). \tag{3.46}$$

By considering the degree of this polynomial and its changes in sign between band edges, it is easy to see that there are no bound states in the continuum (BIC) [131], whereas each band gap (including $\omega < \omega_{A0}$) contains at least one pole. This differs from the multi-emitter case (see Sec. 3.5.2), where subradiance and retardation effects can lead to a BIC [58, 59]. For sufficiently weak couplings ($\kappa \ll \omega_{\mathrm{r}}^{3/2}$), these in-gap poles can be approximated as $\omega_n \approx \omega_{An} - \kappa^2\Pi_B(\omega_{An}) \;/\; [(\omega_{An}-\Delta)^2\prod_{m\neq n}(\omega_{An}-\omega_{Am})]$. There are two additional poles, approximately $\Delta \mp i\kappa\sqrt{\Pi_{B/A}(\Delta)}$, which lie in the same gap if they are real; otherwise one of them (ω_{M}) has negative imaginary part and can lead to Markovian (exponential) decay of the emitter, and the other (ω_{M}^*) is its complex conjugate.

In determining the spectral decay properties, see Fig. 3.11, we recall that not all of these poles contribute towards the residue theorem: due to the square root singularities at the band edges, we can visualize the integrand domain as a Riemann surface consisting of an 'upper sheet' where the integration paths in the complex plane are located and a 'lower sheet' on the other side of the branch cuts. Only the poles on the upper sheet will contribute towards the residue theorem and have a physical interpretation.

For positive lattice depths $s_b > 0$ and Markovian couplings $\Omega \ll \min_{q\in\mathbb{R}}|\Delta-\omega_q|$, the pole ω_n is in the upper sheet only when $\mathrm{sign}\{\Delta-\omega_{An}\} = (-1)^n$. Of the two extra poles, only one is in the upper sheet; in particular, ω_{M}^* cannot be there to avoid exponential growth of the population.

For larger couplings, there is still a change of sheets for one of the poles living in the $n^{th} > 0$ gap as Δ crosses the value ω_{Bn}. On the other hand, by increasing the coupling it is possible to make two lower poles co-located in a gap combine into a double pole and then split into a Markovian pole ω_{M} and its conjugate ω_{M}^*. Whereas ω_{M}^* always remains unphysical, ω_{M} can make it to the upper sheet, as depicted in Fig. 3.11**c**.

This figure reveals behavioral differences between the decay next to a band edge hosting even Bloch waves and one hosting odd ones. Whereas the former behaves as discussed in Sec. 3.2, the latter displays an increase in the Markovian component of the decay at non-Markovian couplings. One would naively expect that reabsorption and emission scale equally with the vacuum coupling; however, this is not the case here as BS formation is suppressed for these parameters (see Fig. 3.11**b**). Despite the phenomenological similarities, this *ultra-Markovian* emission is not to be confused with superradiance, as a single emitter is enough to create this effect. For illustration purposes, let us consider the following example. Under the same conditions as Fig. 3.11**b** and **c**, a quantum emitter with detuning $\Delta = \omega_{B1} + \frac{1}{5}\omega_{\mathrm{r}}$ and coupling $\Omega = \frac{5}{2}\omega_{\mathrm{r}}$ emits half of its population at only $t = 0.52/\omega_{\mathrm{r}}$ and it emits more than 90% ultimately. In contrast, while the initial decay is very similar at $\Delta = \omega_{A0} + \frac{1}{5}\omega_{\mathrm{r}}$ and $\Omega = \frac{5}{2}\omega_{\mathrm{r}}$, most of the radiation is reabsorbed at

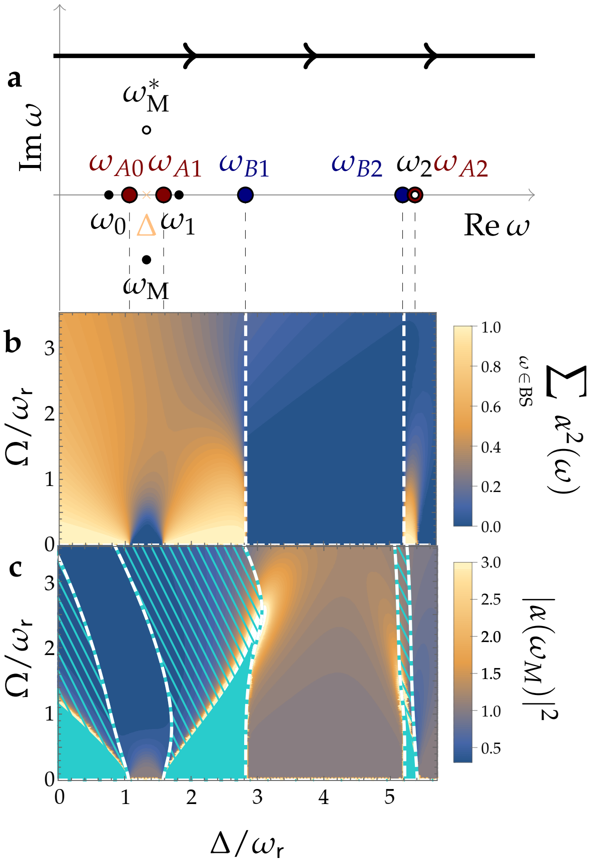

FIGURE 3.11: *Spectral emission properties of a point-like emitter coupled to a lattice.* **a,** Example of poles and branch cuts (dashed lines) of the IT of $\tilde{A}(\omega)$ for $s_a = 20\omega_r$, $s_b = 2.5\omega_r$, Rabi frequency $\Omega = \omega_r$ and a detuning Δ (in light orange) resonant with the first energy band. Black dots correspond to physical poles, whereas the white dots are unphysical and do not contribute to the dynamics. The branch points ω_{An} (dark red) and ω_{Bn} (dark blue) are the band edges hosting even and odd Bloch waves, respectively. The thick black line represents the integration contour of the transform. **b,** The sum of the squared residues of the bound states –an indicator of the population that remains bounded after emission– is presented as a color map on the Δ-Ω plane. Regions separated by the white dashed vertical lines $\{\Delta = \omega_{Bn}\}_{n=1}^{\infty}$ have a different number of bound states. **c,** Squared norm of the residue corresponding to the Markovian pole ω_M on the Δ-Ω plane. In the solid cyan regions there is no Markovian pole, whereas in the cyan dashed regions the pole is in the lower sheet. Figure reproduced from Ref. [51] with permission from the APS.

$t = 2.5/\omega_r$ and the emitter population subsequently oscillates with large amplitude as the system cycles between emission and reabsorption.

The integration path of $\tilde{A}$'s IT can be adapted to the singularities described in Fig. 3.11**a** by circling around the physical poles and branch cuts of the integrand[11], leading to the time evolution

$$A(t) = \sum_{\substack{p\in\text{upper}\\ \text{poles}}} \alpha(\omega_p) e^{-i\omega_p t} - \frac{i\kappa}{\pi} \sum_{n=0}^{\Lambda} (-1)^n e^{-i\omega_{An} t} I\left(\omega_{An}, t\right) + \frac{i\kappa}{\pi} \sum_{n=1}^{\Lambda} (-1)^n e^{-i\omega_{Bn} t} I\left(\omega_{Bn}, t\right) \tag{3.47}$$

where

$$\alpha(\omega) = \frac{2(\omega - \Delta)}{2(\omega - \Delta) + \kappa^2 \frac{d}{d\omega} \Pi_{B/A}(\omega)} \tag{3.48}$$

denotes the residue of the poles, and the branch contribution

$$I\left(\omega, t\right) = \int_0^{\infty} \frac{\sqrt{\Pi_{B/A}(\omega - i\gamma)}}{(\omega - i\gamma - \Delta)^2 + \kappa^2 \Pi_{B/A}(\omega - i\gamma)} e^{-\gamma t} d\gamma \tag{3.49}$$

---

[11] In the same fashion as we did in Sec. 3.2, FIG. 3.4**a**.

is well-defined and rapidly converging unless ω_{M} is on the branch cut. The branch contribution $I(\omega, t)$ tends to zero as the time t increases but does so algebraically, making the decay non-Markovian. The only contributions persistent in time, i.e. the bound states, are the real upper poles residing in the band gaps.

3.4.4 Phenomenology

The general features of the resulting time evolution are shown in Fig. 3.12**a**. It is mostly Markovian for detunings deep inside the bands and non-Markovian around the band edges; there is no decay deep inside the gaps. We note that emission is suppressed at the band edges ω_{Bn} of odd parity with respect to the edges ω_{An}, whose Bloch waves have the same parity as the emitter.

After the emission finishes, the remaining emitter population can oscillate by the beating of various bound states. This effect has been measured experimentally [91] and it is most noticeable in the center of the first energy band. We compare our calculation with the experimental data in Fig. 3.12**b**. As the coupling increases relative to the bandwidth,

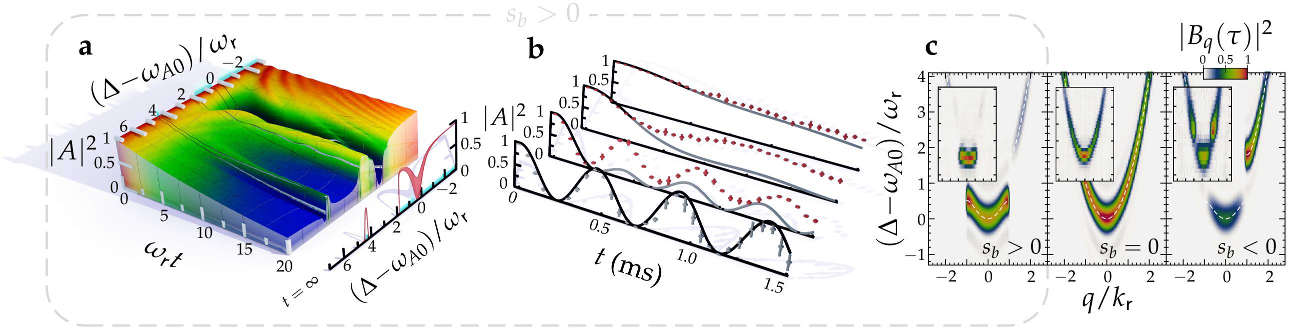

FIGURE 3.12: *Band structure effects in matter-wave decay.* **a,** Detuning dependence of the population decay $|A(t)|^2$, from one point-like emitter to a sinusoidal lattice of potential depth $s_b = 2.5$ and through a coupling $\kappa = 0.082\omega_{\mathrm{r}}^{3/2}$. Cyan marks indicate the position of the energy gaps. The time slice $t = \infty$ represents the range of the asymptotic population that remains bound after decay. **b,** Decay dynamics at the band center $\Delta = \omega_{C1}$ where the ratio between the average coupling g_q to the first band and the bandwidth is from back to front 0.09 (weak coupling), 0.215, 0.5 (intermediately coupled), and 2.45 (strongly coupled). The dots are data averaged over at least three experimental runs each, with error bars representing the standard error of the mean and bandwidths $\frac{1}{2}\omega_{\mathrm{r}} \approx 2\pi \times 1.8\,\mathrm{kHz}$ (red data) and $\frac{1}{10}\omega_{\mathrm{r}}$ (gray data). The gray lines represent the predictions of the single-emitter SB model, with its estimated range of applicability indicated in black. **c,** Quasi-momentum distribution $|B_q(\tau)|^2$ predicted for the emission by a single point-like emitter with $\kappa\omega_{\mathrm{r}}^{-3/2} = 0.015$, 0.032, and 0.015 into potentials with depth $s_b = 2.5$, 0, and -2.6 (respectively) at a fixed time $\omega_{\mathrm{r}}\tau = 9.24$. The insets reproduce the experimentally observed distributions for $s_b = 0$ [78] and $s_b \neq 0$ [91] measured for the same parameters. Figure panels **a** and **b** adapted from Refs. [51] and [91], respectively; **c** is reproduced from [51] with permission from the APS.

the oscillations intensify until the power broadening makes the band indistinguishable from a single state, resulting in perfect Rabi oscillations with the bound states taking the role of the dressed states of the oscillation [91].

An analogous formula to (3.47) can be written for the time evolution $B_q(t)$ of the emitted modes,

$$B_q(t) = -\frac{g_q}{2\pi i}\int_{-\infty+i0^+}^{+\infty+i0^+}\frac{e^{-i\omega t}\,\mathrm{d}\omega/\left(\omega-\omega_q\right)}{\omega-\Delta+i\kappa\sqrt{\Pi_{B/A}(\omega)}}. \tag{3.50}$$

The main difference is that the integration displays an additional pole at energy ω_q. We note that this real pole does not correspond to a bound state but rather to a mode that has completely abandoned the emitter and keeps traveling free indefinitely. This causes a similarity between the emission spectrum and the dispersion relation of the medium, that we show in Fig. 3.12**c**. Notice how the q-dependance of the coupling g_q greatly suppresses the emission to the second energy band for $s_b > 0$ ($[\omega_{B1}, \omega_{B2}]$, which hosts *quasi*-odd Bloch waves) in comparison with the second band $[\omega_{A1}, \omega_{B2}]$ in the $s_b < 0$ case, although they have practically the same dispersion relation ω_q.

Although the single-emitter model matches the observed decay dynamics at short times, it underestimates the amount of subsequent reabsorption seen in the experiment, in which the optical lattice provided an array of emitters. Subsequent oscillations are dominated by reabsorption as the emitted radiation spreads across the emitter array (see FIG. 3.17). More quantitatively [91], if we use the pole decomposition of (3.50) to split the emission into a bound and a decaying part, $B_q(t) = B_q^{\mathrm{BS}}(t) + B_q^{\mathrm{de}}(t)$, then the amount of decay into the n-th Wigner-Seitz (WS) cell is $B_n^{\mathrm{de}}(t) = \sum_q B_q^{\mathrm{de}}(t)\cos(nqd)$. The single emitter model is well applicable when this decay outside of the original WS cell is lower than 10% (i.e. $\sum_{n\neq 0}|B_n(t)|^2 < 0.1$; decay curves are drawn in black during this period in FIG. 3.12**b**). We note that at smaller couplings, the applicability of the theory for a single emitter extends to longer times, which was the case for the parameters of Fig. 3.12**c**.

3.4.5 Evanescent Bloch waves

One might expect that the presence of a lattice potential for the radiated modes induces a corrugation of the evanescent waves [37]. We can compute the spatial distribution of BWs bound to a point-like emitter[12]

$$B_x = \sum_q \frac{g_q A}{\omega-\omega_q}\psi_q(x) \overset{(3.39)}{=} -i\frac{A\Omega}{k_{\mathrm{r}}}2^{3/2}\pi^{5/4}a_{QE}^{1/2}\psi_{q(\omega)}(0)\psi_{q(\omega)}(|x|)\rho(\omega), \tag{3.51}$$

where we immediately identify $\psi_{q(\omega)}(|x|)$ (for ω in a gap) with an evanescent BW.

---

[12] We note that the same calculation can be performed with a GWF [51] adapting the steps outlined in FIG. 3.6 by replacing the plane wave with a Bloch wave (BW) and (3.22) with (3.39), but the result is more convoluted.

To further understand the shape of these waves, notice that by Bloch's theorem, every Bloch wave $\psi_{q\in\mathbb{R}}$ admits a representation $\psi_{q(\omega)}(x) = \psi_{q(\omega)}(0)u_{q(\omega)}(x)e^{iq(\omega)x}$ with $\psi_q(\omega)(0)$ acting as the holomorphic normalization factor in (3.32) and $u_{q(\omega)}(x) = u_{q(\omega)}(x+d)$ a periodic function that can be Fourier-decomposed into $\upsilon_n(\omega)$ (upsilon) coefficients. We reinterpret this as a plane-wave decomposition of the Bloch wave

$$\psi_{q(\omega)}(x) = \psi_{q(\omega)}(0)\sum_{n=-\infty}^{+\infty}\upsilon_n(\omega)e^{i(q(\omega)+2nk_\mathrm{r})x}. \tag{3.52}$$

Contrary to popular belief, band gaps are not devoid of momenta, but they are filled with momenta that are complex (see FIG. 3.13**a**). The decomposition above can be extended to the complex ω-plane, and in particular it can be extended to ω in the gaps

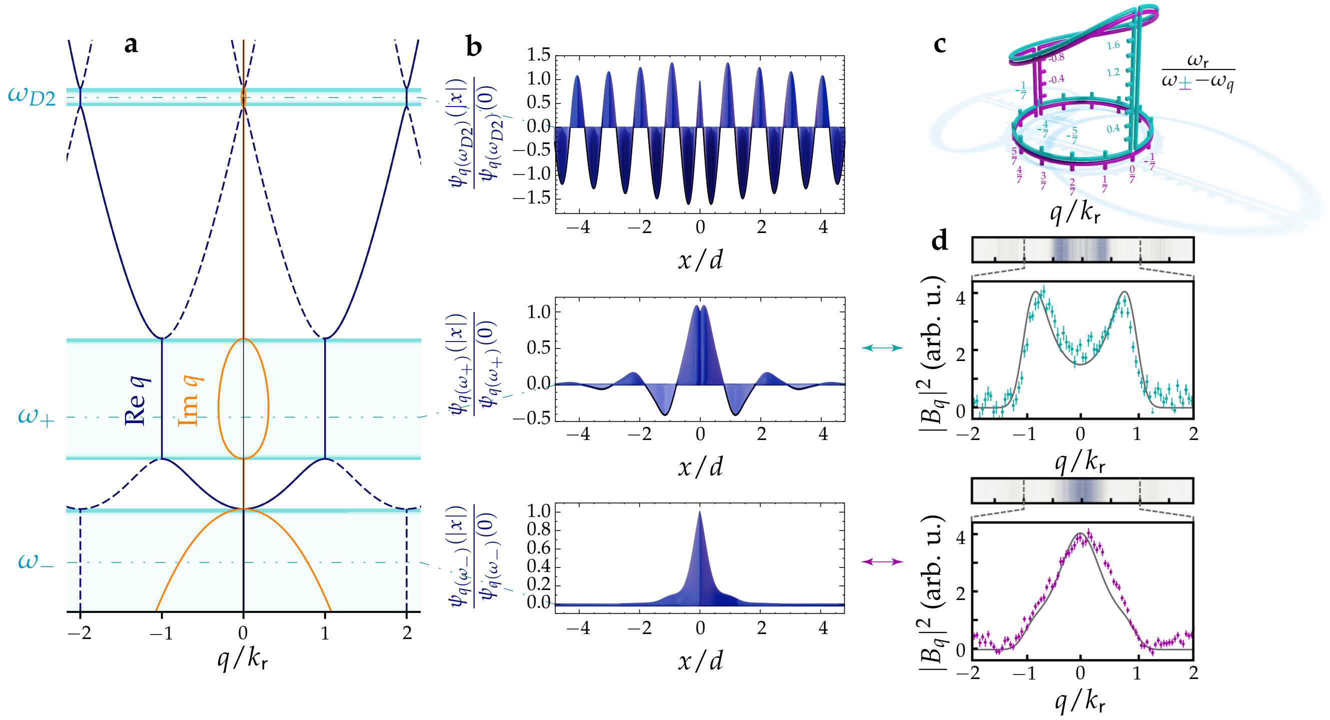

FIGURE 3.13: *Evanescent Bloch waves.* **a,** Real (in dark blue) and imaginary parts (in orange) of $q(\omega)$ along the bands and gaps of a lattice $s_b = 2.5$ deep. Solid lines denote the dominant momenta, whereas dashed lines denote other momenta that also fulfill the dispersion relation. Frequencies $\omega_\pm = \omega_{C1} \pm \frac{3}{4}\omega_\mathrm{r}$ and ω_{D2} are outlined. **b,** Space dependence of the evanescent Bloch waves at the outlined frequencies, hosted in the band gaps. **c,** Symmetry of the evanescent Bloch waves at $\omega_\pm$ under the SB approximation. We visualize their quasimomentum wavefunctions as two different cuts of the same strip. **d,** Adiabatically-generated evanescent Bloch matter waves at $\omega_\pm$. Each data point is the average of more than 30 individual repetitions. The strips show average band map ToF pictures. The gray curve is the wavefunction in **c** squared and convolved with a Gaussian blur ($\sigma_q = 0.15k_\mathrm{r}$) to accommodate finite size effects and imaging resolution. Figure **a** adapted from [51] and **d** reproduced from [91] with permission from the APS.

$\mathbb{R} \setminus \omega_{\mathbb{R}}$,

$$\psi_{q(\omega)}(|x|) = \psi_{q(\omega)}(0) \sum_{n=-\infty}^{+\infty} v_n(\omega) e^{i(q(\omega)+2nk_\mathrm{r})|x|}, \tag{3.53}$$

expressing an evanescent BW as a superposition of evanescent waves with all the complex momenta $q(\omega) + 2nk_\mathrm{r}$ fulfilling the dispersion relation in the gaps. The dominating momenta (especially so for shallow lattices $s_b < 1$) are those that are closest to fulfill the asymptotic PDR (shifted by $s_b/2$), which under our conventions are $q(\omega)$ and $q(\omega) - 2n_\mathrm{gap}k_\mathrm{r}$ with $n_\mathrm{gap} = 0, 1, 2, ...$ enumerating the gaps. Thus, $\mathrm{Re}\, q(\omega)$ gives the spatial frequency of the evanescent BW, whereas $\mathrm{Im}\, q(\omega)$ gives the spatial decay rate, and other harmonics give the expected corrugation (see FIG. 3.13**b**). As noted and measured in [91], and in the spirit of comparing a band structure with a cavity [37], these have the traits of stationary waves despite the absence of boundary conditions and thus they express as sharp peaks around $\pm n_\mathrm{gap}k_\mathrm{r}$ in the band mapping images (FIG. 3.13**d**). Measurements of this kind allow us to access the complex band structure of a lattice, which is also physical as we can see.

As different as they might seem, evanescent BWs below and above the ground band are symmetric under the SB approximation (see FIG. 3.13**c**). Considering energies $\omega_\pm$ symmetrically placed around the center ω_{C1} of the band, the symmetry follows by

$$\frac{\omega_\mathrm{r}}{\omega_+ - \omega_q} = -\frac{\omega_\mathrm{r}}{\omega_- - \omega_{q+k_\mathrm{r} \pmod{2k_\mathrm{r}}}}. \tag{3.54}$$

3.5 Multiemitter effects

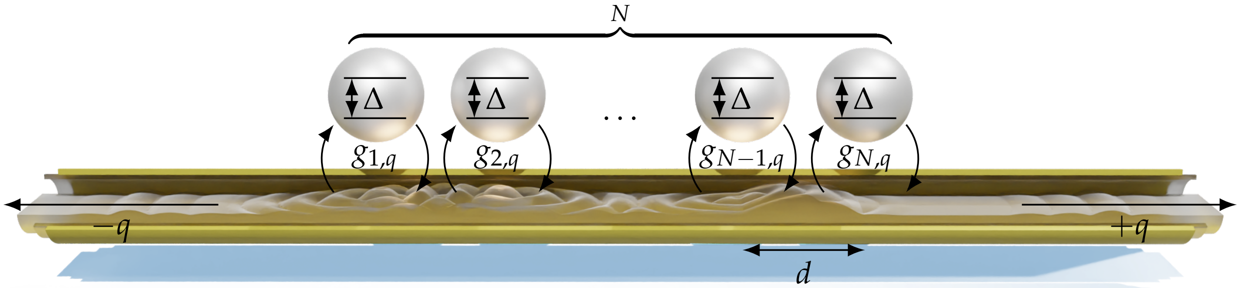

FIGURE 3.14: An *array of N identical QEs coupled to a waveguide*. The phase retardation of photons traveling between emitters induces additional non-Markovian dynamics, such as trapping radiation between emitters.

More generally, one can consider N emitters in the WWH forming an array of QEs [51, 56, 57] with additional non-Markovian effects rooted in the phase retardation (3.34) component of the coupling (2.4), which can be expressed as

$$g_{j,q} = e^{iqdj} g_q \tag{3.55}$$

by Bloch's theorem. The single excitation can now be spanned in the sub-basis

$$|\Psi(t)\rangle = \sum_{j=1}^{N} A_j(t)\hat{a}_j^\dagger |0\rangle + \sum_q B_q(t)\hat{b}_q^\dagger |0\rangle \,, \tag{3.56}$$

in which the TSE reads

$$\begin{cases} \omega\tilde{A}_j - A_j(0) = \Delta\tilde{A}_j + \sum_q g_{j,q}\tilde{B}_q \\ \omega\tilde{B}_q = \omega_q\tilde{B}_q + \sum_{j'} g^*_{j',q}\tilde{A}_{j'} \end{cases} \tag{3.57}$$

for an emission process ($B_q(0) = 0$). Using the equation below to substitute $\tilde{B}_q$ in the one above, yields

$$(\omega - \Delta)\tilde{A}_j - A_j(0) = -i\sum_{j'} \tilde{G}_{j-j'}(\omega)\tilde{A}_{j'} \tag{3.58}$$

where

$$\tilde{G}_{j-j'}(\omega) := \sum_q \frac{i|g_q|^2}{\omega - \omega_q} e^{iqd(j-j')} \qquad \forall\omega \notin \omega_{\mathbb{R}}. \tag{3.59}$$

Solving or further simplifying this equation involves linear algebra, as in matrix form the solution is simply

$$\tilde{\mathbf{A}} = \left((\omega - \Delta)\mathbb{1}_N + i\tilde{\mathbb{G}}(\omega)\right)^{-1} \mathbf{A}(0). \tag{3.60}$$

Following the IT, the spectrum of the system is composed of bound states whose frequencies ω satisfy the equation

$$\det\left((\omega - \Delta)\mathbb{1}_N + i\tilde{\mathbb{G}}(\omega)\right) = 0. \tag{3.61}$$

When analytically continued in the style of FIG. 3.4**a**, this equation also reveals the complex frequencies of the exponentially decaying states; whereas the algebraic decay has again the frequencies of the band edges [51]. However, a more detailed analysis needs to be done on a case-to-case basis.

We note that $i\tilde{\mathbb{G}}(\omega \in \mathbb{R} \setminus \omega_{\mathbb{R}})$ is Hermitian and therefore diagonalizable. If the diagonal basis is ω-independent, then it establishes a decoupled set of normal modes for the emitter array. Importantly, the characteristics of $i\tilde{\mathbb{G}}(\omega)$ are going to be tightly linked to the algebraic-analytic properties of the Toeplitz matrix [145]

$$\mathbb{T}_N(z) = \begin{pmatrix} 1 & z & \cdots & z^{N-1} \\ z & 1 & \cdots & z^{N-2} \\ \vdots & \vdots & \ddots & \vdots \\ z^{N-1} & z^{N-2} & \cdots & 1 \end{pmatrix}, \tag{TM}$$

which is diagonalizable by being symmetric. If $\mathbb{T}_N(z)$ has an eigenvalue or an invariant subspace that is independent of z, then so does

$$\tilde{\mathbb{G}}(\omega) = \sum_q \frac{i|g_q|^2}{\omega - \omega_q} \mathbb{T}_N(e^{iqd}) \tag{3.62}$$

and the subspace decouples its dynamics from array modes that are orthogonal to the subspace.

3.5.1 Two emitters coupled to a single band

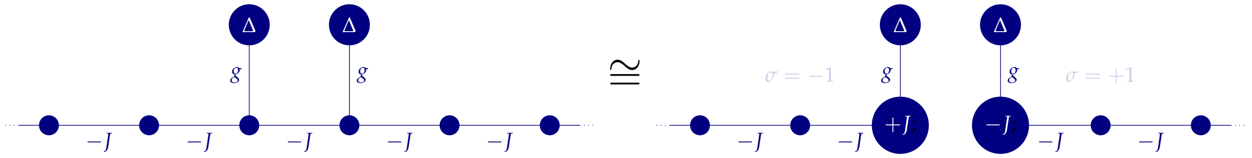

FIGURE 3.15: On the left, *adjacency graph* of two identical QEs coupled to a SB waveguide hosting one excitation in the Wannier basis. On the right, the system is equivalently described in the parity-explicit basis (3.64).

We start with a minimal scenario of one excitation distributed over two QEs ($N = 2$) coupled to a SB. The TM $\mathbb{T}_2(z)$ can always be diagonalized as

$$\begin{pmatrix} \frac{1}{\sqrt{2}} & \frac{1}{\sqrt{2}} \\ \frac{1}{\sqrt{2}} & -\frac{1}{\sqrt{2}} \end{pmatrix}^{-1} \begin{pmatrix} 1 & z \\ z & 1 \end{pmatrix} \begin{pmatrix} \frac{1}{\sqrt{2}} & \frac{1}{\sqrt{2}} \\ \frac{1}{\sqrt{2}} & -\frac{1}{\sqrt{2}} \end{pmatrix} = \begin{pmatrix} 1+z & 0 \\ 0 & 1-z \end{pmatrix}, \tag{3.63}$$

indicating that $(1, \pm 1)/\sqrt{2}$ are decoupled normal modes of the emitter array. This is because together with the number of excitations, the system also conserves the parity σ of an excitation that is distributed symmetrically ($\sigma = +1$) or antisymmetrically ($\sigma = -1$) over the two emitters. Thus, one can take decoupled bases for both cases,

$$|\psi_\sigma(t)\rangle = \frac{a_\sigma(t)}{\sqrt{2}} \left(\hat{a}_1^\dagger + \sigma \hat{a}_2^\dagger\right) |0\rangle + \sum_{j=2}^{\infty} \frac{b_{\sigma,j}(t)}{\sqrt{2}} \left(\hat{b}_{3-j}^\dagger + \sigma \hat{b}_j^\dagger\right) |0\rangle . \tag{3.64}$$

In this basis, the system behaves as two separate quantum emitters, each coupled to a separate half waveguide with an open- or closed-end (see FIG. 3.15). For an emission process ($a_\sigma(0) = 1$ and $b_{\sigma,j}(0) = 0$) and setting half the bandwidth as the natural frequency scale ($2J = 1$), the resulting transformed excitation amplitude of the emitter pair

$$\tilde{a}_\sigma(\omega) = \left(\omega - \Delta - \sigma g^2 + \sigma g^2 \frac{\sqrt{\omega - \sigma}}{\sqrt{\omega + \sigma}}\right)^{-1} \tag{3.65}$$

features decay to an 'even edge' at frequency $-\sigma$, where the parity of the emitter state matches that of the emitted waves, and to an 'odd edge' at σ, where the parity of the emitter state is incompatible with that of the emitted waves.

The singularities of Eqn. (3.65) encode the following single-excitation decay behaviors (cf. Fig. 3.25):

i. There is always a bound state in the gap beyond the even edge and no bound state in the continuum. Another bound state can be found in the gap beyond the odd edge if the detuning lies within this gap or the coupling is large enough ($g^2 > 1 - \sigma\Delta$).

ii. The band edges are a source of algebraic decay of order 3/2. More specifically, the even edge contributes asymptotically to $a_\sigma(t)$ with

$$\frac{(\sigma + i)e^{i\sigma t}}{4\sqrt{\pi}g^2 t^{3/2}} \tag{3.66}$$

while the odd edge contributes with

$$\frac{g^2(\sigma - i)e^{-i\sigma t}}{4\sqrt{\pi}\left(g^2 - 1 + \sigma\Delta\right)^2 t^{3/2}}. \tag{3.67}$$

An exception to this is the incidental case that $g^2 - 1 + \sigma\Delta = 0$, where the algebraic order of the odd edge changes to 1/2. Its influence becomes longer lived as the result of the spectral overlap between this edge and one of the bound states.

iii. The Markovian approximation is applicable for in-band detunings, $|\Delta| < 1$, with weak edge effects, $g^2 \ll 1 - |\Delta|$. In this limit the unemitted population $|a_\sigma(t)|^2$ decays through a single channel with an exponential rate $(1 - \sigma\Delta)\Gamma$, where $\Gamma = 2g^2/\sqrt{1-\Delta^2}$ is the decay rate of an isolated QE. The prefactor $(1 - \sigma\Delta)$ indicates that there is single-particle superradiance when $\sigma\Delta < 0$ and subradiance if $\sigma\Delta > 0$. No collective decay exists at $\Delta = 0$: in the band center, the symmetry between two parity sectors leads to a suppression of collective decay, in opposition to the naive idea that every system symmetry favors collective decay. These characteristics also hold for 2 excitations, see Section 3.6.2.

3.5.2 Bound states in the continuum

For point-like emitters[13], the sum in modes of (3.59) can be done by using Eqn. (3.39), resulting in

$$\tilde{\mathbb{G}}(\omega) = \kappa\sqrt{\Pi_{B/A}(\omega)}\mathbb{T}_N(e^{iq(\omega)d}). \tag{3.68}$$

---

[13] See Ref. [51] for a more general expression using GWFs which, again, can be obtained adapting the steps outlined in FIG. 3.6.

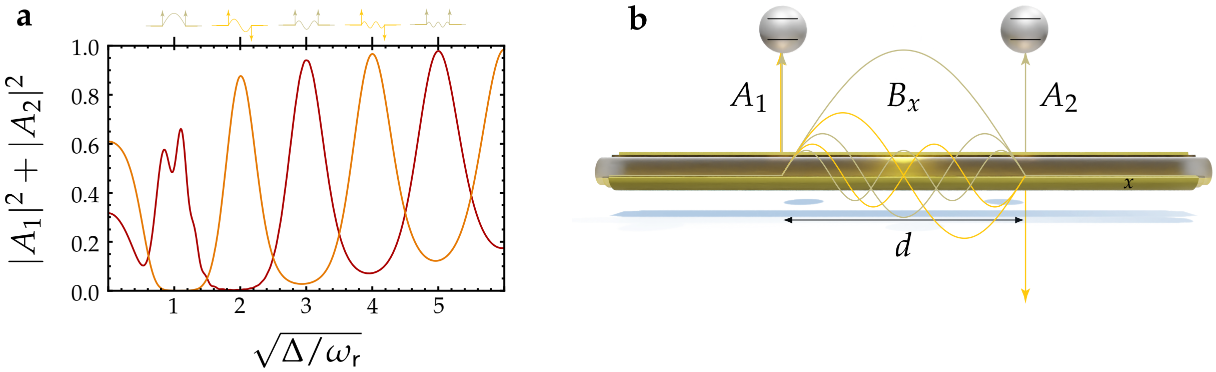

FIGURE 3.16: **a,** Above, the *bound states in the continuum* of two QEs are represented at different detunings in green olive (for even states) and yellow (for odd states). Arrows indicate the state of the emitters, and the line represents the state B_x of the equation, given by (3.71). Below, the remaining emitter array population of the symmetric array mode (in dark red) and the antisymmetric one (in dark orange) after a decay time of $15\omega_\mathrm{r}^{-1}$ under a coupling $g = 1/3$. **b,** Close-up representation of the same BICs.

Since $\det \mathbb{T}_N(z) = (1 - z^2)^{N-1}$, at $z = \pm 1$ the system is highly degenerate. To see this, consider that the range of $\mathbb{T}_N(\pm 1)$ is 1. This condition is only fulfilled for $\omega = \omega_n(0)$ or $\omega = \omega_n(k_\mathrm{r})$ which are normally band edges; but for $s_b = 0$, the frequencies $\omega_n(k_\mathrm{r}) = \omega_\mathrm{r} n^2 > 0$ are in the continuum. Thus fixing $\Delta = \omega_\mathrm{r} n^2$ makes the matrix $(\omega - \Delta)\mathbb{1}_N + i\tilde{\mathbb{G}}(\omega)$ highly degenerate, with $N - 1$ bound states in the continuum at $\omega = \omega_\mathrm{r} n^2$.

One might worry about the fraction of its momentum wavefunction

$$B_q = \frac{g_q^* \sum_j e^{-iqdj} A_j}{\omega_\mathrm{r} n^2 - \omega_q} \tag{3.69}$$

becoming singular due to a vanishing denominator in the case of a BIC, but this zero cancels exactly with one in the numerator as $\sum_j e^{-iq(\omega_\mathrm{r} n^2)dj} A_j = \sum_j (-1)^{nj} A_j = 0$ is the condition of $(A_j)_{j=1}^N$ belonging to the kernel of $\mathbb{T}_N((-1)^n)$.

Let us consider, for simplicity, the case of $N = 2$ QEs emitting into a PDR ($s_b = 0$). At zero detuning the system cannot be Markovian; but if it were, a symmetric emitter state would be superradiant and an antisymmetric one would be subradiant, as in Dicke's famous example [18]. As we increase the detuning, the super- and subradiant roles are switched every time that $0 < \sqrt{\Delta/\omega_\mathrm{r}} = n \in \mathbb{N}$ (see FIG. 3.16**a**). The subradiant state results in the formation of a BIC of parity $(-1)^{n+1}$. The state of the emitter array in such a BIC is thus $\left(A/\sqrt{2},(-1)^{n+1}A/\sqrt{2}\right)$ and the state of the radiation

$$\begin{aligned} B_q &\overset{(3.69)}{=} \frac{gA}{\sqrt{2}\omega_\mathrm{r}} \frac{e^{iqd/2}+(-1)^{n+1}e^{-iqd/2}}{n^2-(q/k_\mathrm{r})^2} \\ &= \frac{gA}{\sqrt{2}\omega_\mathrm{r}} \frac{\pi}{2n} \left(i^{n-1}\mathrm{sinc}\left[\frac{\pi}{2}\left(\frac{q}{k_\mathrm{r}}-n\right)\right] + i^{1-n}\mathrm{sinc}\left[\frac{\pi}{2}\left(\frac{q}{k_\mathrm{r}}+n\right)\right]\right) \end{aligned} \tag{3.70}$$

in momentum space or in position space,

$$B_x = \sum_q B_q \sqrt{\frac{k_\mathrm{r}}{\pi}} e^{iqx} = \begin{cases} \frac{gA}{n\omega_\mathrm{r}}\sqrt{\frac{\pi k_\mathrm{r}}{2}}\,\mathrm{Re}\left[i^{n-1}e^{ink_\mathrm{r}x}\right] & \text{if } x \in \left[-\frac{d}{2},\frac{d}{2}\right] \\ 0 & \text{otherwise,} \end{cases} \tag{3.71}$$

features a stationary wave of the same parity $(-1)^{n+1}$ that is completely trapped between the emitters, as if they formed a perfect cavity (see FIG. 3.16**b**).

3.5.3 Three matter-wave emitters and timed Dicke states

A strong point of the matter-wave (MW) platform is the capacity to create identical, equally-spaced quantum emitters. We saw indications of this in the decay data of FIG. 3.12**b**. Although the one-emitter model ($N = 1$) matches the observed decay dynamics at short times, it underestimates the amount of subsequent reabsorption seen in the experiment, in which the optical lattice provided an array of emitters. As discussed in [51, 91], the subsequent oscillations are dominated by reabsorption as the emitted radiation spreads across the emitter array. Using the formalism presented in this section, the presence of neighboring ground-state emitters (i.e. empty lattice sites) surrounding an excited emitter follows from the IT of (3.60), and already working with a lattice of three sites ($N = 3$) shows a marked improvement for the second oscillation. While it generally gets harder to analyze and numerically solve larger arrays, this is not the case for $N = \infty$ (which we present in Sec. 3.5.4). As shown in FIG. 3.17, the overall agreement with the experiment qualitatively improves further to longer time scales as N increases, but residual deviations persist. They have been attributed to differences in the initial state (the experiment worked with a sparsely populated array with more than one excitation) and

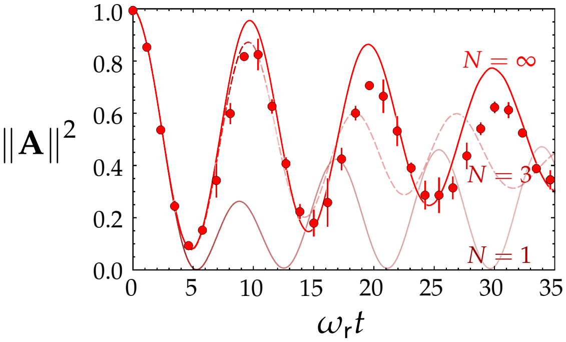

FIGURE 3.17: *Reabsorption of matter waves by empty neighbours*. The red dots indicate the same experimental values presented in FIG. 3.12**b** for intermediate coupling ($\kappa = 0.082\omega_\mathrm{r}^{-3/2}$). The lines denote the multiband multi-emitter theory (3.60,3.68) for an array of $N = 1, 3$ and ∞ point-like emitters, with only the central emitter originally excited. Figure reproduced from Ref. [51] with permission from the APS.

collisions between atoms [51].

Most recently [92], the mentioned decoherence of the ultracold atoms has been exploited to realize an effective model of three QEs radiating free matter waves. We analyze this case in this subsection. The excitation amplitudes of each emitter can be broken down as $(A_1, A_2, A_3) = I_1(t)/\sqrt{3}(1,1,1) + I_2(t)/\sqrt{3}(0,1,0)$ since the even parity of the initial state that we will consider, with the excitation equidistributed over all the QEs ($I_1(0) = 1, I_2(0) = 0$), is preserved throughout the decay. The exact time evolution is given by the IT of (3.60), which can be written in terms of the integrals

$$I_j(t) = \frac{(-1)^j}{2\pi i} \int_{-\infty+i0^+}^{+\infty+i0^+} e^{-i\omega t} \mathcal{G}_{2,3-j} \det{}^{-1} \mathcal{G} \mathrm{d}\omega, \tag{3.72}$$

where

$$\mathcal{G} = (\omega - \Delta)\mathbb{1}_2 + i \begin{pmatrix} \tilde{G}_0(\omega) + \tilde{G}_1(\omega) + \tilde{G}_2(\omega) & \tilde{G}_1(\omega) \\ \tilde{G}_1(\omega) - \tilde{G}_2(\omega) & \tilde{G}_0(\omega) - \tilde{G}_1(\omega) \end{pmatrix} \tag{3.73}$$

and

$$\tilde{G}_n(\omega) = -i\sqrt{\pi} \frac{\Omega^2 k_\mathrm{r} a_{QE}}{8\sqrt{-\omega\omega_\mathrm{r}}} e^{-(k_\mathrm{r} a_{QE})^2 \frac{\omega}{\omega_\mathrm{r}}} \left[e^{-n\pi\sqrt{-\frac{\omega}{\omega_\mathrm{r}}}} \operatorname{erfc}\left(k_\mathrm{r} a_{QE} \sqrt{-\frac{\omega}{\omega_\mathrm{r}}} - \frac{n\pi}{2 k_\mathrm{r} a_{QE}} \right) + n \leftrightarrow -n \right] \tag{3.74}$$

is the transformed bath correlation function (3.59) for an array of GWFs coupled to a PDR.

Analogous to FIG. 3.4**a**, these integrals can be decomposed using the residue theorem on the appropriate analytic continuation of $\mathcal{G}$. The decomposition includes a non-Markovian decay branch-cut at the continuum edge (at $\omega = 0$) and a set of infinite simple poles satisfying $\det \mathcal{G}(\omega_\mathrm{p}) = 0$. Most of these have small contributions and decay extremely fast (well beyond superradiant rates), but they provide a mechanism to avoid the "superradiant paradox" [59], as they help the initial decay to match the dynamics of a single emitter regardless of the detuning (cf. FIG. 3.18). This was first measured in [92] and means that, even if the decay dynamics is super- or subradiant, such character won't manifest until the radiation has reached the neighboring emitter.

Apart from these, we can identify 3 poles representing a bound state, a subradiant (sR), and a superradiant (SR) state. Their amplitudes are given by

$$\mathbf{A}_\mathrm{p} = \frac{e^{-i\omega_\mathrm{p} t}}{\sqrt{3}(\det \mathcal{G})'(\omega_\mathrm{p})} \begin{pmatrix} \mathcal{G}_{2,2}(\omega_\mathrm{p}) \\ \mathcal{G}_{2,2}(\omega_\mathrm{p}) - \mathcal{G}_{2,1}(\omega_\mathrm{p}) \\ \mathcal{G}_{2,2}(\omega_\mathrm{p}) \end{pmatrix}. \tag{3.75}$$

They are tabulated together with their corresponding frequencies in Table 3.1 for the following detunings, and their contributions to the decay dynamics are represented in FIG. 3.18.

At $\Delta = 0$, the diverging DoS causes strong non-Markovian behavior. An oscillation with near-maximum visibility is observed at these detunings, much stronger than that

$\Delta = 0$

p	BS_1	BS_2	SR
ω_p	$-0.22(2)$	$-0.10(1)$	$0.28(2) - 0.033(1)i$
$\mathbf{A}_{\mathrm{p},0}$	$\begin{pmatrix} 0.281(1) \\ 0.36749(1) \\ 0.281(1) \end{pmatrix}$	$\begin{pmatrix} 0.042(1) \\ -0.067(1) \\ 0.042(1) \end{pmatrix}$	$\begin{pmatrix} 0.214(4) + 0.100(4)i \\ 0.3460(7) + 0.0137(6)i \\ 0.214(4) + 0.100(4)i \end{pmatrix}$

$\Delta = \omega_\mathrm{r}$

p	BS	sR	SR
ω_p	$-0.010(2)$	$1.023(3) - 3(1) \times 10^{-6}i$	$1.041(9) - 0.11(2)i$
$\mathbf{A}_{\mathrm{p},0}$	$\begin{pmatrix} 0.009(1) \\ 0.010(2) \\ 0.009(1) \end{pmatrix}$	$\begin{pmatrix} 0.371(2) - 0.0039(5)i \\ 0.742(4) + 0.0013(2)i \\ 0.371(2) - 0.0039(5)i \end{pmatrix}$	$\begin{pmatrix} 0.237(5) + 0.044(2)i \\ -0.225(3) - 0.036(9)i \\ 0.237(5) + 0.044(2)i \end{pmatrix}$

$\Delta = 4\omega_\mathrm{r}$

p	BS	sR	SR
ω_p	$-0.019(4)$	$4.07(1) - 7(3) \times 10^{-6}i$	$4.09(1) - 0.10(1)i$
$\mathbf{A}_{\mathrm{p},0}$	$\begin{pmatrix} 0.0038(7) \\ 0.0043(8) \\ 0.0038(7) \end{pmatrix}$	$\begin{pmatrix} -0.000034(9) - 0.0036(5)i \\ -0.00020(5) + 0.0071(9)i \\ -0.000034(9) - 0.0036(5)i \end{pmatrix}$	$\begin{pmatrix} 0.611(4) + 0.042(8)i \\ 0.597(2) + 0.027(5)i \\ 0.611(4) + 0.042(8)i \end{pmatrix}$

TABLE 3.1: Complex frequencies ω_p (in units of ω_r) and initial amplitudes $\mathbf{A}_{\mathrm{p},0}$ of the bound (BS), subradiant (sR), and superradiant (SR) states involved in the decay of three matter-wave quantum emitters sharing a single excitation, for parameters as in FIG. 3.18. Table reproduced from [92].

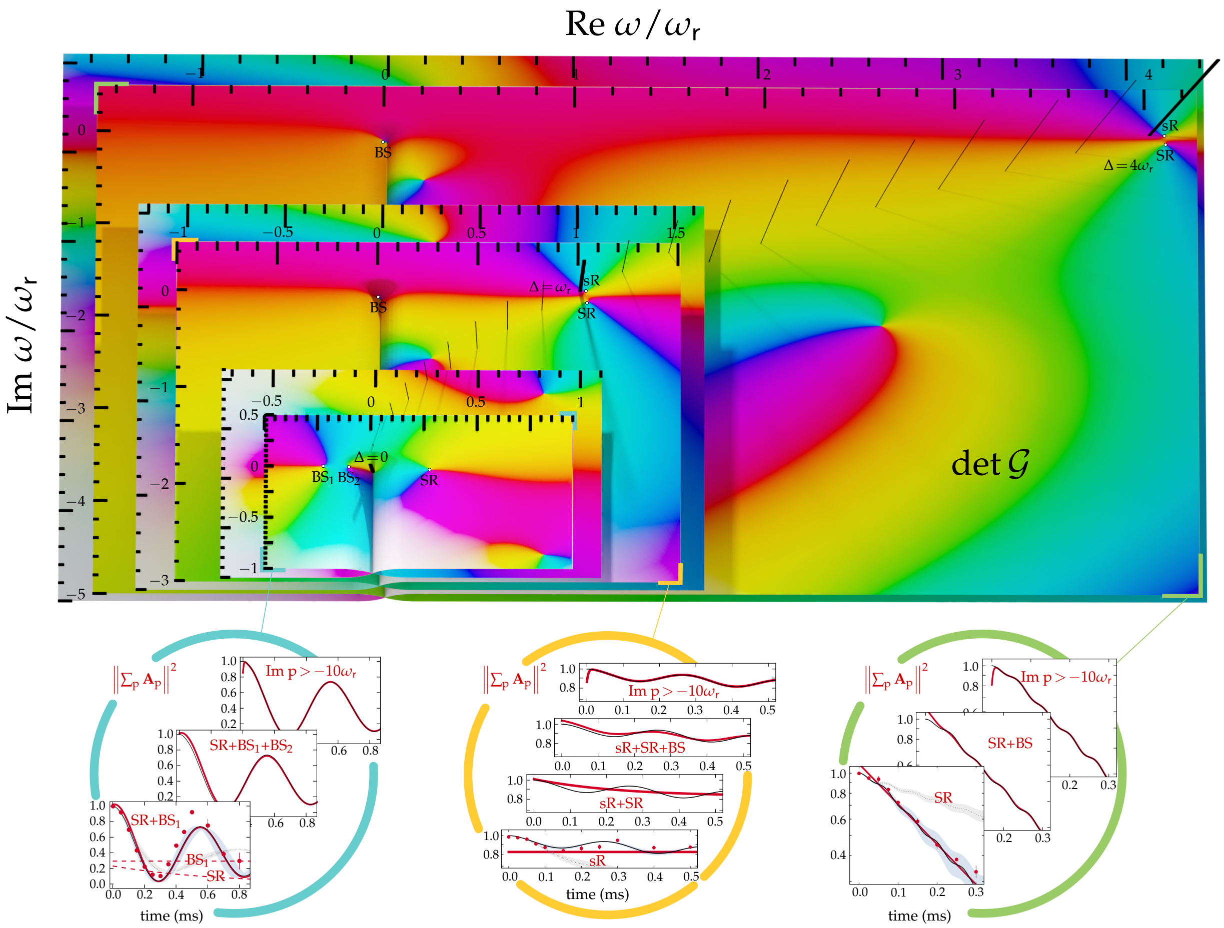

FIGURE 3.18: *Spectral components of the decay of 3 MW QEs.* The domain coloring plots of det $\mathcal{G}$ are represented on Riemann surfaces, along with their analytic continuations, for $s_a = 8$ and $(\Delta, \Omega)/\omega_r = (0, 0.6)$, (1,0.42) and (4,1) from left to right (the vertical bars represent the PDR $q(\Delta)$, to which the origin of the imaginary axis for each Δ is aligned). The zeroes and branch cut of this function define the decay dynamics of the emitters, which are presented in the bottom panels. The black lines represent the simulated dynamics, the gray dotted lines are predictions for a single emitter, the shaded regions account for experimental uncertainties in Ω, the red dots and error bars are experimental values [92], and red lines account for the various spectral contributions; with the main ones coming from superradiant (SR), subradiant (sR) and bound states (BS). Figure adapted from [92].

expected both for an isolated emitter (which shows fractional decay with damped, weak oscillations; see Sec. 3.2) and for an exited emitter surrounded by empty neighbors [78]. Instead, the behavior is that of a TDS with no phase lag strongly coupled to the $q = 0$ mode. Consequently, the momentum distribution of matter waves has been measured to be concentrated near $q = 0$ [92]. In position space, this corresponds to the radiation trapped inside the array including contributions from bound states, which remarkably, share the same gap. This feature does not appear with one or two symmetric emitters, and would ideally lead to persistent oscillations of very low frequency. They correspond to a redistribution of the population of the emitters from the center to the sides and back as if it were a vibration in a molecule of light.

At $\Delta = \omega_{\mathrm{r}}$ there is a mismatch between the phase lag of the TDS and the retardation of the MWs ($e^{i0} \neq e^{iq(\Delta)d}$) that makes the matter waves interfere destructively as they travel through the emitter array. One might thus expect the state to be strongly subradiant and indeed, the sR state has a dominant contribution. However, the non-Markovian character of the process results in also a significant SR contribution. We note that the subradiant state has an extremely small imaginary part: it is a quasi-bound state in the continuum (qBIC) [131]. The fact that matter-wave QEs have a finite size $a_{QE} > 0$ prevents this state from being perfectly bound and from having the ideal amplitude $\mathbf{A} \propto (1, 2, 1)^{\mathsf{T}}$, which otherwise allows for perfectly destructive interference between the three point-like emitters ($\sum_j (-1)^j A_j = 0$). In consequence, the qBIC distribution has two extremely narrow momentum peaks centered at $\pm \operatorname{Re} q(\omega_{\mathrm{sR}})$, as if mixing the properties of Markovian emission (Sec. 3.1) and BICs (Sec. 3.5.2).

At $\Delta = 4\omega_{\mathrm{r}}$, the interference between emitted and traveling MWs is again constructive ($e^{i0} = e^{iq(\Delta)d}$), thus one might expect superradiant decay with a rate factor equivalent to the number of emitters, $N = 3$. Since the detuning is deeply inside the continuum, the dynamics is quite faithful to this Markovian expectation and the dynamics is dominated by the superradiant state. The norm of this state being larger than 1 does not break the unitary evolution of the dynamics, as the state decays quickly and at short times the dynamics contains non-Markovian corrections to resemble a single emitter decay.

Other detunings can also be made super or subradiant by changing the phase lag ϕ between the emitters through Bloch oscillations (see Sec. 2.2.1 and FIG. 3.19**a**). Although the TDS $\hat{a}^{\dagger}_{\phi,N=3} |0\rangle$ can be analyzed in an analogous manner, the qualitative Markovian features of the emission spectrum can be understood as a combination of energy conservation and constructive interference: because of the former, the emission is constrained to the PDR, and because of the latter, it also peaks around the condition $\phi \equiv qd \pmod{2\pi}$. These measurements are presented in FIG. 3.19**b**. Notice that for lags ϕ that are not a multiple integer of π, superradiance is directional: a direct realization that the phase rotation of a system with a phase gradient can be transformed into linear movement. One might think about this as a quantum version of Archimedes' screw, in which the phase rotation of the QEs moves the matter waves in a particular direction. The directional emission of a matter-wave TDS is illustrated in FIG. 2.4 and its analogy with a classical mechanism is depicted in FIG. 3.19**c**. More details about the experiments and numerical simulations of collective matter-wave decay can be found in the PhD dissertation of Y. Kim [108]. For future experiments, it might be feasible to produce directional emission with a single chiral emitter [146] by simultaneously Floquet engineering the optical lattices and an additional optical tweezer [134].

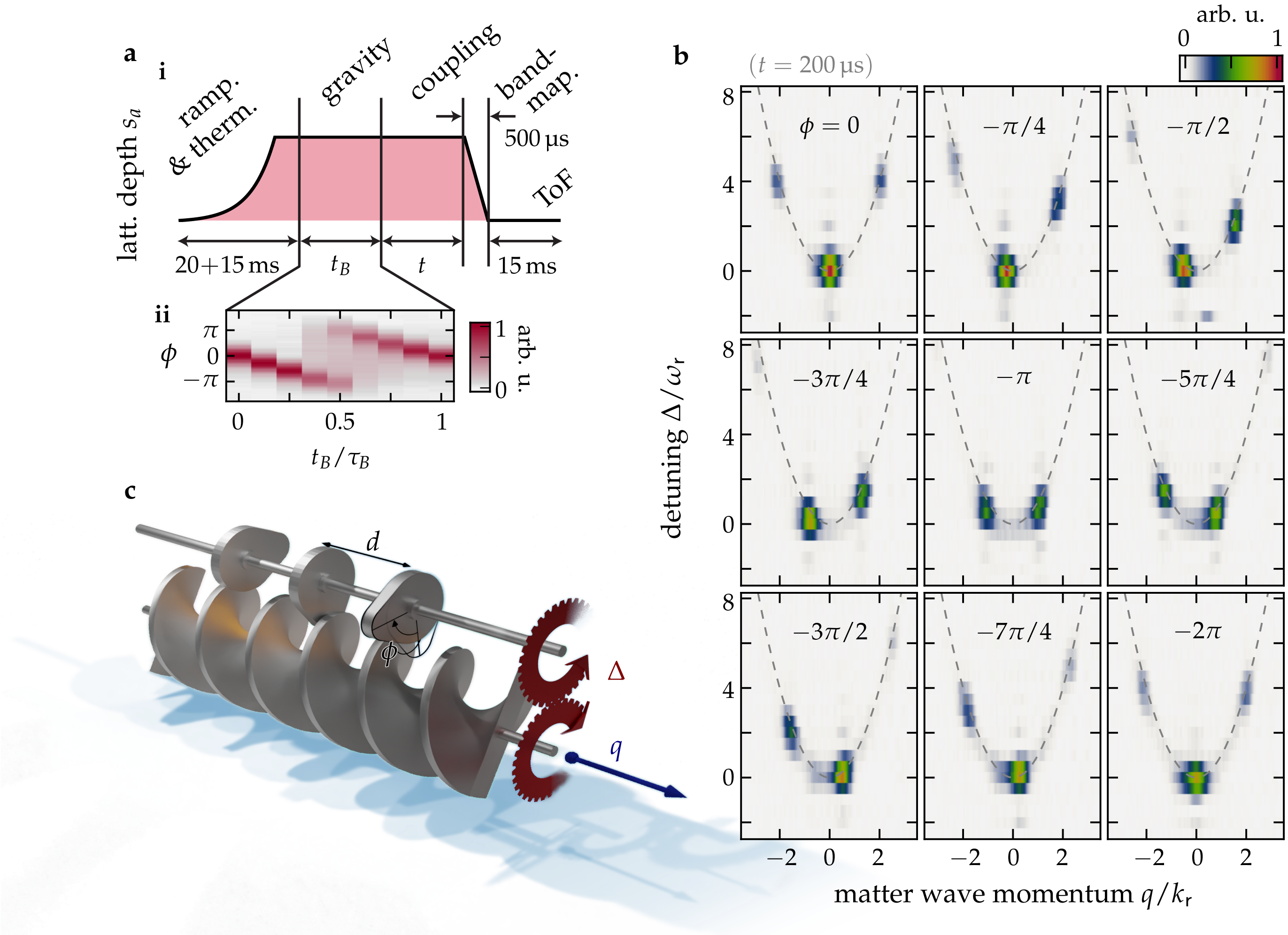

FIGURE 3.19: *Timed Dicke states.* **ai,** Experimental sequence for the creation and phase control of TDSs in the MW platform. After ramping up the optical lattice $(s_a, s_\perp) = (8, 0)$, a differential phase ϕ between emitters is gravitationally imprinted for a duration t_B (in units of the Bloch period $\tau_B = 2\pi\hbar/(mgd) = 1.2\,\mathrm{ms}$). Subsequently a 200-$\mu$s-long coupling pulse with strength $\Omega/\omega_r = 0.60(4)$ is applied to initiate the emission. **aii,** Phase distribution in the array population ($|r\rangle$, obtained via lattice band-mapping) as a function of t_B. **b,** Momentum distributions of emitted matter waves ($|b\rangle$) versus Δ, plotted for various ϕ, each panel is normalized independently. The dashed lines are the PDR of the matter waves. **c,** Mechanical analogy of the TDS $\hat{a}^\dagger_{\phi=-\pi/2,N=3}|0\rangle$. A camshaft of 3 cams separated by a distance d and turned at a relative angle Φ (representing the emitters) only engages a screw of a fitting thread (representing the radiation mode). The rotation of the camshaft with angular velocity Δ is transmitted to the screw, which can instill a linear momentum q to a fluid in only one direction. Figure panels **a** and **b** are reproduced from Ref. [92].

3.5.4 Polaritons

As the number of emitters increases, intra-array effects become more relevant until, in the limit $N \to \infty$, they are all there is. Contrary to what one may think, this case is the easiest to analyze: TDSs can no longer decay, as excitations cannot escape the influence of the emitters, and interference becomes so strong that these states decouple from one another. To prove this within our formalism, it is enough to notice that array vectors of the from $\mathbf{A} = (\ldots, e^{i\phi(j-1)}, e^{i\phi j}, e^{i\phi(j+1)}, \ldots)^\mathsf{T}$ are eigenstates of the TM $\mathbb{T}_\infty(z)$ regardless of z.

From a condensed-matter perspective, the WWH is invariant under discrete translations generated by $x \to x + d$, so by Bloch's theorem quasiparticles –known as polaritons [47, 147, 148]– must form together with a band structure. Remarkably, this is so even for coupling into free space ($V_b = 0$), as the periodicity of the QE array induces a periodicity in the waveguide. From this point of view, the condition of constructive interference $\phi \equiv qd \pmod{2\pi}$ in the TDS promotes to a law of conservation of quasimomentum $q = \phi/d$ for the polariton.

The transformed amplitude of these states follows from decoupling (3.60) as

$$\tilde{A}_q(\omega) = \left(\omega - \Delta + i\tilde{G}_q(\omega)\right)^{-1} A_q(0) \tag{3.76}$$

where the eigenvalue

$$i\tilde{G}_q(\omega) := \sum_{n=-\infty}^{+\infty} \frac{|g_{q+2k_\mathrm{r}n}|^2}{\omega_{q+2k_\mathrm{r}n} - \omega} \tag{3.77}$$

of $i\tilde{\mathbb{G}}(\omega)$ follows by taking into account its matrix elements (3.59) and using the identity $\sum_{j=-\infty}^{+\infty} e^{i(q'-q)dj} = 2k_\mathrm{r} \sum_{n=-\infty}^{+\infty} \delta(q' - (q + 2k_\mathrm{r} n))$.

As $\tilde{A}_q(\omega)$ lacks complex poles and branch cuts, its IT $A_q(t)$ is undecaying, in consistency with the idea that the polaritons can never escape the reach of the emitters. On the other hand, there is an infinite set of real poles $\{w_n(q)\}_{n=1}^{\infty}$ that can be identified with the polariton band structure and satisfy the equation

$$w_n(q) - \Delta + i\tilde{G}_q(w_n(q)) = 0. \tag{3.78}$$

Since all of the poles are real, plotting (3.78) –c.f. FIG. 3.20**a**– helps understanding several properties of the polariton band structure [37, 51]. For instance, polariton bands neither cross each other nor the original energy bands ($w_1(q) < \Delta$, $\omega_{n-1}(q) < w_n(q) < \omega_n(q)$ for $n \geq 2$), although they might cross the detuning at the points $\tilde{G}_q^{-1}(0)$ where the couplings to different bands cancel mutually. Excited polariton bands tend to these points in the limit of very large coupling; otherwise, they soon approximate the energy bands ($w_{n\gg 1}(q) \approx \omega_{n-1}(q)$).

The resulting band structure (purple lines in FIG. 3.20**b**) is exotic and cannot be obtained by a simple periodic potential. An indicator of this is the positive effective mass of both the ground and the first excited polariton band near $q = 0$.

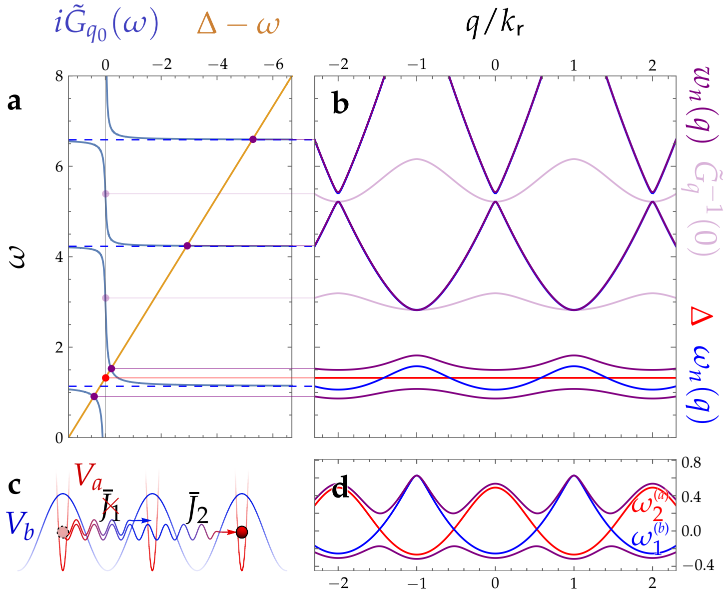

FIGURE 3.20: *Polariton band structure.* **a,** Graphical solution of (3.78) for the polariton bands at a particular quasi-momentum, $q_0 = -2.3k_{\mathrm{r}}$, with the same parameter values as FIG. 3.17 and with frequencies in units of ω_{r}. Polariton bands are located at the intersection between the orange and blue lines. **b,** Resulting polariton band structure $w_n(q)$ (in purple), for the band structure $\omega_n(q)$ (in blue) and detuning Δ (in red) specified in **a**. **c,** Schematic depiction of a particle in a state-dependent lattice with $s_a = 12$ and $s_b = -0.4949$ hopping two lattice sites due to the Rabi coupling $\Omega = 0.626\omega_{\mathrm{r}}$ between states. **d,** Polariton bands corresponding to the situation depicted in **c**, with a detuning of $0.0742\omega_{\mathrm{r}}$ between the centers of $\omega_1^{(b)}(q)$ and $\omega_2^{(a)}(q)$. Figure reproduced from Ref. [51] with permission from the APS.

The dynamical properties associated with these bands follow from applying the residue theorem to the IT of (3.76), which leads to

$$A_q(t) = \sum_{n=1}^{\infty} r_n(q) e^{-iw_n(q)t} A_q(0) \tag{3.79}$$

where the residues are given by

$$r_n(q) = \left(1 + i\tilde{G}_q'(w_n(q))\right)^{-1}. \tag{3.80}$$

The residues for bands far away from the detuning are negligible, rendering the structure of higher bands/gaps irrelevant for the dynamics. Alternatively, these results may also be obtained by decoupling the Hamiltonian [47] or as an ansatz in the SE, while taking into consideration that these residues satisfy the normalization condition ($r_n \in [0,1]$ and $\sum_{n=1}^{\infty} r_n(q) = 1$), energy conservation ($\sum_{n=1}^{\infty} r_n(q) w_n(q) = \Delta$) and $\sum_{n=1}^{\infty} r_n(q)/(\omega_m(q) - w_n(q)) = 0$. With this solution of the system, we can explain the dynamical behavior of the experimental data [78, 91] at longer evolution times $t \geq 1/J_b$ (see Fig. 3.17, case $N = \infty$).

The existence and properties of matter-wave polaritons in the MW platform were first predicted by the author [51] and experimentally confirmed shortly after by J. Kwon and

Y. Kim in our lab [118]. In the case of this newfound quasiparticle, as different quasi-momenta are decoupled unless they differ by an even multiple of the recoil momentum k_r, one can define a periodic momentum-dependent detuning $\Delta \equiv \Delta(q)$ to account more accurately for the dispersion relation $\omega_n^{(a)}(q)$ for the $|r\rangle$ states in the n^{th} band[14], while also modifying the vacuum coupling into $g_q = \Omega \left\langle \psi_{n,q}^{(a)} \middle| \psi_q^{(b)} \right\rangle /2$. From this perspective, one dresses the red and blue lattice through the microwave coupling, allowing more customization of the resulting polariton bands $w_{n'}(q)$ whose hopping rates

$$\bar{J}_j^{(n')} = -\sum_q w_{n'}(q) e^{iqdj} \tag{3.81}$$

can be freely tuned. An extreme example of this is shown in Fig. 3.20**c,d** where the first band of the $|b\rangle$ states is coupled with the second band of the $|r\rangle$ in a way that the polaritons hop two lattice sites at a time, without going through the intermediate site at all ($\bar{J}_1 = 0$, $\bar{J}_2 \neq 0$). The double hopping can be noticed in the emergent band structure by the (approximate) doubling in the periodicity of the bands. This opens the possibility for the analog simulation of J_1-J_2 quantum spin models [149, 150] with ultracold bosons in 1D, by inducing effective spin interactions [151–153]. We note that frustration [154], a core feature of the J_1-J_2 model, has kinetic origin in this case and is generated by coupling bands of opposite effective mass [155].

Although these properties are calculated in the single-excitation sector, the band structure also manifests in the many-body regime, where a BHM of renormalized hopping $\bar{J} \equiv \bar{J}_1^{(1)}$ and interaction energy $\bar{U}$ can form [118]. The higher mobility $(\bar{J} > J)$ of the MW polaritons –enhanced through the microwave coupling Ω and detuning Δ– can 'melt' a Mott insulator (MI) and make it undergo a quantum phase transition into a superfluid (SF) phase, as illustrated in FIG. 3.21**a**. The lattice depth s_a controls the hopping rate J, which directly influences the coherence of the atoms that, in turn, is reflected in the peak width σ of the ToF pictures. While the precise connection J-s_a can be computed, the dependence s_a-σ can studied with a reference measurement (FIG. 3.21**b**). The renormalization of this dependence induced by the microwave (FIG. 3.21**b-d**) then establishes an empiric confirmation of Eqns. (3.78, 3.81).

A deeper dive into the nature of matter-wave polaritons can be done by shaking the transverse lattice depth $s_\perp$ in the MI phase (see FIG. 3.21**e**). The choice of $s_\perp$ over s_a is intentional: as both states $|r\rangle$ and $|b\rangle$ are affected by this lattice, the interaction energy of both states (and between states) is perturbed coherently, avoiding unwanted dephasing. As a result, the process is reversible, except when the modulation frequency $\bar{\omega}$ is resonant with certain frequencies, such as the energy gap $\bar{\omega}_0$ between the center of the lower polariton (LP) band and the bottom of the upper polariton (UP) band (see FIG. 3.21**f**). The excitation spectrum is shown in FIG. 3.21**g**. In a reference run without coupling, excitation peaks can be observed at $\bar{\omega} \approx U/\hbar$ and $2U/\hbar$, as expected from resonant atom

---

[14] Typically $n = 1$ for the experiments, as the red lattice is very deep and the experiments start on the ground band, sometimes even purposely discarding the higher band contributions [78, 91]. However, other bands are more interesting from a theoretical perspective.

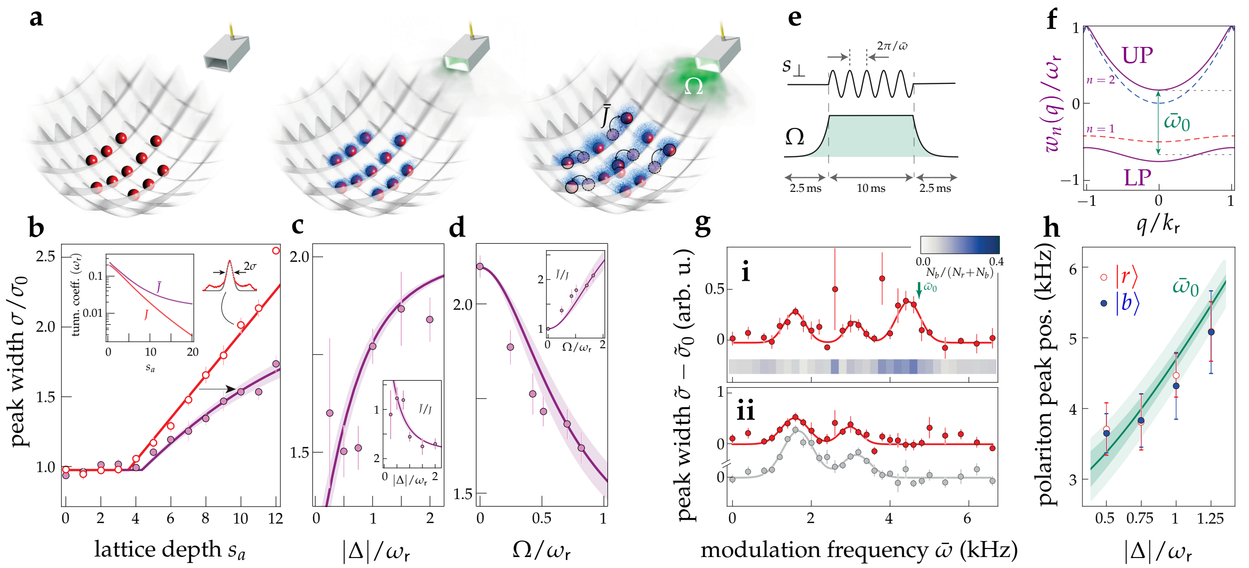

FIGURE 3.21: **a,** A Mott insulator of $|r\rangle$ atoms (left illustration) occupy the bottom of the harmonic confinement induced by a transversal lattice $s_\perp$ and a SDOL with $s_b = 0$. As the microwave is adiabatically turned on, atoms get dressed in $|b\rangle$ forming BSs (center illustration). As the microwave gets strong enough, atoms can hop with rate $\bar{J}$ between sites forming a superfluid of *matter-wave polaritons* (right illustration). **b,** Scan over s_a for $s_\perp = 18$, $\Delta/\omega_r = -0.50(7)$, and $\Omega/\omega_r = 0.84(2)$ (purple), compared to a reference measurement with $\Omega = 0$ (red). Plotted is the fitted 1D Gaussian width σ of the central diffraction peak in ToF (right inset). The red curve is a piece-wise linear fit with zero slope on the left segment, which is used to establish the relationship between σ and s_a. The purple curve is obtained from the red curve after shifting $s(J)$ (black arrow) according to the expected renormalization of hopping J to $\bar{J}$ (left inset); the shaded area accounts for the experimental uncertainties in Δ and Ω. **c, d,** Parameter scans at $s_a = 10$ with either variable Δ at $\Omega/\omega_r = 0.84(2)$ (**c**), or variable Ω at $\Delta/\omega_r = -0.50(7)$ (**d**). The theoretical prediction reflecting experimental uncertainties is shown as a solid purple line surrounded by shaded areas. They also include insets showing the corresponding ratios $\bar{J}/J$. **e,** Experimental sequence for the spectral excitation of the Mott insulator ($s_\perp = 40$, $s_a = 14$). After ramping up Ω adiabatically, $s_\perp$ is modulated by ±30% at variable frequency $\bar{\omega}$ for 10 ms. Then Ω is turned back down. **f,** Two lowest polariton bands ($n = 1, 2$, in purple) calculated for $s_a = 10$, $\Omega/\omega_r = 1$ and $\Delta/\omega_r = -0.5$. The green arrow denotes the separation $\bar{\omega}_0$ from the middle of the lower band to the bottom of the upper band. The dashed curves reproduce the atomic band structure. **g,** Excitation spectra following sequence **e** for $\Delta/\omega_r = -1.00(7)$ and $\Omega/\omega_r = 1.09(2)$, with the inset stripe showing the number of $|b\rangle$ atoms (**i**); or for the uncoupled case $\Omega = 0$ (red) and lower depth s_a=10 (gray) (**ii**). Error bars show the standard error of the mean with horizontal bars being smaller than the size of the data points. All data points are the average over at least 3 runs. **h,** Detuning dependence of the third excitation feature. Open red circles denote the $|r\rangle$ peak position, and blue dots denote the position of the maximum transfer of $|b\rangle$ atoms, as extracted from Gaussian fits, with error bars representing the spectral width (2σ) of the excitation feature. The green curve is the calculated polariton excitation energy $\bar{\omega}_0(\Delta, \Omega)$, where the shaded areas include (in darker green) the width of the ground band and (in lighter green) the uncertainties in Δ (±0.27 kHz) and Ω (±2%). Figure panels **b**-**h** are reproduced from Ref. [118] with permission from Springer Nature.

redistribution between sites [156]. The coupling has no noticeable effect on the position of the peaks, suggesting that for the parameters used (Ω, $|\Delta| \sim \omega_\mathrm{r}$) the change of the on-site energy is small ($\bar{U} \approx U$). However, an additional feature appears, centered around $\bar{\omega}_0$ (see FIG. 3.21**h**), accompanied by excess $|b\rangle$ population left after the coupling is ramped back down. This excess represents matter-wave shedding caused by the resonant excitation of the LP band. More details about the experiments on matter-wave polaritons can be found in the PhD dissertations of J. Kwon [107] and Y. Kim [108].

3.6 Multiexcitation effects

This section reproduces the study [70] on the consequences of having more than one excitation in a wQED system, replicating it verbatim, or adapting the ideas for a more consistent discussion and adding new explanations (see Section 3.6.4). In either case, they consist of original ideas developed by the author.

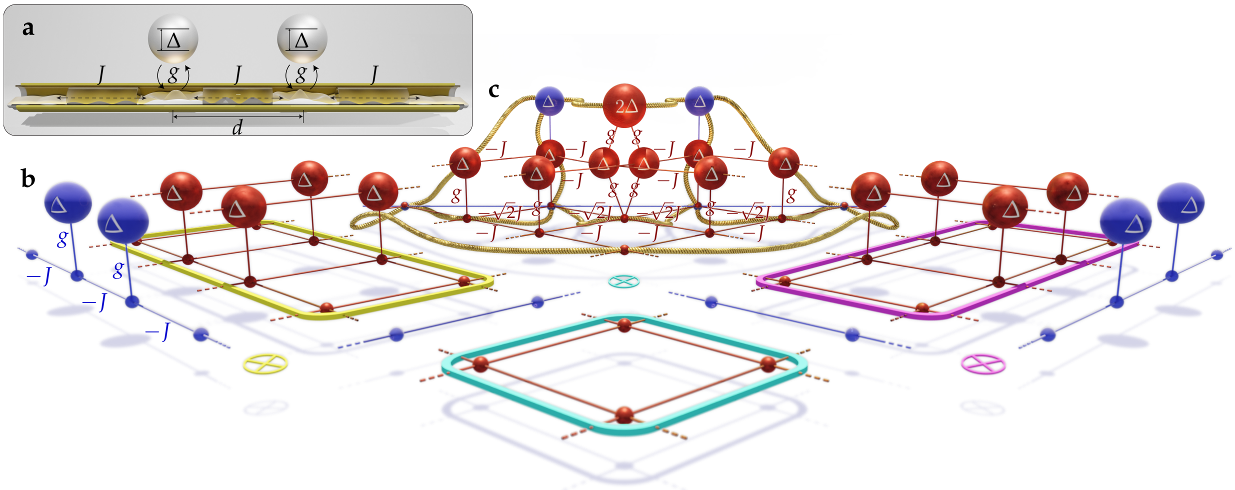

FIGURE 3.22: *Two-excitation sector* of a $N = 2$ wQED system. **a,** Two quantum emitters coupled to a waveguide. The strong periodic modulation of the index of refraction in the waveguide induces a single-band dispersion relation for the photons inside. **b,** Adjacency graph of the matrix representation of the system Hamiltonian restricted to a single excitation (in blue) and two excitations (in red). The connection between the two is given by strings with two blue nodes at the sides and a red node at the center. For clarity, some of the strings are omitted. **c,** Three asymptotic regions of the red graph that can be decoupled as tensor products between the blue graph of either the system and the waveguide (yellow and magenta regions) or twice the waveguide (cyan region). Figure reproduced from [70].

In his seminal work [18] Dicke departed from the classical idea of emitters decaying independently. He showed that, despite the lack of photon-to-photon interactions, quantum emitters might be mutually influenced by sharing the same electromagnetic modes, thus decaying collectively. From the Markovian point of view, the field modes establish decay channels that might be super- or subradiant, but this picture is also incomplete. Given that there is only a semantic difference between a quantum emitter reabsorbing a photon in a certain mode and the mode emitting the excitation back into the quantum emitter, the reabsorption of photons can only be accounted for by placing modes and emitters at the same level in the spirit of the WWH [8, 9]. Collective non-Markovian decay is the natural next step in the study of superradiance, where the "collective" not only refers to the quantum emitters but the emitters and field modes altogether.

As demonstrated in previous sections, several factors can cause and modify non-Markovian decay, such as a strong coupling between the emitters and the bath of electromagnetic modes [135, 157], a structured bath [37, 40, 45] with one [50] or multiple energy bands [51], the topology [52] and dimensionality [49] of the bath, the size [53–55] and the arrangement [51, 56, 57] of the emitters, and the delay of radiation traveling between them [58–63]. Such effects could become prominent in large quantum networks [61, 158]; but despite rapid experimental advancements on multi-excitation super- and subradiance [71], their interplay with non-Markovian dynamics is an incipient area of experimentation [92].

Theoretical studies of collective non-Markovian effects in quantum optics rely on effective Hamiltonians [47, 64, 65], numerical methods [50, 63, 66, 159], Feynman diagrams [67–69] or analytic approximations [61]. While these approximate methods tend to be simpler and more versatile, an exact solution would benefit the field in many ways: providing checkpoints for the approximated methods, inspiring new ansätze for related problems, unveiling hidden symmetries and new phenomena, and developing mathematical tools to approach the problem. But the solvability of non-Markovian systems beyond the single-excitation sector is unclear [47, 50, 160], as an infinite number of modes makes the dimension of the Hilbert space diverge and the collective nature of the decay couples the dynamics of the individual excitations through effective interactions caused by photon blockade.

Due to the enormous difficulty of the topic, we will restrict ourselves to providing an exact solution of collective non-Markovian decay for a minimal system featuring two adjacent quantum emitters spontaneously radiating two excitations into a one-dimensional SB waveguide. We provide techniques to analyze and solve this problem and emphasize the connection between the sectors with one and two excitations. The solution has a plethora of features: multiple super- and subradiant states, algebraic decay, mixed algebraic and exponential decay, fractional decay with bound states in and out of multiple continua, as well as logarithmic corrections to the algebraic decay. We also establish a simple criterion to ascertain the presence of collective non-Markovian decay.

3.6.1 The two excitation sector

We consider the same system as in Sec. 3.5.1: two identical QEs coupled by g to a 1D structured waveguide (or coupled-cavity array [121]) with period d and hopping rate J. The dispersion relation of the waveguide features a SB. The excitation energy $\hbar\Delta$ of the

QEs is best interpreted as the detuning Δ from the middle of this band, as it can also have a negative value. The QEs are fixed to adjacent lattice sites of the waveguide (represented in FIG. 3.22**a**).

Such a system is described by a WWH, which in the Wannier basis reads as

$$\hat{H}/\hbar = \Delta \sum_{j=1}^{2} \hat{a}_j^\dagger \hat{a}_j - J \sum_{j=-\infty}^{\infty} \left(\hat{b}_j^\dagger \hat{b}_{j+1} + \hat{b}_j \hat{b}_{j+1}^\dagger\right) + g \sum_{j=1}^{2} \left(\hat{a}_j \hat{b}_j^\dagger + \hat{a}_j^\dagger \hat{b}_j\right), \tag{3.82}$$

where $\hat{a}_j^\dagger = |1_j^a\rangle \langle 0|$ is a fermionic creation operator and $\hat{b}_j^\dagger = |1_j^b\rangle \langle 0| + \sqrt{2}|2_j^b\rangle\langle 1_j^b| + ...$ is a bosonic one.

We will study the dynamic evolution when the two emitters start off excited. Since the Hamiltonian conserves the number of excitations, we could expand it in the sub-basis of two-excitation states

$$\begin{aligned} |\psi(t)\rangle =& A(t)\hat{a}_1^\dagger \hat{a}_2^\dagger |0\rangle + \sum_{j<j'} B_{j,j'}(t)\hat{b}_j^\dagger \hat{b}_{j'}^\dagger |0\rangle \\ &+ \sum_{j=-\infty}^{\infty} B_{j,j}(t) \left(\tfrac{1}{\sqrt{2}}\hat{b}_j^\dagger \hat{b}_j^\dagger\right) |0\rangle + \sum_{j,j'} C_{j,j'}(t)\hat{a}_j^\dagger \hat{b}_{j'}^\dagger |0\rangle , \end{aligned} \tag{3.83}$$

where $A(0) = 1$ and $B_{j,j'}(0) = C_{j,j'}(0) = 0$. The factor of $1/\sqrt{2}$ is necessary to make the basis orthonormal.

Following the above approach results in a large, sparse matrix representation of the Hamiltonian. To gain insight into the underlying geometry, without necessarily computing this matrix, we introduce a graphical representation of the problem, illustrated in FIG. 3.22. We start with the adjacency graph of the Hamiltonian for a single excitation (FIG. 3.22**b**, in blue), which resembles the actual system (FIG. 3.22**a**). Then we denote two-excitation states by drawing strings between any two points of this graph. Because of fermionic exclusion, no such string can be drawn with both ends at the same QE single-excitation basis state (represented as a blue ball with a Δ). To produce the nodes of a new graph representing two-excitation states, we mark the centers of these strings (in red) with the total energy of the state, which is given by the sum of energies at the two ends of the string due to the absence of interactions between excitations (other than fermionic exclusion in the emitters).

Edges in the blue graph induce corresponding edges in the red graph. More specifically, every excitation experiencing coupling or hopping is represented by not only a blue edge but also several red ones, one for every two-excitation state containing the excitation. The induced transition rates are identical to the original rates, except for an additional factor of $\sqrt{2}$ when either the initial or final configuration contains two excitations in the same site (bosonic enhancement).

The resulting red graph is the adjacency graph of the Hamiltonian restricted to the subspace of two excitations; despite the 1D nature of the waveguide, the graph resembles that of a coupled 2D system. There are asymptotic regions that factor into tensor products of simpler graphs. Those simpler graphs are (1, in yellow and magenta) the original blue graph, and the one corresponding to an emitterless waveguide containing a single excitation, or (2, in cyan) two such emitterless waveguide graphs. Physically, this decomposition implies that the two excitations are independent and distinguishable when they are infinitely apart. These decompositions will be instrumental in finding and interpreting the general solution, which justifies why we solved the single-excitation case first (see Sec. 3.5.1).

We emphasize that the bosonic/fermionic properties of the particles are engraved in the geometry of this diagram. As a result, even a classical (non-planar) circuit board [161] following this graph could serve to test and simulate the dynamics of this quantum system.

3.6.2 The master equation approach

Collective decay [18] has been traditionally approached through reduced density matrices that obviate the evolution of the waveguide, treating it as a photon sink. Here we present such a Markovian approach [163] for completeness.

When each of the QEs is holding an excitation there is no phase relation between the two excitations, despite the initial state seeming symmetric. This allows for the system to decay into either the symmetric or anti-symmetric decay channels presented in Sec. 3.5.1***ii*** (see FIG. 3.23).

The density matrix $\rho = \mathrm{Tr}_B \left|\psi\right\rangle \left\langle\psi\right|$ resulting from partial-tracing over the waveguide subsystem B follows a dynamics that in the Markovian limit are described by the master equation [163]

$$\dot{\rho} = -i\left[\sum_{j=1}^{2} \Delta \hat{a}_j^\dagger \hat{a}_j, \rho\right] + \sum_{\nu=1}^{4} \frac{\Gamma_\nu}{2}\left(2\hat{O}_\nu \rho \hat{O}_\nu^\dagger - \rho \hat{O}_\nu^\dagger \hat{O}_\nu - \hat{O}_\nu^\dagger \hat{O}_\nu \rho\right), \tag{3.84}$$

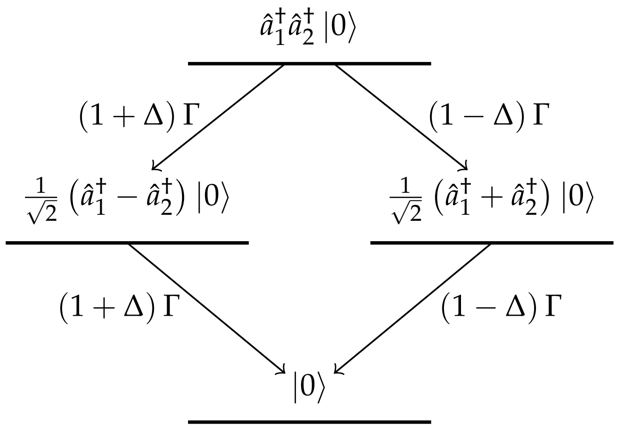

FIGURE 3.23: *Decay channels* and rates for the superradiant cascade of two excitations leaving two emitters through the coupling to a single sinusoidal band. Figure inspired by [162] and reproduced from [70].

where ν runs over the decay channels of FIG. 3.23, for example $\Gamma_1 = (1+\Delta)\Gamma$ and $\hat{\mathcal{O}}_1 = \sqrt{1/2}\left(\hat{a}_1^\dagger - \hat{a}_2^\dagger\right)|0\rangle\langle 0|\,\hat{a}_1\hat{a}_2$. This results in a 4×4 density matrix that is diagonal in the implied parity-explicit basis and describes exponential decay of the total population of the emitters,

$$\mathrm{Tr}\left(\hat{a}_1^\dagger\hat{a}_1 + \hat{a}_2^\dagger\hat{a}_2\right)\rho = \frac{1-\Delta}{1+\Delta}e^{-(1-\Delta)\Gamma t} + \frac{1+\Delta}{1-\Delta}e^{-(1+\Delta)\Gamma t} - \frac{4\Delta^2}{1-\Delta^2}e^{-2\Gamma t}. \tag{3.85}$$

We note that this decreases monotonically, so although they cooperate, two distant quantum emitters are not enough to produce a superradiant burst [164].

The decay channels illustrated in FIG. 3.23 become identical at $\Delta = 0$, and (3.85) reduces to the decay of two independent emitters. This signals a suppression of the collective effects, similar to the single-excitation case discussed in Section 3.5.1.

Another relevant observable (see Section 3.6.6) is the probability of finding exactly one excitation in the emitters,

$$\mathrm{Tr}\left(\hat{a}_1^\dagger\hat{a}_1 + \hat{a}_2^\dagger\hat{a}_2 - 2\hat{a}_1^\dagger\hat{a}_2^\dagger\hat{a}_1\hat{a}_2\right)\rho = \frac{1-\Delta}{1+\Delta}e^{-(1-\Delta)\Gamma t} + \frac{1+\Delta}{1-\Delta}e^{-(1+\Delta)\Gamma t} - 2\frac{1+\Delta^2}{1-\Delta^2}e^{-2\Gamma t}. \tag{3.86}$$

The global maximum of this function is 0.5 at $\Delta = 0$ and $\Gamma t = \log 2$, so any evidence of a higher value would signal physics beyond the Markovian approximation.

3.6.3 Secular equations

The SE for (3.83) simplifies when written in terms of the transformed field $|\tilde{\psi}(\omega)\rangle$ and then brought to a form that accommodates the asymptotic solutions of the system (see Sec. 3.6.1). For this purpose, we introduce the Bloch modes of the waveguide via $\hat{b}_q = \sum_j e^{-iqd(j-3/2)}\hat{b}_j$, where $q \in (-k_\mathrm{r}, +k_\mathrm{r}]$ is the quasimomentum (restricted to the first BZ because we only consider one band). Also, for simplicity and without loss of generality, we use the hopping rate to establish a natural frequency scale $2J = 1$. The transformed wavefunction in this picture is described by a set of amplitudes

$$\begin{aligned}|\tilde{\psi}(\omega)\rangle = {}& \tilde{A}(\omega)\hat{a}_1^\dagger\hat{a}_2^\dagger|0\rangle + \sum_{p<q}\tilde{B}_{p,q}(\omega)\hat{b}_p^\dagger\hat{b}_q^\dagger|0\rangle \\ & + \sum_q \tilde{B}_{q,q}(\omega)\left(\tfrac{1}{\sqrt{2}}\hat{b}_q^\dagger\hat{b}_q^\dagger\right)|0\rangle + \sum_{j,q}\tilde{C}_{j,q}(\omega)\hat{a}_j^\dagger\hat{b}_q^\dagger|0\rangle\end{aligned} \tag{3.87}$$

that are connected by (see Appendix A)

$$\begin{cases} \tilde{A} = \frac{1}{\omega-2\Delta} + \frac{g}{\omega-2\Delta} \sum\limits_{q} \left(e^{-\frac{iqd}{2}} \tilde{C}_{2,q} + e^{\frac{iqd}{2}} \tilde{C}_{1,q} \right) \\ \tilde{B}_{p<q} = \frac{g}{\omega-\omega_p-\omega_q} \sum\limits_{j=1}^{2} \left(e^{ipd\left(\frac{3}{2}-j\right)} \tilde{C}_{j,q} + e^{iqd\left(\frac{3}{2}-j\right)} \tilde{C}_{j,p} \right) \\ \tilde{B}_{q,q} = \frac{\sqrt{2}g}{\omega-2\omega_q} \sum\limits_{j=1}^{2} e^{iqd\left(\frac{3}{2}-j\right)} \tilde{C}_{j,q} \,, \end{cases} \tag{3.88}$$

and in which $\tilde{C}_{2,q}(\omega) = \tilde{C}^{*}_{1,q}(\omega)$ for $\omega \in \mathbb{R}$; while determining $\tilde{C}_{1,q}(\omega)$ interweaves positions and momenta, evading a simple treatment. However, it is possible to proceed by introducing the analytic function

$$C(\omega, z) := \sum_{j=-\infty}^{\infty} \tilde{C}_{1,j}(\omega) z^{1-j} \qquad (\text{with } z \in \mathbb{C}), \tag{3.89}$$

which simultaneously captures the position distribution of the amplitude $\tilde{C}_{1,j}(\omega)$ in its Laurent coefficients around $z = 0$, and the momentum distribution on the unit circle $z = e^{iqd} \in \mathbb{S}^1$,

$$C(\omega, e^{iqd}) = e^{-\frac{iqd}{2}} \tilde{C}_{1,q}(\omega). \tag{3.90}$$

After (anti-)symmetrizing this function,

$$C_\sigma(\omega, z) := \frac{1}{2} \left(C(\omega, z) + \frac{\sigma}{z} C\left(\omega, z^{-1}\right) \right), \tag{3.91}$$

the secular equation becomes

$$C_\sigma(\omega, z) = g \left(\frac{1}{z} + \sigma \right) \tilde{a}_\sigma(\delta\omega) \left(\frac{1/2 + g\tilde{C}_{1,2}(\omega)}{\omega - 2\Delta} + g \oint \frac{z' + \sigma}{1 + 2\delta\omega\, z' + z'^2} \frac{C_\sigma(\omega, z')\mathrm{d}z'}{2\pi i} \right), \tag{3.92}$$

where the contour integral is positively oriented around $\mathbb{S}^1$ and $\delta\omega := \omega + (z + z^{-1})/2$ is the dimensionless counterpart of the energy left in the state after losing one of the excitations to the waveguide, $\hbar(\omega - \omega_q)$. The reappearance of (3.65) establishes the connection between one and two excitations analytically. We clarify that $\tilde{C}_{1,2}$ refers to the transformed field amplitude of having one excitation in emitter 1 and another in the waveguide at the position of emitter 2; this term can be treated as a constant from the perspective of solving the integral equation, although it couples the symmetry sectors $\sigma = \pm 1$.

To the best of our knowledge, this complex integral equation has not been studied in the literature. In the next two subsections, we develop the analytical tools to solve it based on two intertwined concepts: symmetries and the analytic structure of the solution.

3.6.4 Explicit and hidden symmetries

An exact solution has escaped the community for 70 years after Dicke's seminal work on superradiance [18] because multiparticle problems that do not adhere to the Bethe ansatz[15] [167] are broadly regarded as lacking enough symmetry to be solvable[16]. However, in physics, it is common to model complex systems as simpler highly-symmetric objects: like when Earth is approximated as a sphere, or the universe as an isometric and homogeneous space-time metric. So why not use simpler functions to model solutions of equations that we cannot solve otherwise?

Normally, in physics such models are born from intuition and judged by their results; but we can establish this notion with mathematical rigor. Consider looking at a person for instance. Intuition might tell you that most of us are left-right symmetric, but a number of details such as the shape of your hair or the position of freckles break the symmetry. It is highly tempting to regard it as an approximate symmetry, but to quantify the differences between a person and his mirror image is just too hard. Mathematically, one would have to define a distance function between complex systems and apply it between the original system and the transformed one. Our approach bypasses this difficulty: we propose to use an equivalence relation "$\sim$" and group all "equivalent people" together. For instance, we could say that two people are equivalent if they have the same number of fingers on the right hand and also the same number of fingers on the left hand. Then the group of people (known as the "equivalence class" and denoted by "$[\bullet]$") that have 5 fingers on the right and 5 fingers on the left is perfectly left-right symmetric, even if the individual members are not. This is because the reflected image of any one person in this set is yet another person in the set.

One might think that this way of manipulating symmetries is too loose to find exact solutions, as a big deal of information on the original problem is lost when taking the equivalence class. But this is not the case –as we will see in our problem at hand– if the chosen equivalence relation allows us to trace the original element back.

Let us focus now on the symmetries of our system. These symmetries generate a group of transformations of the double complex plane $(\omega, z) \in \mathbb{C} \times \mathbb{C}$. We highlight the following 3 generators:

i. The inversion $(\omega, z) \to (\omega, z^{-1})$ physically represents left-right parity in the system.

ii. The reciprocation $(\omega, z) \to (-\omega, -z)$ finds its physical origin in the symmetry of the band structure $\omega_q = -\omega_{q+k_r}$. This symmetry becomes explicit in parameter space under the change $\Delta \to -\Delta$ (see FIG. 3.26) and is broken when multiple bands are considered [51]. It is the one responsible for the suppression of collective effects at $\Delta = 0$ (see Sec. 3.5.1.***iii*** or 3.6.2). Signatures of this symmetry in single-excitation, single-QE bound states coupled to a single band were observed in [91].

---

[15] While we won't explore the topic, it's worth noting that the Bethe ansatz is a significant area of research at SBU. Esteemed faculty members such as C. N. Yang [165] and V. E. Korepin [166] have made substantial contributions to this field.

[16] By "solvable" here we mean in a closed form involving a finite set of elementary functions

iii. The substitution $(\omega, z) \rightarrow (\omega, \zeta(\omega, z))$ is motivated by the exchange of function variable z with the contributing pole of the two canceling the denominator in (3.92)'s integrand,

$$\zeta^{\pm 1}(\omega, z) := -\delta\omega \pm \sqrt{\delta\omega + 1}\sqrt{\delta\omega - 1}, \tag{3.93}$$

where by 'contributing' we mean that it lies within the integration contour, $|\zeta(\omega, z)| \leq 1$. This inequality is generally strict except for $z \in \zeta^{\pm 1}\left(\omega, \mathbb{S}^1\right)$, at which the integration contour crosses a pole and the integral is not well defined. In this way, $\zeta^{\pm 1}\left(\omega, \mathbb{S}^1\right)$ defines two mutually-inverse branch cuts in the shape of curve segments connecting the branch points $\zeta^{\pm 1}(\omega, 1)$ and $\zeta^{\pm 1}(\omega, -1)$. These cuts are present not only in $C_\sigma(\omega, z)$ but also in $\tilde{a}_\sigma(\delta\omega)$.

The function ζ has many other mathematical properties, such as $\zeta(\omega, z) = \zeta(\omega, z^{-1})$, $\zeta(\omega, z) = -\zeta(-\omega, -z)$, or $\zeta(\omega, \zeta(\omega, z)) = z^{\pm 1}$ (for $|z|^{\pm 1} < 1$), that ensure the closure of the symmetry group. From the point of view of physics however, the substitution is a rather abstract symmetry: it leaves certain properties of $C_\sigma(z)$ invariant but not $C_\sigma(z)$ itself.

To be more specific, the symmetry is not explicit but hidden, which can be stated mathematically. In the following, we treat ω as an implicit constant and only show z-dependencies. Also for simplicity, we restrict the z-domain to $\mathbb{C} \setminus \left(\mathbb{S}^1 \cup \zeta\left(\mathbb{S}^1\right) \cup \zeta^{-1}\left(\mathbb{S}^1\right)\right)$. Let us denote by $\mathrm{sl}(z) := \operatorname{sign}\log|z|$ the sign of the logarithm of a number's absolute value, by

$$\mathcal{R} = \left\{ \frac{P(z)}{Q(z)} \middle| P, Q \in \mathbb{C}[z] \right\} \tag{3.94}$$

the set of rational complex functions, and by

$$\mathcal{A} = \mathcal{R}\left\langle 1, \zeta, \mathrm{sl}, \mathrm{sl}\,\zeta \right\rangle \tag{3.95}$$

an algebra (under the usual operations) of functions of the form

$$\alpha(z) = \begin{cases} r_1(z) + r_2(z)\frac{\sqrt{\delta\omega-1}}{\sqrt{\delta\omega+1}} & \text{if } |z| < 1 \\ r_3(z) + r_4(z)\frac{\sqrt{\delta\omega-1}}{\sqrt{\delta\omega+1}} & \text{if } |z| > 1 \end{cases} \tag{3.96}$$

where $r_1, r_2, r_3, r_4 \in \mathcal{R}$. This algebra is closed under the symmetry group discussed above. We note that the functions in $\mathcal{A}$ need to be defined by parts to accommodate for the symmetry $z \rightarrow \zeta(\zeta(z)) = z^{-1}(1 + \mathrm{sl}(z))/2 + z(1 - \mathrm{sl}(z))/2$.

Since functions in $\mathcal{A}$ have simple expressions that can be found *a posteriori*, we can 'set them aside' through an equivalence relation

$$f_1 \sim f_2 \Leftrightarrow \exists \alpha, \alpha^{-1} \in \mathcal{A} \mid f_1 - \alpha f_2 \in \mathcal{A}. \tag{3.97}$$

This relation greatly simplifies the problem. For instance, tweaking Eqn. (3.92) to simplify it while retaining the new solution $\Phi(z)$ in the same equivalence class, $[\Phi(z)] = [C_\sigma(z)]$.

There are many choices for this; we propose

$$\Phi(z) = \tfrac{z+1}{z-1}\left(\frac{1}{4} + \oint \tfrac{z'-1/z'}{1+2\delta\omega z'+z'^2}\frac{\sqrt{\delta\omega'+1}}{\sqrt{\delta\omega'-1}}\frac{\Phi(z')\mathrm{d}z'}{2\pi i}\right), \tag{3.98}$$

where $\delta\omega' := \omega + (z' + z'^{-1})/2$ and the integration takes place around a positively oriented circle of radius 1^- and center in 0.

We work out the properties of this equation in Appendix C with the main result being that the solution is equivalent to an incomplete Legendre's relation

$$C_\sigma(z) \sim \Phi(z) \sim K(k^{-1})E(x(z);k) - k^2E(k^{-1})F(x(z);k) - (1-k^2)K(k^{-1})F(x(z);k) \tag{3.99}$$

(see TAB. 3.2). With this, we choose Φ as a canonical representative for the solution, as it is more explicitly symmetric (see (C.1)) which translates in

$$[C_\sigma(z)] = [C_\sigma(\zeta(z))]. \tag{3.100}$$

This characterizes $z \to \zeta(z)$ not as a symmetry of $C_\sigma(z)$ in the space of functions, but in the quotient space of equivalence classes. Such a condition is a lot less restrictive on the requirements of invariance that symmetries should satisfy, and therefore it is expected that this method will apply to many other problems.

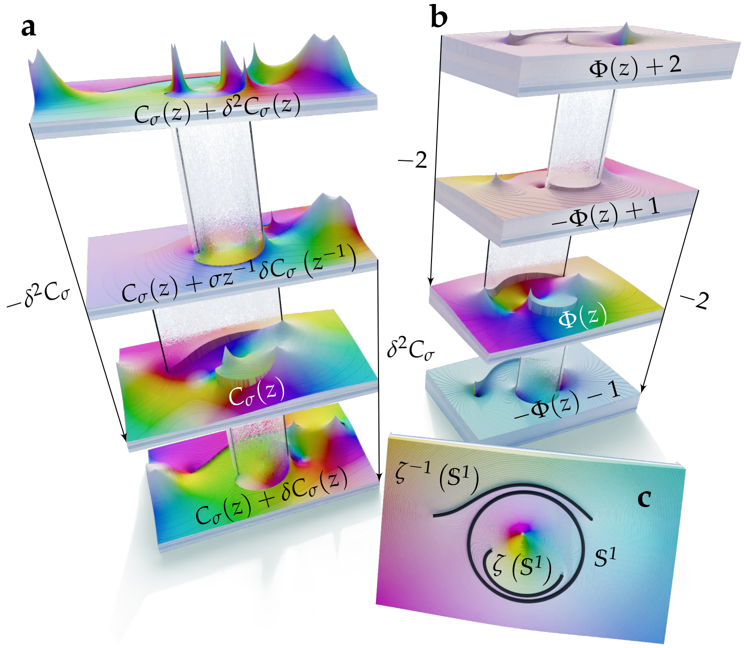

FIGURE 3.24: **Domain coloring plots** of functions $C_\sigma(z)$ (**a**) and $\Phi(z)$ (**b**), and $\zeta(z)$ (**c**). **a** and **b** extended analytically to an ∞ number of Riemann sheets (only 4 shown), connected through the branch cuts $\zeta^{\pm 1}(\mathbb{S}^1)$ that are represented vertically. These are also branch cuts of $\zeta(z)$, which are represented in **c** together with $\mathbb{S}^1$ as thick black lines. The plots have a complex frequency of $\omega = (1-i)\left(\sqrt{5}-2\right)/2$, parameters $\Delta = 0$ and $g = \sigma = 1$, and a plot range of $|\mathrm{Re}\, z| \leq (1+\sqrt{5})^2/4$ and $|\mathrm{Im}\, z| \leq (1+\sqrt{5})/2$. Figure reproduced from [70].

TABLE 3.2: Set of formulas for the evaluation of $C_\sigma(z)$ through (3.102). Table reproduced from [70].

<table>
<tr><td colspan="4">Increments of C_σ</td></tr>
<tr><td colspan="2">$\delta C_\sigma(z) = \frac{\left(2g\tilde{C}_{1,1}\sigma-1\right)\frac{z+\sigma}{z}\frac{\sqrt{\delta\omega-\sigma}}{\sqrt{\delta\omega+\sigma}}}{g^3\left(\left[g^{-2}(\delta\omega-\Delta)-\sigma\right]^2-\frac{\delta\omega-\sigma}{\delta\omega+\sigma}\right)\left(g^{-2}\left(\frac{z+1/z}{2}+\Delta\right)+\frac{2\sigma z}{z-\sigma}\right)}$</td><td colspan="2">$\delta^2 C_\sigma(z) = \frac{-2\sigma\left(2g\tilde{C}_{1,1}\sigma-1\right)\frac{\sqrt{\delta\omega-\sigma}}{\sqrt{\delta\omega+\sigma}}\frac{(z+\sigma)^2}{z(z-\sigma)}}{g^3\left(\left[g^{-2}(\delta\omega-\Delta)-\sigma\right]^2-\frac{\delta\omega-\sigma}{\delta\omega+\sigma}\right)\left(\left[g^{-2}\left(\frac{z+1/z}{2}+\Delta\right)+\sigma\right]^2-\frac{(z+\sigma)^2}{(z-\sigma)^2}\right)}$</td></tr>
<tr><td colspan="4">The Φ function</td></tr>
<tr><td colspan="4">$\Phi(z) = \frac{-K(k^{-1})\,\mathrm{sgnRe}\,\omega}{2\pi\sqrt{k}}\left(\frac{z^{-1}-z}{1-\zeta(z)}+\frac{z+1}{z-1}(1+\omega)+2\frac{z-1}{z+1}\zeta^{-1}(-1)-\frac{z^2-6z+1}{z^2-1}\zeta^{-1}(z)\right)$
$-\frac{2\,\mathrm{sgnRe}\,\omega}{\pi i k}\left(K(k^{-1})E(x;k)-k^2E(k^{-1})F(x;k)-(1-k^2)K(k^{-1})F(x;k)\right)$</td></tr>
<tr><td colspan="4">Elliptic integrals</td></tr>
<tr><td colspan="2">incomplete</td><td colspan="2">complete</td></tr>
<tr><td>1st kind</td><td>2nd kind</td><td>1st kind</td><td>2nd kind</td></tr>
<tr><td>$F(x;k) := \int_0^x \frac{\mathrm{d}t}{\sqrt{1-t^2}\sqrt{1-k^2t^2}}$</td><td>$E(x;k) := \int_0^x \frac{\sqrt{1-k^2t^2}}{\sqrt{1-t^2}}\,\mathrm{d}t$</td><td>$K(k) := F(1;k)$</td><td>$E(k) := E(1;k)$</td></tr>
<tr><td colspan="2">Eccentricity</td><td colspan="2">Amplitude</td></tr>
<tr><td colspan="2">$k = \frac{\omega^2-2+\omega\sqrt{\omega-2}\sqrt{\omega+2}}{2}$</td><td colspan="2">$x = \frac{k^{-1/2}\,\mathrm{sgnIm}\,\omega}{\sqrt{-k-\zeta^{-1}(-1)}}\frac{z+1}{z-1}\sqrt{\frac{\zeta^{-1}(z)-\zeta(1)}{\zeta^{-1}(z)-\zeta(-1)}}\sqrt{\frac{\zeta^{-1}(-1)-\zeta(-1)}{\zeta^{-1}(z)-\zeta(-1)}\frac{\zeta^{-1}(z)-\zeta^{-1}(1)}{\zeta^{-1}(-1)-\zeta^{-1}(1)}}$</td></tr>
<tr><td colspan="2">$\mathrm{sgnIm}\,\omega = \begin{cases} +1 \text{ if } \mathrm{Im}\omega > 0 \vee (\mathrm{Im}\,\omega = 0 \wedge \mathrm{Re}\,\omega < 2) \\ -1 \text{ otherwise} \end{cases}$</td><td colspan="2">$\mathrm{sgnRe}\,\omega = \begin{cases} +1 \text{ if } \mathrm{Re}\,\omega \geq 0 \\ -1 \text{ otherwise} \end{cases}$</td></tr>
<tr><td colspan="4">The rational function r_σ</td></tr>
<tr><td colspan="4">$r_\sigma(z) = \frac{\sigma}{4}\left(\delta C_\sigma(z)+\frac{\sigma}{z}\delta C_\sigma\left(\frac{1}{z}\right)\right)\frac{\sqrt{\delta\omega+\sigma}}{\sqrt{\delta\omega-\sigma}}\left[g^{-2}\left(\delta\omega-\Delta\right)-\sigma\right]$
$+\left(2g\tilde{C}_{1,1}\sigma-1\right)\sum_{i=1}^{3}\alpha_\sigma(z_{\sigma i})\left(\sigma+z^{-1}\right)z_{\sigma i}\left(\frac{1}{1+2\delta\omega\, z_{\sigma i}+z_{\sigma i}^2}-\frac{1}{(1-z_{\sigma i}z)(1-z_{\sigma i}z^{-1})}\right)$</td></tr>
<tr><td colspan="2">$(z_{\sigma i}^2+2\Delta z_{\sigma i}+1)(z_{\sigma i}-\sigma) = 4g^2 z_{\sigma i}$</td><td colspan="2">$\alpha_\sigma(z) := \frac{\left(2\sigma(2\Phi(z)+1)\frac{\sqrt{\delta\omega-\sigma}}{\sqrt{\delta\omega+\sigma}}-\left[g^{-2}(\delta\omega-\Delta)-\sigma\right]\right)\left(1-z^{-2}\right)}{2g^3\left(\left[g^{-2}(\delta\omega-\Delta)-\sigma\right]^2-\frac{\delta\omega-\sigma}{\delta\omega+\sigma}\right)\left(g^{-2}(1-z^{-2})+\frac{4}{(\sigma-z)^2}\right)}$</td></tr>
<tr><td colspan="4">Special field amplitudes</td></tr>
<tr><td colspan="2">$2g\tilde{C}_{1,1} = \frac{\sum_{\sigma,i}\sigma\alpha_\sigma(z_{\sigma i})}{\sum_{\sigma,i}\alpha_\sigma(z_{\sigma i})}$</td><td colspan="2">$2g\tilde{C}_{1,2} = \frac{\omega-2\Delta}{2g}\frac{\left(\sum_{\sigma,i}\sigma\alpha_\sigma(z_{\sigma i})\right)^2-\left(\sum_{\sigma,i}\alpha_\sigma(z_{\sigma i})\right)^2}{\sum_{\sigma,i}\alpha_\sigma(z_{\sigma i})} - 1$</td></tr>
</table>

3.6.5 Analytic structure

The analytic continuation of $C_\sigma(z)$ can be investigated by modifying the integration contour of (3.92) as z is displaced across the branch cuts (see App. B for details). Crossing $\zeta\ (\mathbb{S}^1)$ results in an increment $\delta C_\sigma(z)$ in the function, which is again lost if the same branch cut is subsequently crossed in the same direction. By inversion symmetry, the situation is analogous when crossing $\zeta^{-1}\ (\mathbb{S}^1)$, while the increment becomes $\sigma z^{-1}\delta C_\sigma(z^{-1})$.

The analytically continued function is strikingly similar to the original: whereas the simple poles of C_σ inherited by $\tilde{a}_\sigma$ in (3.92) relocate, the branch cuts (which are independent of g, Δ and σ, see (3.93)) reappear over and over in the same locations as illustrated in FIG. 3.24. Crossing one branch cut after the other leads to an increment of $\pm\delta^2 C_\sigma$, where

$$\delta^2 C_\sigma(z) := \delta C_\sigma(z) - \sigma z^{-1}\delta C_\sigma\left(z^{-1}\right). \tag{3.101}$$

This behavior can be written succinctly as

$$C_\sigma(z) = \frac{1}{2}\delta^2 C_\sigma(z)\left(\Phi(z)+\frac{1}{2}\right) - \frac{1}{2}\delta C_\sigma(z) + \frac{1}{2}r_\sigma(z), \tag{3.102}$$

where we interpret this as a deconstruction of the analytic structure of $C_\sigma(z)$: $\Phi(z)$ contains the monodromy group of the function (it has the same branch cuts, see FIG. 3.24**b**) but unlike C_σ it is independent of g, Δ, σ, $\tilde{C}_{1,1}$ or $\tilde{C}_{1,2}$; then $\delta^2 C_\sigma(z)$ and $\delta C_\sigma(z)$ are algebraic functions that fix double and single leaps (respectively) in the Riemann sheets of the function; and $r_\sigma(z)$ is a rational function that fixes the form of C_σ within one Riemann sheet. Closed formulas for these functions are given in TABLE 3.2 and proof of these can be found in Appendices B, C, and D.

3.6.6 Spectrum and decay

Combining the expression for $\tilde{A}$ in Eqn. (3.88) with expressions for $\tilde{C}_{1,2}$ (and nested definitions of $z_{\sigma i}$ and α_σ) in TAB. 3.2 yields

$$\tilde{A}(\omega) = \frac{\left(\sum_{\sigma,i} \sigma \alpha_\sigma(\omega, z_{\sigma i})\right)^2 - \left(\sum_{\sigma,i} \alpha_\sigma(\omega, z_{\sigma i})\right)^2}{2g \sum_{\sigma,i} \alpha_\sigma(\omega, z_{\sigma i})} \tag{3.103}$$

for the amplitude of both emitters being simultaneously excited, which we use to study the spectrum and decay properties of the system. While the spectrum is determined by the complex singularities of $\tilde{A}(\omega)$ (all located on the real line), the decay properties are given by the analytic continuation in the complex ω-plane [51]. More specifically, the branch cuts of $\tilde{A}(\omega)$ are segments along the real line representing different continua in the spectrum; redrawing them vertically reveals other singularities (as in FIG. 3.25**a**) that characterize the decay dynamics.

The spectrum of the system is easily understood physically. There are simple real poles that represent bound states with both excitations located around the emitters. These poles satisfy the equation

$$\sum_{\sigma,i} \alpha_\sigma(\omega, z_{\sigma i}) = 0, \tag{3.104}$$

and they can be located away from or on the branch cuts (in which case they represent bound states in the continuum and, consequently, they are hard to distinguish with simple numerical approaches, such as a brute-force diagonalization of the truncated Hamiltonian). The largest of these cuts is $[-2, 2]$ and it represents two excitations emitted into the waveguide. Additionally, a cut is formed at $[\varepsilon_{\sigma i} - 1, \varepsilon_{\sigma i} + 1]$ (for some $i \in \{1, 2, 3\}$) when one excitation forms a bound state of parity σ and dimensionless energy $\varepsilon_{\sigma i} = -\left(z_{\sigma i} + z_{\sigma i}^{-1}\right)/2$ (see Sec. 3.5.1) and another excitation is delocalized over the waveguide. We note that Eqn. (3.104) is exact, in contrast to previous approaches used to compute multiexcitation bound state energies, such as variational [50] or perturbative [47] methods.

To access the decay properties, one needs to analytically continue $\tilde{A}(\omega)$ beyond these branch cuts. For most of the calculations, this can be done by reverting the signs of the square roots appropriately. The situation is complicated by $\Phi(\omega, z)$ when ω crosses $[-2, 2]$ (see FIG. C.1): the two branch cuts in z-space, $\zeta^{\pm 1}\left(\omega, \mathbb{S}^1\right)$, come into contact when

$\omega \in [-2, 2]$ and, as they separate beyond this continuum, a new branch cut crosses from one to the other. This topological change in analytic structure is important for understanding the collective decay of our system.

The analysis reveals several sources of decay:

i. Solutions to the analytic continuation of (3.104) that do not describe bound states, contain the collective exponential decay rates. Mathematically, they are simple poles p in the continuation of $\tilde{A}(\omega)$ and, while their frequency is $\operatorname{Re} p$, the amplitude decay rates are given by $-\operatorname{Im} p$. In some cases, this decay rate might exceed the Markovian superradiant prediction $2\Gamma/2$ (for instance, for $\Delta = -0.8$ and $g = \Gamma = 0.3$ the dominant pole is $-1.5077(1) - 0.31956(1)i$). However, even in such cases and in contrast to [59, 62], the total decay is generally slower than the Markovian prediction (Sec. 3.6.2) due to other non-Markovian effects such as the bound population at late times, or the dynamics starting out as Rabi oscillations between the QEs and the sites below them at early times [91].

ii. When $\varepsilon_{\sigma i} \in \mathbb{C}$ is a pole that contributes to the decay dynamics of a single excitation (Sec. 3.5.1), then $\varepsilon_{\sigma i} \pm 1$ is a branch point of the two-excitation problem, with frequency $\operatorname{Re}\{\varepsilon_{\sigma i} \pm 1\}$ and a mixture of exponential decay with rate $-\operatorname{Im} \varepsilon_{\sigma i}$ (which can be 0) and an algebraic decay with an order inherited from the corresponding single-excitation band edge (generally 3/2).

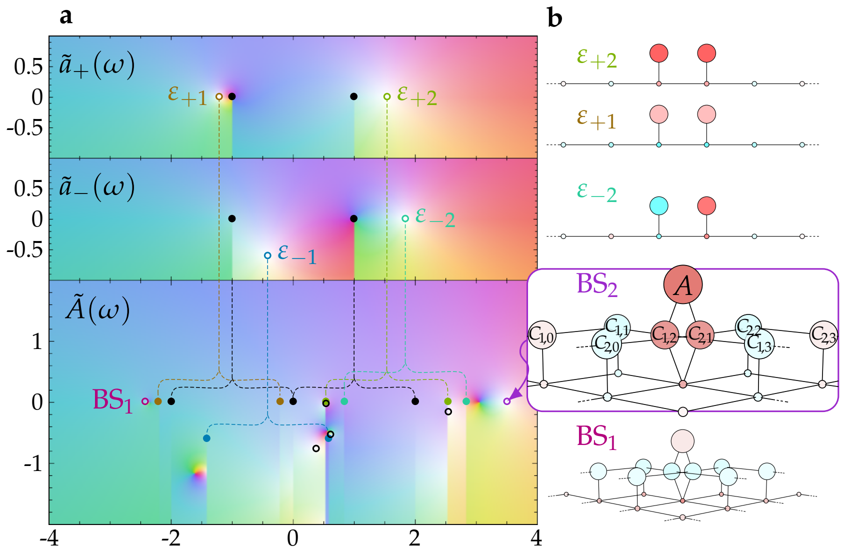

FIGURE 3.25: *Spectrum and decay properties* of the system for $\Delta = g = 1$. **a,** Simple poles (open circles) $\varepsilon_{\sigma i}$ of the transformed symmetric ($\sigma = +1$) and antisymmetric ($\sigma = -1$) emitter amplitudes $\tilde{a}_\sigma(\omega)$ split into branch points (solid circles) $\varepsilon_{\sigma i} \pm 1$ of the doubly-excited amplitude $\tilde{A}(\omega)$. Black open circles correspond to collective exponential decay sources. **b,** Corresponding bound-state amplitudes in Wannier space for a single excitation ($\varepsilon_{+1}, \varepsilon_{+2}$, and ε_{-1}) and two excitations (BS_1 and BS_2). Hue encodes the phase (red for positive, cyan for negative) and saturation encodes the absolute value. Figure reproduced from [70].

iii. In between branch points $\omega = \pm 2$ at the borders of $[-2, 2]$, there is an additional branch point at the center ($\omega = 0$). All three points are a source of algebraic decay, generally of order 3 (such as the expected for quantum emitters in 2D [134]). From a mathematical perspective, these singularities originate from $\Phi(\omega, z)$ and are thus the hardest to analyze (see the last part of App. C).

Indeed, ***ii*** and ***iii*** are what one would expect for two independently emitted excitations. However, the algebraic decay orders themselves can also present signs of collective decay. For instance, for $\Delta = 0$ and $g = 1$ (a critical coupling between Markovian decay and bound-state induced oscillations), one might expect $\omega = \pm(1 + \sqrt{2})$ to be the dominant decay sources at very late times ($2Jt \gg 10$) with an algebraic order of $1/2$. However, these sources actually have an order of $3/2$, making the branch points $\omega = \pm 2$ the slowest decay sources instead. Additionally, assuming independently emitted excitations would imply those sources produce algebraic decay of order 1, but there is a $\log^2(t)$ correction to the asymptotic decay that they induce,

$$\sim \frac{e^{\mp 2it}}{t \log^2(t)}. \tag{3.105}$$

We note that such a logarithmic correction will be difficult to access in measurements and simulations because the bound state contributions overshadow the algebraic decay at exponentially late times. For any other parameter values the logarithmic corrections are also present at $\omega = \pm 2$ and $\omega = 0$, although not generally at leading order.

Exponential, algebraic decay, and bound states always participate in the dynamics, but which one dominates the emission process depends on the interplay between g and Δ. Qualitatively, for weak couplings g (see FIG. 3.26), the decay is mostly Markovian for deep in-band detunings Δ, mostly algebraic when Δ is resonant with the band edges and suppressed for detunings far outside the band, when none of the two excitations may significantly leave its emitter (this means they form a two-excitation bound state of energy $\simeq 2\Delta$). As one increases the coupling, the Markovian decay for in-band detunings becomes algebraic with pronounced oscillations that eventually become bound-state oscillations [91] for couplings that surpass the band width. The dynamics is not sensitive to detuning changes smaller than the coupling.

A clear signature of non-Markovian collective behavior can be found in the probability of having one excitation in the emitters and the other in the waveguide (the right plot of FIG. 3.26). If we use p to denote the probability for the first excitation to be held by one of the emitters, then assuming independence between the two excitations would result in a probability $2p(1-p)$ of having just one emitter excited. Since $2p(1-p) \leq 1/2$ regardless of the value of p, 0.5 is a fundamental limitation for this probability, were the excitations independent. The collective nature of the decay allows it to break this limitation, as seen in the plot. As shown in Sec. 3.6.2, the violation is also a sign of non-Markovianity, because the Markovian prediction for this probability peaks at 0.5 for $\Delta = 0$ when the decay channels are not collectively enhanced or suppressed.

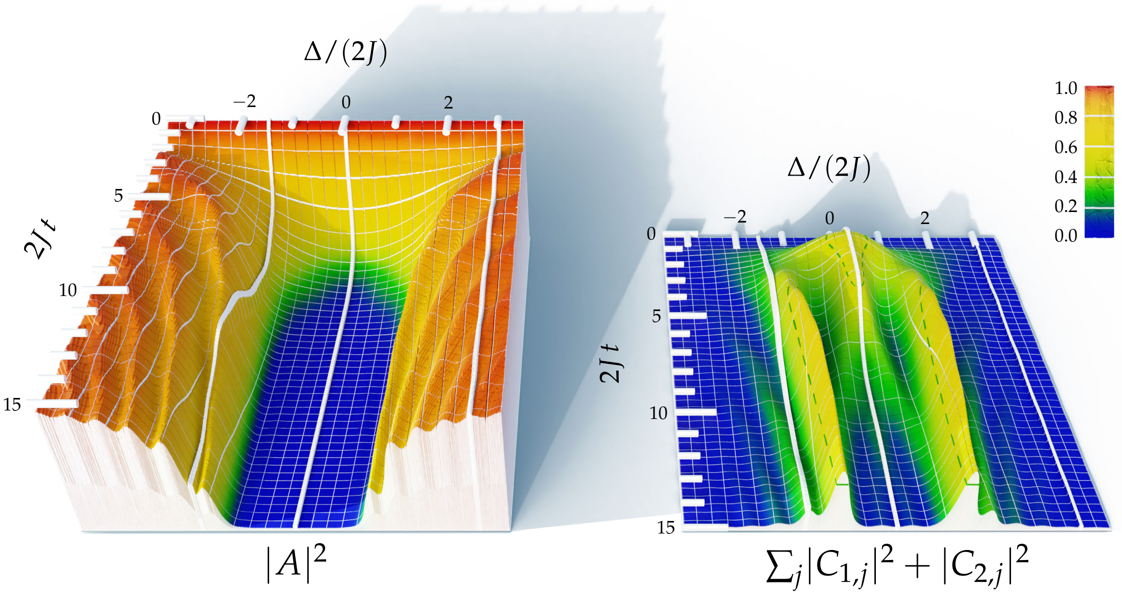

FIGURE 3.26: *Dynamical evolution* of the probability $|A(t)|^2$ of having both emitters simultaneously excited and the probability $\sum_{j=-\infty}^{\infty} |C_{1,j}(t)|^2 + |C_{2,j}(t)|^2$ of having only one excited for a coupling strength $g = 1/3$. Three white lines in each plot delineate examples of dynamics dominated by Markovian decay (at $\Delta = 0$), algebraic decay ($\Delta = -3J$), and a bound state ($\Delta = 6J$). The dashed lines on the right plot are level lines of probability 0.5, the theoretical maximum if the excitations were independent. Figure reproduced from [70].

3.6.7 Bound states with two excitations

The shape of two-excitation bound states can most easily be computed by reusing the equations that describe the transformed field amplitudes in Sections 3.6.3 and 3.6.5. These equations (except those for $\tilde{C}_{1,1}$ and $\tilde{C}_{1,2}$ in TABLE 3.2) are affine, with a homogeneous part proportional to the field amplitudes and an inhomogeneous part. Removing the tildes and the inhomogeneous parts (e.g. through the substitutions $(2g\tilde{C}_{1,1}\sigma - 1) \to 2gC_{1,1}\sigma$ in TABLE 3.2) yields equations that describe the field amplitudes of the bound states instead.

There are two ways to justify dropping the tildes and the inhomogeneous part to compute the bound states. First, the eigenstate equation is formally identical to the TSE (A.1), except for the tildes and a "-1" that represents the initial conditions and breaks the linearity of the equations. Second, the transformed field amplitudes are divergent at the bound state energies, so the inhomogeneous terms are negligible in comparison. Scaling the amplitudes A (from Eqn. (3.103)), $C_{1,1}$ and $C_{1,2}$ (from TABLE 3.2) with the vanishing factor $\sum_{\sigma,i} \alpha_\sigma(z_{\sigma i})$ fixes the divergent terms and yields the correct (not yet normalized) multi-excitation bound-state amplitudes. This argument can be made more rigorous by using the residue theorem in the IT and separating the bound states using a harmonic decomposition of the solution. Examples of bound states are presented in FIG. 3.25**b**.

3.6.8 Closing remarks

This completes the picture for the problem of two excited QEs coupled to a single-band waveguide, which constitutes a minimal scenario for the study of collective non-Markovian decay. The solution could be generalized to many other cases whose exact single-excitation dynamics are known [45, 49–52, 55–57, 121, 135, 157, 168, 169]. The most immediate generalizations are to revisit the multi-photon scattering problem [64, 67, 69, 170] by means of a different initial state; to change the distance between the emitters and investigate delay-induced entangled dark states [61]; or to consider multiband waveguides, which – as shown in Sec. 3.4.1–can also be done analytically and efficiently by using infinite products *à la Euler* [51].

Non-Markovian collective decay is commonly related to either strong coupling or retardation delays between emitters [171]. This characterization oversimplifies the full complexity of the problem, which has infinitely many degrees of freedom. We instead treat the quantum emitters and the radiation modes as a collective in which every constituent partakes in the decay process since the spectral decay components of the solution cannot be traced back to individual origins.

The closed expression for the transformed field amplitudes in terms of elementary functions exposes a spectrum with a wide variety of decay types. Whereas the amount, frequencies, or decay rates of bound and exponentially-decaying states are independent of the single excitation spectrum, this is not the case for the algebraic decay components. The algebraic decay is generally caused by edges of continua involving free states, where the two excitations can be considered to be independent. A peculiar case of algebraic decay occurs at the center of the band, which is not singular for one excitation and does not lead to collective decay in the Markovian limit, and yet it is a source of collective non-Markovian decay with logarithmic modifications. These modifications might be the result of interference between superposed algebraic decays, as they also affect the edges of the continuum representing two free particles.

Despite their stark difference in functional dependence, logarithmic modifications to the decay would be extremely hard to measure, as they would require interrogating the emitters for exponentially long times with exponentially high precision. In contrast, finding more than a 50% chance of having exactly one emitter excited should be feasible in state-of-the-art experiments while also being a conceptually clearer indicator of collective non-Markovian decay. Our results could be tested in a variety of platforms, including atoms near photonic crystals [76] or optical fibers [86], semiconductor quantum dots [172], matter-wave emitters [78], quantum acoustic systems [173], or superconducting circuits [79].

We expect that the connections we established between the one- and two-excitation sectors can be extrapolated to arbitrary excitation numbers and that the solution presented here can also be used for studies of the fundamental connection between superradiance, synchronization [174, 175], and entanglement [66, 176, 177].

Chapter 4

Conclusion

The reader who has made it until this point of the dissertation is hopefully convinced that the work in our group makes for a rare combination in which theoretical physics, experimental physics, and pure mathematics –in the form of wQED, ultracold atoms, and complex analysis– are simultaneously advanced altogether. Waveguide QED has the difficulty of relying on assumptions, simplifications, and numerical techniques that often need external verification. Experiments with ultracold atoms are challenging to perform due to the technical demands of running complicated apparatus, as well as the necessity of devising, understanding, and contextualizing the experiments being done. Complex analysis is an extremely elegant and useful formalism but it needs new problems to feed on, and it can sometimes be hard to link it with reality or its practical uses. My research experience during my PhD is that the fields can complement each other while iterating theory and experiment until both converge into reliable results and measurements. The peculiar synergy between these three fields (illustrated in FIG. 4.1) has allowed our group

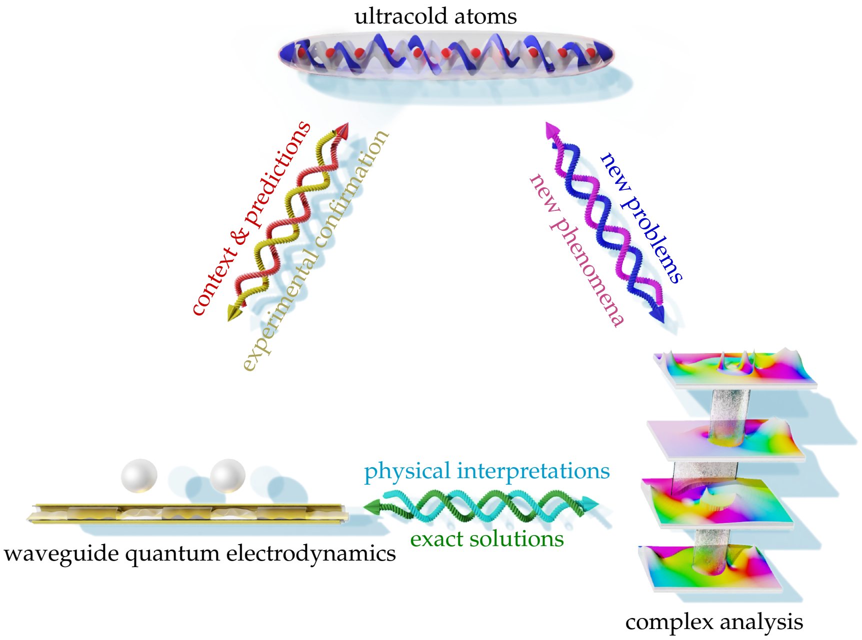

FIGURE 4.1: *Synergy* across fields in theoretical physics, experimental physics, and pure mathematics.

to develop a slow but steady and exhaustive understanding of light-matter interactions at the fundamental level.

From the experimental perspective, we have realized bound states below [78, 91] and above [91] the band, being the first group to image these states. We have transitioned between Markovian decay and coherent oscillations between BSs [91] far ahead of any other groups [125, 128]. We have predicted [51] and observed [118] a new quasiparticle, the matter-wave polariton. And more recently [92], we have made advanced use of coherence to create slow, non-Markovian super- and subradiant states; found indirect evidence of bound states in the continuum; created complex beats between multiple quantum emitters precluding dynamics akin those of a molecule of light; produced timed Dicke states, with some of them featuring strong directional emission akin to a quantum Archimedes screw; and also explored the reciprocal phenomenon of how collective decay can inducing coherence between the emitters.

Future lab improvements could enrich the matter-wave platform by the addition of state-selective optical potentials or tweezers for finer control of the number of quantum emitters [134] or the use of the state-selective light also for the creation of the lattice tubes, which would allow more independent control of the interaction strength between atomic species [92]. These could facilitate the observation of frustration [51], Floquet engineering of giant atoms [134], emission into topological waveguides [52, 178], topological polaritons [118, 179], simulations of fermionic quantum optics [139], or scattering experiments [180].

On the more theoretical side of wQED, the author has also made several contributions. Some small contributions amount to clarifying the connection between atom-photon bound states and polariton Wannier functions [78, 118], investigating the detailed spatial structure of bound states [51], or realizing that the origins of non-Markovian decay cannot, in general, be traced back to retardation or strong coupling alone [70]. Other contributions are the prediction of new phenomena, such as *ultra-Markovian* decay[1] next to an odd band edge [51], the possibility of double hopping in frustrated matter-wave polariton bands [51], or logarithmic modifications to a non-Markovian decay that is more than just exponential or algebraic [70]. Furthermore, the author was able to visualize the geometry of a collective non-Markovian system using adjacency graphs [70] shedding light on this arduous problem. More broadly, these contributions consist of simplifying, generalizing, and providing exact solutions for the analysis of the effects that strong coupling, emitter size, multiple bands, emitter arrangement, or multiple excitations have in spontaneous emission processes.

Interestingly, when multiple sizable quantum emitters decay, there are an infinite number of states decaying at increasing rates (see Sec. 3.5.3). A promising research avenue would be to study methods to isolate these states as they have, in principle, no bounds to how fast they can decay. Another direction that interests the author is to study further the connection between adjacency graphs of Hamiltonians, the emergence of space and relativity in quantum mechanics, and the asymptotic independence between particles [70].

---

[1] Meaning decay that is strongly Markovian despite belonging to a non-Markovian parameter regime.

In regards to complex analysis, the author has developed tools to solve several equations using holomorphic functions on $\mathbb{C}$. Remarkably, the treatment of Mathieu-like equations using infinite products *à la Euler* [51] offers a fastly-convergent and easy-to-analytically-continue description of the solution. Moreover, by generalizing the concept of symmetry we were able to unveil hidden symmetries that were not explicit in complex integrodifferential equations, also resulting in a novel solution.

In 1929, English mathematician and theoretical physicist Paul M. A. Dirac wrote: "*The fundamental laws necessary for the mathematical treatment of a large part of physics and the whole of chemistry are known... The difficulty lies only in the fact that these laws lead to equations too complex to be solved*" [181]. Our approach to hidden symmetries may be useful in the future development of theoretical physics, as it allows us to work with simpler versions of the equations without loss of information. Apart from yielding exact solutions to problems that are too hard or too asymmetric to solve otherwise, this could also help in the technical aspects of writing a paper, where often long equations have to be brought to a shorter form.

Bibliography

[1] J. Hadamard, *An essay on the psychology of invention in the mathematical field* (Dover Publications, 1954).

[2] R. Rashed, “Fermat et le principe du moindre temps”, Comptes Rendus Mécanique **347**, 357–364 (2019).

[3] M. S. Zubairy, “A very brief history of light”, in *Optics in our time*, edited by M. D. Al-Amri, M. El-Gomati, and M. S. Zubairy (Springer International Publishing, Cham, 2016), pp. 3–24.

[4] M. Planck, “On the theory of the energy distribution law of the normal spectrum”, Verhandl. Dtsch. phys. Ges. **2**, 237–245 (1900).

[5] A. Einstein, “Über einen die Erzeugung und Verwandlung des Lichtes betreffenden heuristischen Gesichtspunkt”, Annalen der Physik **322**, 132–148 (1905).

[6] G. N. Lewis, “The conservation of photons”, Nature **118**, 874–875 (1926).

[7] W. E. Lamb, “Anti-photon”, Applied Physics B **60**, 77–84 (1995).

[8] P. A. M. Dirac, “The quantum theory of the emission and absorption of radiation”, Proceedings of the Royal Society of London **114**, 243–265 (1927).

[9] V. Weisskopf and E. Wigner, “Berechnung der natürlichen linienbreite auf grund der diracschen lichttheorie”, Zeitschrift für Physik **63**, 54–73 (1930).

[10] A. Einstein, B. Podolsky, and N. Rosen, “Can quantum-mechanical description of physical reality be considered complete?”, Phys. Rev. **47**, 777–780 (1935).

[11] D. W. Belousek, “Einstein’s 1927 unpublished hidden-variable theory: its background, context and significance”, Stud. Hist. Philos. Sci. B **27**, 437–461 (1996).

[12] J. S. Bell, *Speakable and unspeakable in quantum mechanics: collected papers on quantum philosophy*, 2nd ed. (Cambridge University Press, Cambridge, 2004).

[13] J. F. Clauser, M. A. Horne, A. Shimony, and R. A. Holt, “Proposed experiment to test local hidden-variable theories”, Phys. Rev. Lett. **23**, 880–884 (1969).

[14] S. J. Freedman and J. F. Clauser, “Experimental test of local hidden-variable theories”, Phys. Rev. Lett. **28**, 938–941 (1972).

[15] C.-Y. Lu, X.-Q. Zhou, O. Gühne, W.-B. Gao, J. Zhang, Z.-S. Yuan, A. Goebel, T. Yang, and J.-W. Pan, “Experimental entanglement of six photons in graph states”, Nature Physics **3**, 91–95 (2007).

[16] H.-S. Zhong, H. Wang, Y.-H. Deng, M.-C. Chen, L.-C. Peng, Y.-H. Luo, J. Qin, D. Wu, X. Ding, Y. Hu, P. Hu, X.-Y. Yang, W.-J. Zhang, H. Li, Y. Li, X. Jiang, L. Gan, G. Yang, L. You, Z. Wang, L. Li, N.-L. Liu, C.-Y. Lu, and J.-W. Pan, "Quantum computational advantage using photons", Science **370**, 1460–1463 (2020).

[17] E. M. Purcell, "Spontaneous emission probabilities at ratio frequencies", Phys. Rev. **69**, 674–674 (1946).

[18] R. H. Dicke, "Coherence in spontaneous radiation processes", Physical Review **93**, 99–110 (1954).

[19] S. K. Lamoreaux, "The Casimir force: background, experiments, and applications", Reports on Progress in Physics **68**, 201 (2005).

[20] H. Walther, B. T. Varcoe, B.-G. Englert, and T. Becker, "Cavity quantum electrodynamics", Reports on Progress in Physics **69**, 1325 (2006).

[21] S. Haroche and J.-M. Raimond, "Cavity quantum electrodynamics", Scientific American **268**, 54–60 (1993).

[22] H. J. Kimble, "Strong interactions of single atoms and photons in cavity QED", Physica Scripta **1998**, 127 (1998).

[23] D. Leibfried, R. Blatt, C. Monroe, and D. Wineland, "Quantum dynamics of single trapped ions", Rev. Mod. Phys. **75**, 281–324 (2003).

[24] R. H. Brown and R. Q. Twiss, "Correlation between photons in two coherent beams of light", Nature **177**, 27–29 (1956).

[25] L. Mandel, "Fluctuations of photon beams and their correlations", Proceedings of the Physical Society **72**, 1037 (1958).

[26] R. J. Glauber, "The quantum theory of optical coherence", Phys. Rev. **130**, 2529–2539 (1963).

[27] L. Mandel and E. Wolf, *Optical coherence and quantum optics* (Cambridge University Press, Cambridge, 1995).

[28] J. P. Gordon, H. J. Zeiger, and C. H. Townes, "The maser—new type of microwave amplifier, frequency standard, and spectrometer", Phys. Rev. **99**, 1264–1274 (1955).

[29] A. L. Schawlow and C. H. Townes, "Infrared and optical masers", Phys. Rev. **112**, 1940–1949 (1958).

[30] J. Heber, "All together now", Nature Materials **9**, S11–S11 (2010).

[31] C. V. Raman and K. S. Krishnan, "The negative absorption of radiation", Nature **122**, 12–13 (1928).

[32] B. P. Abbott et al., "Observation of gravitational waves from a binary black hole merger", Phys. Rev. Lett. **116**, 061102 (2016).

[33] T. Taylor, *Introduction to laser science and engineering* (CRC Press, 2019).

[34] D. Barredo, V. Lienhard, S. de Léséleuc, T. Lahaye, and A. Browaeys, "Synthetic three-dimensional atomic structures assembled atom by atom", Nature **561**, 79–82 (2018).

[35]W. Kaiser and C. G. B. Garrett, “Two-photon excitation in CaF_2: Eu^{2+}”, Phys. Rev. Lett. **7**, 229–231 (1961).

[36]P. A. Franken, A. E. Hill, C. W. Peters, and G. Weinreich, “Generation of optical harmonics”, Phys. Rev. Lett. **7**, 118–119 (1961).

[37]V. P. Bykov, “Spontaneous emission from a medium with a band spectrum”, Soviet Journal of Quantum Electronics **4**, 861 (1975).

[38]S. John, “Electromagnetic absorption in a disordered medium near a photon mobility edge”, Phys. Rev. Lett. **53**, 2169–2172 (1984).

[39]S. John, “Strong localization of photons in certain disordered dielectric superlattices”, Physical Review Letters **58**, 2486–2489 (1987).

[40]S. John and J. Wang, “Quantum electrodynamics near a photonic band gap: photon bound states and dressed atoms”, Physical Review Letters **64**, 2418–2421 (1990).

[41]S. John and J. Wang, “Quantum optics of localized light in a photonic band gap”, Phys. Rev. B **43**, 12772–12789 (1991).

[42]S. John and T. Quang, “Spontaneous emission near the edge of a photonic band gap”, Phys. Rev. A **50**, 1764–1769 (1994).

[43]S. John and T. Quang, “Localization of superradiance near a photonic band gap”, Phys. Rev. Lett. **74**, 3419–3422 (1995).

[44]L. Zhang, R. Gogna, W. Burg, E. Tutuc, and H. Deng, “Photonic-crystal exciton-polaritons in monolayer semiconductors”, Nature Communications **9**, 713 (2018).

[45]P Lambropoulos, G. M. Nikolopoulos, T. R. Nielsen, and S. Bay, “Fundamental quantum optics in structured reservoirs”, Reports on Progress in Physics **63**, 455 (2000).

[46]D. Mogilevtsev, “Robustness of the photon atom bound state in bandgap reservoirs”, J. Opt. B **7**, 274–282 (2005).

[47]T Shi, Y.-H. Wu, A González-Tudela, and J. I. Cirac, “Effective many-body Hamiltonians of qubit-photon bound states”, New Journal of Physics **20**, 105005 (2018).

[48]I. García-Elcano, A. González-Tudela, and J. Bravo-Abad, “Tunable and robust long-range coherent interactions between quantum emitters mediated by weyl bound states”, Phys. Rev. Lett. **125**, 163602 (2020).

[49]A. González-Tudela and J. I. Cirac, “Markovian and non-Markovian dynamics of quantum emitters coupled to two-dimensional structured reservoirs”, Physical Review A **96**, 043811 (2017).

[50]G. Calajó, F. Ciccarello, D. Chang, and P. Rabl, “Atom-field dressed states in slow-light waveguide QED”, Phys. Rev. A **93**, 033833 (2016).

[51]A. Lanuza, J. Kwon, Y. Kim, and D. Schneble, “Multiband and array effects in matter-wave-based waveguide QED”, Physical Review A **105**, 023703 (2022).

[52]M. Bello, G. Platero, J. I. Cirac, and A. González-Tudela, “Unconventional quantum optics in topological waveguide QED”, Science Advances **5**, eaaw0297 (2019).

[53] L. Z. Guo, A. Grimsmo, A. F. Kockum, M. Pletyukhov, and G. Johansson, “Giant acoustic atom: a single quantum system with a deterministic time delay”, Physical Review A **95**, 053821 (2017).

[54] L. Z. Guo, A. F. Kockum, F. Marquardt, and G. Johansson, “Oscillating bound states for a giant atom”, Physical Review Research **2**, 043014 (2020).

[55] A. Soro, C. S. Muñoz, and A. F. Kockum, “Interaction between giant atoms in a one-dimensional structured environment”, Physical Review A **107**, 013710 (2023).

[56] P. Facchi, D. Lonigro, S. Pascazio, F. V. Pepe, and D. Pomarico, “Bound states in the continuum for an array of quantum emitters”, Physical Review A **100**, 023834 (2019).

[57] A. Burgess and M. Florescu, “Non-Markovian dynamics of a single excitation within many-body dissipative systems”, Physical Review A **105**, 062207 (2022).

[58] G. Calajó, Y. L. Fang, H. U. Baranger, and F. Ciccarello, “Exciting a bound state in the continuum through multiphoton scattering plus delayed quantum feedback”, Physical Review Letters **122**, 073601 (2019).

[59] K. Sinha, P. Meystre, E. A. Goldschmidt, F. K. Fatemi, S. L. Rolston, and P. Solano, “Non-Markovian collective emission from macroscopically separated emitters”, Physical Review Letters **124**, 043603 (2020).

[60] A. Del Ángel, P. Solano, and P. Barberis-Blostein, “Effects of environment correlations on the onset of collective decay in waveguide QED”, Physical Review A **108**, 013703 (2023).

[61] W. Alvarez-Giron, P. Solano, K. Sinha, and P. Barberis-Blostein, “Delay-induced spontaneous dark state generation from two distant excited atoms”, arXiv:2303.06559, [quant–ph] (2023).

[62] F. Dinc and A. M. Brańczyk, “Non-Markovian super-superradiance in a linear chain of up to 100 qubits”, Physical Review Research **1**, 032042(R) (2019).

[63] H. Zheng and H. U. Baranger, “Persistent quantum beats and long-distance entanglement from waveguide-mediated interactions”, Physical Review Letters **110**, 113601 (2013).

[64] T. Shi, D. E. Chang, and J. I. Cirac, “Multiphoton-scattering theory and generalized master equations”, Physical Review A **92**, 053834 (2015).

[65] C. A. González-Gutiérrez, J. Román-Roche, and D. Zueco, “Distant emitters in ultrastrong waveguide QED: Ground-state properties and non-Markovian dynamics”, Physical Review A **104**, 053701 (2021).

[66] C. Cascio, J. C. Halimeh, I. P. McCulloch, A. Recati, and I. de Vega, “Dynamics of multiple atoms in one-dimensional fields”, Physical Review A **99**, 013845 (2019).

[67] M. Laakso and M. Pletyukhov, “Scattering of two photons from two distant qubits: exact solution”, Physical Review Letters **113**, 183601 (2014).

[68] M. P. Schneider, T. Sproll, C. Stawiarski, P. Schmitteckert, and K. Busch, “Green’s-function formalism for waveguide QED applications”, Physical Review A **93**, 013828 (2016).

[69] A. Roulet and V. Scarani, “Solving the scattering of N photons on a two-level atom without computation”, New Journal of Physics **18**, 093035 (2016).

[70] A. Lanuza and D. Schneble, “Exact solution for the collective non-Markovian decay of two fully excited quantum emitters”, arXiv:2403.13871, [quant–ph] (2024, accepted for publication in Phys. Rev. Research).

[71] A. S. Sheremet, M. I. Petrov, I. V. Iorsh, A. V. Poshakinskiy, and A. N. Poddubny, “Waveguide quantum electrodynamics: collective radiance and photon-photon correlations”, Reviews of Modern Physics **95**, 015002 (2023).

[72] M. Mirhosseini, E. Kim, X. Zhang, A. Sipahigil, P. B. Dieterle, A. J. Keller, A. Asenjo-Garcia, D. E. Chang, and O. Painter, “Cavity quantum electrodynamics with atom-like mirrors”, Nature **569**, 692–697 (2019).

[73] A. P. Foster, D. Hallett, I. V. Iorsh, S. J. Sheldon, M. R. Godsland, B. Royall, E. Clarke, I. A. Shelykh, A. M. Fox, M. S. Skolnick, I. E. Itskevich, and L. R. Wilson, “Tunable photon statistics exploiting the Fano effect in a waveguide”, Physical Review Letters **122**, 173603 (2019).

[74] A. Sipahigil, R. E. Evans, D. D. Sukachev, M. J. Burek, J. Borregaard, M. K. Bhaskar, C. T. Nguyen, J. L. Pacheco, H. A. Atikian, C. Meuwly, R. M. Camacho, F. Jelezko, E. Bielejec, H. Park, M. Lončar, and M. D. Lukin, “An integrated diamond nanophotonics platform for quantum-optical networks”, Science **354**, 847–850 (2016).

[75] N. V. Corzo, J. Raskop, A. Chandra, A. S. Sheremet, B. Gouraud, and J. Laurat, “Waveguide-coupled single collective excitation of atomic arrays”, Nature **566**, 359–362 (2019).

[76] A. Goban, C.-L. Hung, J. D. Hood, S.-P. Yu, J. A. Muniz, O. Painter, and H. J. Kimble, “Superradiance for atoms trapped along a photonic crystal waveguide”, Physical Review Letters **115**, 063601 (2015).

[77] B. Kannan, M. J. Ruckriegel, D. L. Campbell, A. F. Kockum, J. Braumuller, D. K. Kim, M. Kjaergaard, P. Krantz, A. Melville, B. M. Niedzielski, A. Vepsalainen, R. Winik, J. L. Yoder, F. Nori, T. P. Orlando, S. Gustavsson, and W. D. Oliver, “Waveguide quantum electrodynamics with superconducting artificial giant atoms”, Nature **583**, 775–779 (2020).

[78] L. Krinner, M. Stewart, A. Pazmiño, J. Kwon, and D. Schneble, “Spontaneous emission of matter waves from a tunable open quantum system”, Nature **559**, 589–592 (2018).

[79] X. Gu, A. F. Kockum, A. Miranowicz, Y. X. Liu, and F. Nori, “Microwave photonics with superconducting quantum circuits”, Physics Reports **718**, 1–102 (2017).

[80] M. Lucas, A. V. Danilov, L. V. Levitin, A. Jayaraman, A. J. Casey, L. Faoro, A. Y. Tzalenchuk, S. E. Kubatkin, J. Saunders, and S. E. de Graaf, “Quantum bath suppression in a superconducting circuit by immersion cooling”, Nature Communications **14**, 3522 (2023).

[81] M. V. Gustafsson, T. Aref, A. F. Kockum, M. K. Ekström, G. Johansson, and P. Delsing, “Propagating phonons coupled to an artificial atom”, Science **346**, 207–211 (2014).

[82] H. Thyrrestrup, G. Kiršanskė, H. Le Jeannic, T. Pregnolato, L. Zhai, L. Raahauge, L. Midolo, N. Rotenberg, A. Javadi, R. Schott, A. D. Wieck, A. Ludwig, M. C. Löbl, I. Söllner, R. J. Warburton, and P. Lodahl, "Quantum optics with near-lifetime-limited quantum-dot transitions in a nanophotonic waveguide", Nano Letters **18**, 1801–1806 (2018).

[83] H. Le Jeannic, T. Ramos, S. F. Simonsen, T. Pregnolato, Z. Liu, R. Schott, A. D. Wieck, A. Ludwig, N. Rotenberg, J. J. García-Ripoll, and P. Lodahl, "Experimental reconstruction of the few-photon nonlinear scattering matrix from a single quantum dot in a nanophotonic waveguide", Physical Review Letters **126**, 023603 (2021).

[84] M. K. Bhaskar, D. D. Sukachev, A. Sipahigil, R. E. Evans, M. J. Burek, C. T. Nguyen, L. J. Rogers, P. Siyushev, M. H. Metsch, H. Park, F. Jelezko, M. Lončar, and M. D. Lukin, "Quantum nonlinear optics with a germanium-vacancy color center in a nanoscale diamond waveguide", Physical Review Letters **118**, 223603 (2017).

[85] E. Vetsch, D. Reitz, G. Sagué, R. Schmidt, S. T. Dawkins, and A. Rauschenbeutel, "Optical interface created by laser-cooled atoms trapped in the evanescent field surrounding an optical nanofiber", Physical Review Letters **104**, 203603 (2010).

[86] C. Liedl, S. Pucher, F. Tebbenjohanns, P. Schneeweiss, and A. Rauschenbeutel, "Collective radiation of a cascaded quantum system: from timed Dicke states to inverted ensembles", Physical Review Letters **130**, 163602 (2023).

[87] C. Liedl, F. Tebbenjohanns, C. Bach, S. Pucher, A. Rauschenbeutel, and P. Schneeweiss, "Observation of superradiant bursts in a cascaded quantum system", Physical Review X **14**, 011020 (2024).

[88] I. de Vega, D. Porras, and J. Ignacio Cirac, "Matter-wave emission in optical lattices: single particle and collective effects", Phys. Rev. Lett. **101**, 260404 (2008).

[89] C. Navarrete-Benlloch, I. de Vega, D. Porras, and J. I. Cirac, "Simulating quantum-optical phenomena with cold atoms in optical lattices", New Journal of Physics **13**, 023024 (2011).

[90] M. Stewart, L. Krinner, A. Pazmiño, and D. Schneble, "Analysis of non-Markovian coupling of a lattice-trapped atom to free space", Physical Review A **95**, 013626 (2017).

[91] M. Stewart, J. Kwon, A. Lanuza, and D. Schneble, "Dynamics of matter-wave quantum emitters in a structured vacuum", Physical Review Research **2**, 043307 (2020).

[92] Y. Kim, A. Lanuza, and D. Schneble, "Super- and subradiant dynamics of quantum emitters mediated by atomic matter waves", arXiv:2311.09474, [quant–ph] (2023).

[93] E. MacKinnon, "De Broglie's thesis: A critical retrospective", American Journal of Physics **44**, 1047–1055 (1976).

[94] G. P. Thomson and A. Reid, "Diffraction of cathode rays by a thin film", Nature **119**, 890–890 (1927).

[95] C. Davisson and L. H. Germer, "Diffraction of electrons by a crystal of nickel", Phys. Rev. **30**, 705–740 (1927).

[96] A. Einstein, "Quantentheorie des einatomigen idealen Gases", Sitzungsberichte der Königlich Preussischen Akademie der Wissenschaften (1924).

[97] H. Metcalf and P. Van der Straten, *Laser cooling and trapping* (Springer, 1999).

[98] M. H. Anderson, J. R. Ensher, M. R. Matthews, C. E. Wieman, and E. A. Cornell, "Observation of Bose-Einstein condensation in a dilute atomic vapor", Science **269**, 198–201 (1995).

[99] K. B. Davis, M. O. Mewes, M. R. Andrews, N. J. van Druten, D. S. Durfee, D. M. Kurn, and W. Ketterle, "Bose-einstein condensation in a gas of sodium atoms", Physical Review Letters **75**, 3969–3973 (1995).

[100] N. Bigagli, W. Yuan, S. Zhang, B. Bulatovic, T. Karman, I. Stevenson, and S. Will, "Observation of Bose–Einstein condensation of dipolar molecules", Nature **631**, 289–293 (2024).

[101] M. Horvath, S. Dhar, A. Das, M. D. Frye, Y. Guo, J. M. Hutson, M. Landini, and H.-C. Nägerl, "Bose-Einstein condensation of non-ground-state caesium atoms", Nature Communications **15**, 3739 (2024).

[102] C.-C. Chen, R. González Escudero, J. Minář, B. Pasquiou, S. Bennetts, and F. Schreck, "Continuous Bose–Einstein condensation", Nature **606**, 683–687 (2022).

[103] E. R. Elliott, D. C. Aveline, N. P. Bigelow, P. Boegel, S. Botsi, E. Charron, J. P. D'Incao, P. Engels, T. Estrampes, N. Gaaloul, J. R. Kellogg, J. M. Kohel, N. E. Lay, N. Lundblad, M. Meister, M. E. Mossman, G. Müller, H. Müller, K. Oudrhiri, L. E. Phillips, A. Pichery, E. M. Rasel, C. A. Sackett, M. Sbroscia, W. P. Schleich, R. J. Thompson, and J. R. Williams, "Quantum gas mixtures and dual-species atom interferometry in space", Nature **623**, 502–508 (2023).

[104] D. Pertot, D. Greif, S. Albert, B. Gadway, and D. Schneble, "Versatile transporter apparatus for experiments with optically trapped bose–einstein condensates", Journal of Physics B: Atomic, Molecular and Optical Physics **42**, 215305 (2009).

[105] L. Krinner, "Exploring spontaneous emission phenomena using ultracold atomic matter waves", PhD thesis (Stony Brook University, 2018).

[106] M. Stewart, "Dynamics of matter-wave quantum emitters in engineered reservoirs", PhD thesis (Stony Brook University, 2020).

[107] J. Kwon, "Simulating strongly-coupled light-matter systems with ultracold atoms", PhD thesis (Stony Brook University, 2022).

[108] Y. Kim, "Exploring collective radiative phenomena with ultracold matter waves", PhD thesis (Stony Brook University, 2024).

[109] L. J. LeBlanc and J. H. Thywissen, "Species-specific optical lattices", Phys. Rev. A **75**, 053612 (2007).

[110] Z. Wilhelm, "Mott–Hubbard transition of cold atoms in optical lattices", Journal of Optics B: Quantum and Semiclassical Optics **5**, S9 (2003).

[111] M. O. Scully, E. S. Fry, C. H. R. Ooi, and K. Wódkiewicz, "Directed spontaneous emission from an extended ensemble of N atoms: timing is everything", Phys. Rev. Lett. **96**, 010501 (2006).

[112]M. Born and V. Fock, “Beweis des Adiabatensatzes”, Zeitschrift für Physik **51**, 165–180 (1928).

[113]P. L. Gould, G. A. Ruff, and D. E. Pritchard, “Diffraction of atoms by light: The near-resonant Kapitza-Dirac effect”, Phys. Rev. Lett. **56**, 827–830 (1986).

[114]Y. Zhai, C. H. Carson, V. A. Henderson, P. F. Griffin, E. Riis, and A. S. Arnold, “Talbot-enhanced, maximum-visibility imaging of condensate interference”, Optica **5**, 80–85 (2018).

[115]W. Gerlach and O. Stern, “Der experimentelle Nachweis der Richtungsquantelung im Magnetfeld”, Zeitschrift für Physik **9**, 349–352 (1922).

[116]G. Breit and I. I. Rabi, “Measurement of nuclear spin”, Phys. Rev. **38**, 2082–2083 (1931).

[117]L. Krinner, M. Stewart, A. Pazmiño, and D. Schneble, “In situ magnetometry for experiments with atomic quantum gases”, Review of Scientific Instruments **89**, 013108 (2018).

[118]J. Kwon, Y. Kim, A. Lanuza, and D. Schneble, “Formation of matter-wave polaritons in an optical lattice”, Nature Physics **18**, 657–661 (2022).

[119]J. Orear, A. H. Rosenfeld, and R. A. Schluter, *Nuclear physics: a course given by Enrico Fermi at the University of Chicago* (University of Chicago Press, 1950).

[120]K. Vodenkova and H. Pichler, “Continuous coherent quantum feedback with time delays: tensor network solution”, arXiv:2311.07302, [quant–ph] (2023).

[121]F. Lombardo, F. Ciccarello, and G. M. Palma, “Photon localization versus population trapping in a coupled-cavity array”, Physical Review A **89**, 053826 (2014).

[122]M. Scigliuzzo, G. Calajò, F. Ciccarello, D. Perez Lozano, A. Bengtsson, P. Scarlino, A. Wallraff, D. Chang, P. Delsing, and S. Gasparinetti, “Controlling atom-photon bound states in an array of Josephson-junction resonators”, Physical Review X **12**, 031036 (2022).

[123]F. Ciccarello, P. Lodahl, and D. Schneble, “Waveguide quantum electrodynamics”, Opt. Photon. News **35**, 34–41 (2024).

[124]S. R. Wilkinson, C. F. Bharucha, M. C. Fischer, K. W. Madison, P. R. Morrow, Q. Niu, B. Sundaram, and M. G. Raizen, “Experimental evidence for non-exponential decay in quantum tunnelling”, Nature **387**, 575–577 (1997).

[125]V. Jain, V. D. Kurilovich, Y. D. Dahmani, C. U. Lei, D. Mason, T. Yoon, P. T. Rakich, L. I. Glazman, and R. J. Schoelkopf, “Acoustic radiation from a superconducting qubit: from spontaneous emission to rabi oscillations”, Physical Review Applied **20**, 014018 (2023).

[126]R. Manenti, A. F. Kockum, A. Patterson, T. Behrle, J. Rahamim, G. Tancredi, F. Nori, and P. J. Leek, “Circuit quantum acoustodynamics with surface acoustic waves”, Nature Communications **8**, 975 (2017).

[127]D. Burgarth, P. Facchi, M. Ligabò, and D. Lonigro, “Hidden non-Markovianity in open quantum systems”, Physical Review A **103**, 012203 (2021).

[128] D. Lechner, R. Pennetta, M. Blaha, P. Schneeweiss, A. Rauschenbeutel, and J. Volz, "Light-matter interaction at the transition between cavity and waveguide QED", Physical Review Letters **131**, 103603 (2023).

[129] A. Kofman, G. Kurizki, and B. Sherman, "Spontaneous and induced atomic decay in photonic band structures", Journal of Modern Optics **41**, 353–384 (1994).

[130] T. Quang, M. Woldeyohannes, S. John, and G. S. Agarwal, "Coherent control of spontaneous emission near a photonic band edge: a single-atom optical memory device", Phys. Rev. Lett. **79**, 5238–5241 (1997).

[131] C. W. Hsu, B. Zhen, A. D. Stone, J. D. Joannopoulos, and M. Soljačić, "Bound states in the continuum", Nature Reviews Materials **1**, 16048 (2016).

[132] D. F. Walls and G. J. Milburn, *Quantum optics*, 2nd edn. (Springer, 2008).

[133] A. F. Kockum, "Quantum optics with giant atoms – the first five years", in *International symposium on mathematics, quantum theory, and cryptography*, Vol. 33, edited by T. Takagi et al., Mathematics for Industry (Springer, 2020).

[134] A. González-Tudela, C. S. Muñoz, and J. I. Cirac, "Engineering and harnessing giant atoms in high-dimensional baths: a proposal for implementation with cold atoms", Physical Review Letters **122**, 203603 (2019).

[135] K Rzazewski, M Lewenstein, and J. Eberly, "Threshold effects in strong-field photodetachment", Journal of Physics B: Atomic and Molecular Physics **15**, L661 (1982).

[136] M. Lewenstein, J. Zakrzewski, and T. W. Mossberg, "Spontaneous emission of atoms coupled to frequency-dependent reservoirs", Phys. Rev. A **38**, 808–819 (1988).

[137] P. R. Berman and G. W. Ford, "Spectrum in spontaneous emission: beyond the weisskopf-wigner approximation", Physical Review A **82**, 023818 (2010).

[138] E. Yablonovitch, "Inhibited spontaneous emission in solid-state physics and electronics", Physical Review Letters **58**, 2059–2062 (1987).

[139] B. Windt, M. Bello, E. Demler, and J. I. Cirac, "Fermionic matter-wave quantum optics with cold-atom impurity models", Phys. Rev. A **109**, 023306 (2024).

[140] N. Ashcroft and N. Mermin, "Solid State Physics", in (Saunders College, Philadelphia, 1976) Chap. 8, prob. 1.

[141] D Frenkel and R Portugal, "Algebraic methods to compute Mathieu functions", Journal of Physics A: Mathematical and General **34**, 3541–3551 (2001).

[142] B. Fine and G. Rosenberger, "The fundamental theorem of algebra", in, Undergraduate Texts in Mathematics (Springer New York, 2012), pp. 70–71.

[143] R. P. Feynman and R. Leighton, *The Feynman lectures on physics*, Vol. 1 (Addison-Wesley, 1977), pp. 22–10.

[144] W. Dunham, *Euler: the master of us all*, Dolciani Mathematical Expositions v. 22 (Mathematical Association of America, 1999).

[145] A. Asenjo-Garcia, J. D. Hood, D. E. Chang, and H. J. Kimble, "Atom-light interactions in quasi-one-dimensional nanostructures: a Green's-function perspective", Physical Review A **95**, 033818 (2017).

[146] C. Joshi, F. Yang, and M. Mirhosseini, “Resonance fluorescence of a chiral artificial atom”, Phys. Rev. X **13**, 021039 (2023).

[147] I. Carusotto and C. Ciuti, “Quantum fluids of light”, Reviews of Modern Physics **85**, 299–366 (2013).

[148] D. N. Basov, A. Asenjo-Garcia, P. J. Schuck, X. Zhu, and A. Rubio, “Polariton panorama”, Nanophotonics **10**, 549–577 (2021).

[149] P. Chandra and B. Doucot, “Possible spin-liquid state at large S for the frustrated square heisenberg lattice”, Phys. Rev. B **38**, 9335–9338 (1988).

[150] E. Dagotto and A. Moreo, “Phase diagram of the frustrated spin-1/2 heisenberg antiferromagnet in 2 dimensions”, Physical Review Letters **63**, 2148–2151 (1989).

[151] A. B. Kuklov and B. V. Svistunov, “Counterflow superfluidity of two-species ultracold atoms in a commensurate optical lattice”, Physical Review Letters **90**, `10.1103/PhysRevLett.90.100401` (2003).

[152] E. Altman, W. Hofstetter, E. Demler, and M. D. Lukin, “Phase diagram of two-component bosons on an optical lattice”, New Journal of Physics **5**, `10.1088/1367-2630/5/1/113` (2003).

[153] R. Liao, F. Xiong, and X. Chen, “Simulating an exact one-dimensional transverse ising model in an optical lattice”, Physical Review A **103**, 043312 (2021).

[154] L. Balents, “Spin liquids in frustrated magnets”, Nature **464**, 199–208 (2010).

[155] C. Sträter and A. Eckardt, “Orbital-driven melting of a bosonic mott insulator in a shaken optical lattice”, Physical Review A **91**, 053602 (2015).

[156] C. Kollath, A. Iucci, T. Giamarchi, W. Hofstetter, and U. Schollwöck, “Spectroscopy of ultracold atoms by periodic lattice modulations”, Physical Review Letters **97**, 050402 (2006).

[157] S. Bay, P. Lambropoulos, and K. Mølmer, “Atom-atom interaction in strongly modified reservoirs”, Phys. Rev. A **55**, 1485–1496 (1997).

[158] H. J. Kimble, “The quantum internet”, Nature **453**, 1023–1030 (2008).

[159] I. de Vega and D. Alonso, “Dynamics of non-Markovian open quantum systems”, Reviews of Modern Physics **89**, 015001 (2017).

[160] S. J. Masson and A. Asenjo-Garcia, “Universality of dicke superradiance in arrays of quantum emitters”, Nature Communications **13**, 2285 (2022).

[161] P. M. Lenggenhager, A. Stegmaier, L. K. Upreti, T. Hofmann, T. Helbig, A. Vollhardt, M. Greiter, C. H. Lee, S. Imhof, H. Brand, T. Kießling, I. Boettcher, T. Neupert, R. Thomale, and T. Bzdušek, “Simulating hyperbolic space on a circuit board”, Nature Communications **13**, 4373 (2022).

[162] J. Mlynek, A. Abdumalikov, C. Eichler, and A. Wallraff, “Observation of dicke superradiance for two artificial atoms in a cavity with high decay rate”, Nature Communications **5**, 5186 (2014).

[163] H. Breuer and F. Petruccione, *The theory of open quantum systems* (Oxford University Press, 2002).

[164] S. J. Masson, I. Ferrier-Barbut, L. A. Orozco, A. Browaeys, and A. Asenjo-Garcia, "Many-body signatures of collective decay in atomic chains", Physical Review Letters **125**, 263601 (2020).

[165] C. N. Yang, "Some exact results for the many-body problem in one dimension with repulsive delta-function interaction", Phys. Rev. Lett. **19**, 1312–1315 (1967).

[166] V. E. Korepin, "Calculation of norms of bethe wave functions", Communications in Mathematical Physics **86**, 391–418 (1982).

[167] F. Levkovich-Maslyuk, "The bethe ansatz", Journal of Physics A: Mathematical and Theoretical **49**, 323004 (2016).

[168] B. Vacchini and H.-P. Breuer, "Exact master equations for the non-Markovian decay of a qubit", Physical Review A **81**, 042103 (2010).

[169] T. Tufarelli, M. S. Kim, and F. Ciccarello, "Non-Markovianity of a quantum emitter in front of a mirror", Physical Review A **90**, 012113 (2014).

[170] D. Roy, C. M. Wilson, and O. Firstenberg, "Colloquium: strongly interacting photons in one-dimensional continuum", Reviews of Modern Physics **89**, 021001 (2017).

[171] F. Dinc, İ. Ercan, and A. M. Brańczyk, "Exact Markovian and non-Markovian time dynamics in waveguide QED: collective interactions, bound states in continuum, superradiance and subradiance", Quantum **3**, 213 (2019).

[172] P. Lodahl, S. Mahmoodian, and S. Stobbe, "Interfacing single photons and single quantum dots with photonic nanostructures", Rev. Mod. Phys. **87**, 347–400 (2015).

[173] Y. Chu, P. Kharel, W. H. Renninger, L. D. Burkhart, L. Frunzio, P. T. Rakich, and R. J. Schoelkopf, "Quantum acoustics with superconducting qubits", Science **358**, 199–202 (2017).

[174] M. Xu, D. A. Tieri, E. C. Fine, J. K. Thompson, and M. J. Holland, "Synchronization of two ensembles of atoms", Physical Review Letters **113**, 154101 (2014).

[175] J. M. Weiner, K. C. Cox, J. G. Bohnet, and J. K. Thompson, "Phase synchronization inside a superradiant laser", Physical Review A **95**, 033808 (2017).

[176] C. Gonzalez-Ballestero, F. J. García-Vidal, and E. Moreno, "Non-Markovian effects in waveguide-mediated entanglement", New Journal of Physics **15**, 073015 (2013).

[177] F. Lohof, D. Schumayer, D. A. W. Hutchinson, and C. Gies, "Signatures of superradiance as a witness to multipartite entanglement", Physical Review Letters **131**, 063601 (2023).

[178] C. Vega, D. Porras, and A. González-Tudela, "Topological multimode waveguide QED", Phys. Rev. Res. **5**, 023031 (2023).

[179] T. Karzig, C.-E. Bardyn, N. H. Lindner, and G. Refael, "Topological polaritons", Phys. Rev. X **5**, 031001 (2015).

[180] J. Reeves, L. Krinner, M. Stewart, A. Pazmiño, and D. Schneble, "Nonadiabatic diffraction of matter waves", Physical Review A **92**, 023628 (2015).

[181] P. A. M. Dirac, "Quantum mechanics of many-electron systems", Proc. R. Soc. Lond. A **123**, 714–733 (1929).

[182] M. Abramowitz and I. A. Stegun, *Handbook of mathematical functions, With formulas, graphs, and mathematical tables*, Vol. 55, Applied Mathematics Series (National Bureau of Standards, tenth printing, ch. 7, 1972) Chap. 17, pp. 590–591.

Appendix A

Dynamics of the transformed field amplitudes for two excitations

This appendix reproduces another one from [70] verbatim, with minimal adaptations.

The TSE for the transformed fields (3.87) and the initial conditions $A(0) = 1$ and $B_{p,q}(0) = C_{j,q}(0) = 0$ denoting two fully excited emitters, becomes

$$\begin{cases} \omega\tilde{A} - 1 = 2\Delta\tilde{A} + g\sum\limits_{q}\left(e^{iqx_1}\tilde{C}_{2,q} + e^{iqx_2}\tilde{C}_{1,q}\right) \\ \omega\tilde{B}_{p,q} = (\omega_p + \omega_q)\tilde{B}_{p,q} \\ \qquad +g\sum\limits_{j=1}^{2}\left(e^{-ipx_j}\tilde{C}_{j,q} + e^{-iqx_j}\tilde{C}_{j,p}\right) \qquad \text{if } p < q \\ \omega\tilde{B}_{q,q} = 2\omega_q\tilde{B}_{q,q} + \sqrt{2}g\sum\limits_{j=1}^{2} e^{-iqx_j}\tilde{C}_{j,q} \\ \omega\tilde{C}_{j,q} = (\Delta + \omega_q)\tilde{C}_{j,q} + ge^{iqx_j}\tilde{A} \\ \quad +g\left(\sum\limits_{p<q} e^{ipx_j}\tilde{B}_{p,q} + \sum\limits_{q<p} e^{ipx_j}\tilde{B}_{q,p} + \sqrt{2}e^{iqx_j}\tilde{B}_{q,q}\right), \end{cases} \tag{A.1}$$

where $x_1 = -d/2$ and $x_2 = +d/2$ are the positions of the quantum emitters on the waveguide. Solving for the $\tilde{C}_{j,q}$, we get Eqns. (3.88) and the additional equation

$$\begin{aligned} \left(\omega - \Delta - \omega_q\right)\tilde{C}_{j,q} = \frac{ge^{iqx_j}}{\omega - 2\Delta} + g^2\sum_p \frac{e^{i(px_1+qx_j)}\tilde{C}_{2,p} + e^{i(px_2+qx_j)}\tilde{C}_{1,p}}{\omega - 2\Delta} \\ + g^2\sum_p\sum_{j'=1}^{2}\frac{e^{ip(x_j-x_{j'})}\tilde{C}_{j',q} + e^{i(px_j-qx_{j'})}\tilde{C}_{j',p}}{\omega - \omega_p - \omega_q}. \end{aligned} \tag{A.2}$$

We can use this equation to prove that $\tilde{C}_{1,q}(\omega) = \tilde{C}^*_{2,q}(\omega)$ for all $\omega \in \mathbb{R}$. Beyond informing us about the form of the bound states (see FIG. 3.25b), this allows us to obtain $\tilde{C}_{2,q}$ from $\tilde{C}_{1,q}$ through analytic continuation. For the proof, notice that conjugating this equation while rewriting $j \to \neg j$ and $j' \to \neg j'$, the equation becomes

$$\begin{aligned}(\omega - \Delta - \omega_q)\, \tilde{C}^*_{\neg j,q} = \frac{g e^{iqx_j}}{\omega - 2\Delta} + g^2 \sum_p \frac{e^{i(px_1 + qx_j)} \tilde{C}^*_{1,p} + e^{i(px_2 + qx_j)} \tilde{C}^*_{2,p}}{\omega - 2\Delta} \\ + g^2 \sum_p \sum_{j'=1}^{2} \frac{e^{ip(x_j - x_{j'})} \tilde{C}^*_{\neg j',q} + e^{i(px_j - qx_{j'})} \tilde{C}^*_{\neg j',p}}{\omega - \omega_p - \omega_q},\end{aligned} \tag{A.3}$$

which is identical to the original writing (A.2) after exchanging $\tilde{C}_{1,q} \leftrightarrow \tilde{C}^*_{2,q}$. Since the dynamics are unequivocally determined by the SE and initial conditions, (A.2) has a unique solution and therefore $\tilde{C}_{1,q} = \tilde{C}^*_{2,q}$. We note that this also implies through (3.88) that $\tilde{A}, \tilde{B}_{p,q} \in \mathbb{R}$ for $\omega \in \mathbb{R}$.

Using this result, Eqn. (A.2) with $j = 1$ and arbitrary $\omega \in \mathbb{C}$ can also be written as

$$\begin{aligned}(\delta\omega - \Delta) C(\omega, z) = \frac{g/z}{\omega - 2\Delta} \\ + \frac{g^2/z}{2\pi i} \oint \left\{ \frac{2C(\omega, z')}{\omega - 2\Delta} + 2\frac{zC(\omega, z) + C(\omega, 1/z)/z' + (z + z')C(\omega, z')}{1 + 2\delta\omega\, z' + z'^2} \right\} \mathrm{d}z'\end{aligned} \tag{A.4}$$

in terms of the function $C(\omega, z)$ defined in (3.89). After splitting C into symmetric and antisymmetric parts as in (3.91), this equation simplifies into (3.92).

Appendix B

Increments of C_σ

This appendix reproduces another one from [70] verbatim, with minimal adaptations.

As mentioned in Sec. 3.6.5, Eqn. (3.92) imposes a very particular analytic structure on the function $C_\sigma(z)$. For starters, knowing the value of the function for values of $z \in \mathbb{S}^1$ (corresponding to real quasimomenta) allows to determine the analytic continuation $C_\sigma^{\textcircled{0}}(z)$ of the function to all $z \in \mathbb{C} \setminus \left(\zeta\left(\mathbb{S}^1\right) \cup \zeta^{-1}\left(\mathbb{S}^1\right)\right)$, through direct integration of the RHS in (3.92).

Continuing the function to $C_\sigma^{\textcircled{1}}(z)$ beyond the $\zeta\left(\mathbb{S}^1\right)$ branch cut (in FIG. 3.24**a**, this corresponds to crossing from the second lowest to the lowest sheet) is possible by deforming the integration contour, as shown in FIG. B.1. Subsequently applying the residue theorem

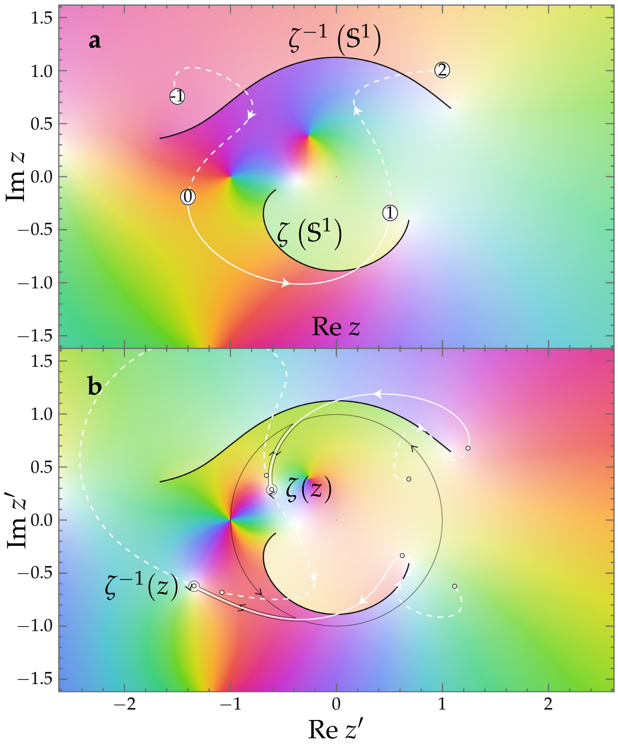

FIGURE B.1: **a,** Domain coloring plot of $C_\sigma^{\textcircled{0}}(z)$ for the same parameters as in FIG. 3.24. In white, a path for z that crosses the branch cuts $\zeta^{\pm 1}\left(\mathbb{S}^1\right)$ (in black) is suggested. The circled numbers enumerate the analytic continuations $C_\sigma^{\textcircled{-1}}(z)$, $C_\sigma^{\textcircled{0}}(z)$, $C_\sigma^{\textcircled{1}}(z)$, and $C_\sigma^{\textcircled{2}}(z)$ that the path traverses. **b,** Corresponding domain coloring plot of Eqn. (3.92)'s integrand at $z = 0.5 - 0.4i$. The integration contour (originally $\mathbb{S}^1$, in black) has been adapted to avoid the mobile poles $\zeta^{\pm 1}(z)$, whose trajectory as z follows the white path in **a** is marked with white lines and black circles. Figure reproduced from [70].

results in

$$\begin{aligned} C_\sigma^{\textcircled{1}}(z) &= \frac{\nu_{-,\sigma}(z)}{\nu_{+,\sigma}(z)} C_\sigma^{\textcircled{0}}(z) \\ &- 2\nu_{-,\sigma}(z) \frac{\zeta(z)+\sigma}{\zeta(z)-\zeta^{-1}(z)} \times \begin{cases} C_\sigma^{\textcircled{0}}(\zeta(z)) & \text{if } |z|<1 \\ C_\sigma^{\textcircled{1}}(\zeta(z)) & \text{if } |z|>1, \end{cases} \end{aligned} \tag{B.1}$$

where for briefness we introduced

$$\nu_{\pm,\sigma}(z) := \frac{\frac{1}{z}+\sigma}{g^{-2}\left(\delta\omega-\Delta\right) \pm \sigma \frac{\sqrt{\delta\omega-\sigma}}{\sqrt{\delta\omega+\sigma}} - \sigma}. \tag{B.2}$$

We note that crossing the same branch cut again in either direction brings you back to $C_\sigma^{\textcircled{0}}(z)$, as the modification to the integration contour is reverted around the poles. This is no longer the case (i.e. $C_\sigma^{\textcircled{2}}(z) \neq C_\sigma^{\textcircled{0}}(z)$) if one subsequently crosses the other branch cut instead, but unexpectedly both increments

$$\delta C_\sigma(z) = C_\sigma^{\textcircled{1}}(z) - C_\sigma^{\textcircled{0}}(z) \tag{B.3}$$

and

$$\delta^2 C_\sigma(z) = C_\sigma^{\textcircled{0}}(z) - C_\sigma^{\textcircled{2}}(z) \tag{B.4}$$

become meromorphic functions when multiplied by $\sqrt{\delta\omega+\sigma}/\sqrt{\delta\omega-\sigma}$.

The proof for δC_σ is elaborated (for $\delta^2 C_\sigma$ it then follows from (3.101)). We start by noticing that, by construction, the only possible branch cuts of δC_σ are $\zeta\left(\mathbb{S}^1\right)$ and $\zeta^{-1}\left(\mathbb{S}^1\right)$. This is how the function extends when we cross them:

$$\begin{gathered} \delta C_\sigma = C_\sigma^{\textcircled{1}} - C_\sigma^{\textcircled{0}} \xrightarrow{\zeta\left(\mathbb{S}^1\right)} C_\sigma^{\textcircled{0}} - C_\sigma^{\textcircled{1}} = -\delta C_\sigma \\ \delta C_\sigma = C_\sigma^{\textcircled{1}} - C_\sigma^{\textcircled{0}} \xrightarrow{\zeta^{-1}\left(\mathbb{S}^1\right)} C_\sigma^{\textcircled{2}} - C_\sigma^{\textcircled{-1}}. \end{gathered}$$

The last function can also be equated to $-\delta C_\sigma$. To do so, one should write $C_\sigma^{\textcircled{2}}(z)$ and $C_\sigma^{\textcircled{-1}}(z)$ in terms of $C_\sigma^{\textcircled{0}}(z)$ and $C_\sigma^{\textcircled{0}}(\zeta(z))$, which is a tedious calculation but shows that indeed the equality holds iff

$$\begin{aligned} &4\frac{\zeta(z)+\sigma}{\zeta(z)-\zeta^{-1}(z)} \frac{z+\sigma}{z-z^{-1}} \\ &+ \left(\nu_{+,\sigma}^{-1}(\zeta(z)) - \nu_{-,\sigma}^{-1}(\zeta(z))\right)\left(\nu_{+,\sigma}^{-1}(z) - \nu_{-,\sigma}^{-1}(z)\right) = 0, \end{aligned} \tag{B.5}$$

which, in turn, holds because

$$\nu_{+,\sigma}^{-1}(z) - \nu_{-,\sigma}^{-1}(z) = \frac{2\sigma}{\sigma+z^{-1}} \frac{\sqrt{\delta\omega-\sigma}}{\sqrt{\delta\omega+\sigma}}. \tag{B.6}$$

This concludes that $\delta C_\sigma(z)\sqrt{\delta\omega+\sigma}/\sqrt{\delta\omega-\sigma}$ is meromorphic.

In fact, using these formulas and briefly denoting $\mathrm{sl}(z) := \operatorname{sign}\log|z|$ for all $z \notin \mathbb{S}^1 \cup \{0\}$, one can rewrite the function as

$$\begin{gathered}\delta C_\sigma(z)\frac{\nu_{+,\sigma}(\zeta(z))}{\nu_{-,\sigma}(z)\nu_{-\,\mathrm{sl}(z),\sigma}(\zeta(z))} = \\ \frac{2\sigma}{\sigma+z^{-1}}\frac{\sqrt{\delta\omega-\sigma}}{\sqrt{\delta\omega+\sigma}}C_\sigma(z) - 2\frac{\zeta(z)+\sigma}{\zeta(z)-\zeta^{-1}(z)}C_\sigma(\zeta(z))\end{gathered} \tag{B.7}$$

which can be regarded as the way in which $C_\sigma(z)$ transforms under the $z \leftrightarrow \zeta(z)$ hidden symmetry (see Sec. 3.6.4). We use this formula to extract the symmetries of δC_σ,

$$\begin{gathered}\delta C_\sigma\left(\tfrac{1}{z}\right) = \sigma z\frac{\nu_{+\,\mathrm{sl}(z),\sigma}(\zeta(z))}{\nu_{-\,\mathrm{sl}(z),\sigma}(\zeta(z))}\delta C_\sigma(z) \\ \delta C_\sigma\left(\zeta(z)\right) = \mathrm{sl}(z)\frac{\sqrt{\delta\omega+\sigma}}{\sqrt{\delta\omega-\sigma}}\frac{\nu_{+\,\mathrm{sl}(z),\sigma}(\zeta(z))}{\nu_{-,\sigma}(z)}\frac{z+\sigma}{z-\sigma}\delta C_\sigma(z).\end{gathered} \tag{B.8}$$

With these symmetries, we build up the projectors

$$\begin{gathered}P_{\mathrm{inv}}\{f_\sigma\}(z) = \tfrac{1}{2}\left(f_\sigma(z) + \tfrac{\sigma}{z}\frac{\nu_{-\,\mathrm{sl}(z),\sigma}(\zeta(z))}{\nu_{+\,\mathrm{sl}(z),\sigma}(\zeta(z))}f_\sigma\left(z^{-1}\right)\right) \\ P_\zeta\{f_\sigma\}(z) = \tfrac{1}{2}\left(f_\sigma(z) + \mathrm{sl}(z)\frac{\sqrt{\delta\omega-\sigma}}{\sqrt{\delta\omega+\sigma}}\frac{\nu_{-,\sigma}(z)}{\nu_{+\,\mathrm{sl}(z),\sigma}(\zeta(z))}\frac{z-\sigma}{z+\sigma}f_\sigma\left(\zeta(z)\right)\right)\end{gathered} \tag{B.9}$$

that take functions of the form meromorphic× $\sqrt{\delta\omega-\sigma}/\sqrt{\delta\omega+\sigma}$ and imbues in them the corresponding symmetry. $P_\zeta \circ P_{\mathrm{inv}}$ spans a linear subspace of functions so limited that only one has the correct asymptotic dependence for $\delta C_\sigma(z \to \infty)$, which can be found by using (3.92) to extract

$$\begin{aligned}C_\sigma(z) = {} & \sigma z^{-1}\frac{g\left(1+2g\tilde{C}_{1,2}\right)}{\omega-2\Delta} \\ & + g\frac{1-2\sigma(\omega-\Delta)+2g\tilde{C}_{1,1}(\omega-2\Delta)+2g\tilde{C}_{1,2}(1-\sigma\omega)}{z^2(\omega-2\Delta)} + O\left(z^{-3}\right)\end{aligned} \tag{B.10}$$

and combine it with (B.7) to obtain

$$\begin{aligned}\delta C_\sigma(z) &= 8g^3z^{-3}(2g\tilde{C}_{1,1}\sigma-1) + O\left(z^{-4}\right) \\ &= 8g^3\sigma z^2(2g\tilde{C}_{1,1}\sigma-1) + O\left(z^3\right).\end{aligned} \tag{B.11}$$

The only function matching the symmetries and asymptotic dependence is listed as $\delta C_\sigma(z)$ in TABLE 3.2.

Appendix C

The function Φ

This appendix reproduces another one from [70] verbatim, with minimal adaptations.

The core idea behind our solution is that since the overall form of the analytic structure of $C_\sigma(z)$ (see FIG. 3.24) is independent of the system parameters, we can define a simpler parameter-free version $\Phi(z)$ of the function hosting the same overall structure.

Starting from Eqn. (3.98), we have the following properties.

i. Symmetries:

$$\begin{cases} \Phi(z) = -\Phi(1/z) \\ \Phi(z) = \mathrm{sl}(z)(\Phi(\zeta(z)) + 1/2) \end{cases} \tag{C.1}$$

ii. Asymptotic expansion:

$$\Phi(z) = \frac{1}{4}\frac{z+1}{z-1} + O\left(|z|^{-1}\right) \tag{C.2}$$

iii. $\Phi(-1) = 0$ and $(z-1)\Phi(z) \in \mathcal{H}\big(\mathbb{C} \setminus \left(\zeta\left(\mathbb{S}^1\right) \cup \zeta^{-1}\left(\mathbb{S}^1\right)\right)\big)$. This can be used to regularize the integral equation of $(z-1)\Phi(z)$ in the unit circumference. This allows for a Picard iteration scheme to both prove existence and uniqueness and to compute the numerical solution of the equation, albeit not efficiently.

iv. Analytic extension (see FIG. 3.24**b**). It can be achieved by carefully changing the shape of the integration contour, completely analogous to the study of the analytic extensions of $C_\sigma(z)$ presented in App. B.

v. An algorithm to compute Φ is the following. Due to the analytic structure of this function, it can be written as

$$\Phi(z) = -\frac{1}{2} + \frac{1 + \sum_{n=1}^{\infty} a_n z^n}{4(1-z)} \sqrt{\frac{\delta\omega - 1}{\delta\omega + 1}} \quad \forall |z| < \frac{1}{|\zeta(\pm 1)|}. \tag{C.3}$$

Applying (C.1), this has to be equal to

$$\Phi_\zeta(z) = \frac{1 + \sum_{n=1}^{\infty} a_n \zeta(z)^n}{4(1-\zeta(z))} \frac{z+1}{z-1} \quad \forall z \in \mathbb{C}, \tag{C.4}$$

where the convergence is improved to the whole complex plane thanks to the fact that always $|\zeta(z)| \leq 1$. Now, one can show that any function with the generic analytic shape of (C.3) that also has property (C.1) satisfies equation (3.98). In other words, enforcing

$$\Phi(z) = \Phi_\zeta(z) \qquad \forall |z| < \min\{|\zeta(1)|^{-1}, |\zeta(-1)|^{-1}\} \tag{C.5}$$

can be used to fit the real coefficients $\{a_n\}_{n=1}^{\infty}$ unequivocally, and subsequently evaluate Φ in any point of the complex plane through the expression for $\Phi_\zeta(z)$ in (C.5). Since it is essentially solving a least-square problem, this method is efficient in practice if one chooses to enforce this along equispaced points on the circumference $\mathbb{S}^1$ excluding the singular $z = 1$ (this choice makes the branch cut of the $a_n(\omega)$ to be at $\omega \in [-2, 2]$). And the accuracy of the algorithm gets compromised the closer one gets to this branch cut.

vi. The analytic structure displayed in FIG. 3.24**b** simplifies greatly by taking the derivative with respect to z, to the point that it can be expressed algebraically as

$$\Phi'(z) \propto \frac{(z-z_0)(z-z_0^{-1})(z-\zeta(z_0))(z-\zeta^{-1}(z_0))}{(\delta\omega^2-1)z^2(z-1)^2}\frac{\sqrt{\delta\omega-1}}{\sqrt{\delta\omega+1}}, \tag{C.6}$$

where z_0 is one of the four symmetric points where $\Phi'(z_0) = 0$.

vii. Reintegrating the expression above means that $\Phi(z)$ can be expressed in terms of elliptic integrals [182]. In the Legendre normal form, the incomplete elliptic integral of the first and second kind we use are presented in TABLE 3.2 together with the integrated expression for $\Phi(z)$. Our choice of branch cuts for these functions matches the branch cuts of their respective integrands (where we also choose $\arg\sqrt{z} \in (-\pi/2, \pi/2]$).

While integrating, it is useful to notice that $z_0 \equiv z_0(\omega)$ can be extracted from

$$\omega + \frac{z_0 + z_0^{-1}}{2} = \frac{\omega}{2} - \frac{\omega+2}{2}\sqrt{1 - \frac{2\omega}{\omega + 1 + k\cdot\left(1 - \frac{E\left(k^{-1}\right)}{K\left(k^{-1}\right)}\right)}}, \tag{C.7}$$

whereas taking the opposite sign in the large square root yields $\omega + (\zeta(z_0) + \zeta^{-1}(z_0))/2$ instead. Also one can express the residue

$$\mathrm{Res}\{\Phi(z), z = 1\} = \frac{\sqrt{\omega(2+\omega)k^{-1}}}{\pi} K\left(k^{-1}\right). \tag{C.8}$$

The second line in the closed formula of $\Phi(z)$ at TAB. 3.2 is very particular and, although there is no value of ω or z such that $x(z) = 1$, if we enforce this, the second line becomes ±1 due to Legendre's relation. In other words, excluding algebraic functions (see Sec. 3.6.4), $\Phi(z)$ is a modification of Legendre's relation for incomplete elliptic integrals.

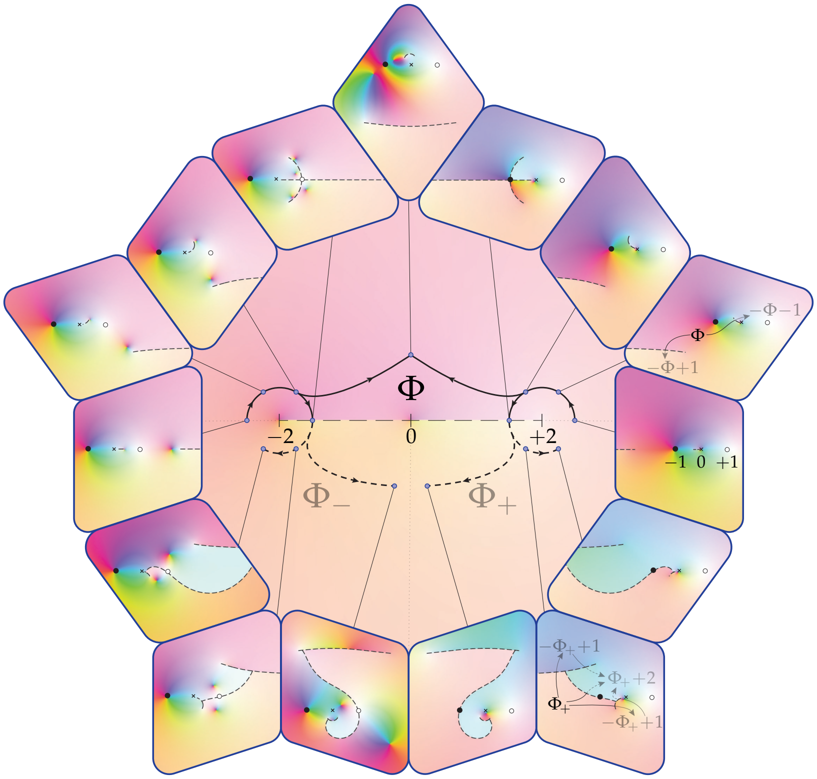

FIGURE C.1: *Analytic continuations of* $\Phi(\omega, z)$. The central image is a domain coloring plot of $\mathrm{Res}\{\Phi(\omega, z), z = 1\}$ in the complex ω-plane. Around it, we show domain coloring plots (this time in the complex z-plane) of $\Phi(i, z)$ and $\Phi(\pm 2 + e^{i\pi n/3}/2, z)$ for $n \in \{0, 1, 2, 3\}$, together with the analytic continuations $\Phi_\pm(-i \pm 1/4, z)$ and $\Phi_\pm(\pm 2 + e^{i\pi n/3}/2, z)$ for $n \in \{4, 5\}$. At values $\omega = 2 \pm e^{i\pi/3}/2$, we also indicate how the function analytically continues in $z \in \mathbb{C}$. For simplicity, instead of complex axes we use the ω-values 0 and ± 2 and the z-values of -1 (black dots), 0 (small crosses), and +1 (white dots) as a reference system for the complex coordinates. Figure reproduced from [70].

viii. If we include the dependencies in ω explicitly, we have the additional symmetry

$$\Phi(\omega, z) = \Phi(-\omega, -z) + \frac{\mathrm{sgnRe}\,\omega \;\; 2\omega\left(z^2 + \omega z + 1\right) K\left(k^{-1}(\omega)\right)}{\pi\left(z^2 - 1\right)\sqrt{k(\omega)}\sqrt{\delta\omega + 1}\sqrt{\delta\omega - 1}}. \tag{C.9}$$

ix. There is a two-particle continuum at $\omega \in [-2, 2]$, which represents a branch cut in the ω plane. We can use the closed form of $\Phi(\omega, z)$ to analytically continue it beyond the branch cut, which will be needed to compute the super- and subradiant states of the system. For that purpose, we introduce $\xi \equiv \xi(\omega, z)$ as

$$\xi = \frac{\zeta(z) - \zeta(-1)}{1 - \zeta(-1)\zeta(z)} \sqrt{x\left(0^+\right)^2 \frac{\zeta(z) - \zeta^{-1}(-1)}{\zeta(-1) - \zeta(z)}} \sqrt{x\left(0^+\right)^{-2} \frac{\zeta^{-1}(z) - \zeta(-1)}{\zeta^{-1}(-1) - \zeta^{-1}(z)}} \tag{C.10}$$

where $x\left(0^+\right)$ denotes the limit of the amplitude x (see TAB. 3.2) when $z \to 0$. It can be shown that $\xi \in \{-1, 1\}$ is a sign dependent on ω and z. Consequently, the extension $\Phi_+(\omega, z)$ of $\Phi(\omega, z)$ when ω crosses the positive part of the continuum $(0, 2)$ can then be written as

$$\begin{aligned}\Phi_+(z) = {} & \frac{-K(k)\sqrt{k}\,\mathrm{sgnRe}\,\omega}{2\pi}\left(\frac{z^{-1}-z}{1-\zeta(z)}+\frac{z+1}{z-1}(1+\omega)+2\frac{z-1}{z+1}\zeta(-1)-\frac{z^2-6z+1}{z^2-1}\zeta^{-1}(z)\right) \\ & +\xi\frac{2k\,\mathrm{sgnRe}\,\omega}{\pi i}\left(K(k)E\left(x^{-1};k^{-1}\right)-k^{-2}E(k)F\left(x^{-1};k^{-1}\right)-(1-k^{-2})K(k)F\left(x^{-1};k^{-1}\right)\right).\end{aligned} \tag{C.11}$$

It should be pointed out that $\Phi_+(\omega, z)$ is a continuation in the space of functions that still have a z dependence to be evaluated. To know the analytic extension of the function evaluated at a particular $z_0 \in \mathbb{C}$, one additionally has to take into account all the instances in which a branch cut of $\Phi(z)$ or $\Phi_+(z)$ crosses the point z_0 and correct for them accordingly. This is needed e.g. to plot $\tilde{A}(\omega)$ in FIG. 3.25**a**.

We caution that expression (C.11) is only valid for Re $\omega > 0$ and Im $\omega < 0$ if $(0, 2)$ is crossed from above to below (as illustrated in FIG. C.1), or for Re $\omega > 0$ and Im $\omega > 0$ if it is crossed from below. The corresponding continuation Φ_- for ω crossing $(-2, 0) \subset \mathbb{C}$ can be computed as

$$\Phi_-(\omega, z) = \Phi_+(-\omega, -z) + \frac{\mathrm{sgnRe}\,\omega\ \ 2\omega\sqrt{k(\omega)}\left(z^2+\omega z+1\right)K\left(k(\omega)\right)}{\pi\left(z^2-1\right)\sqrt{\delta\omega+1}\sqrt{\delta\omega-1}} \tag{C.12}$$

using the symmetry (C.9). Interestingly, Φ_+ and Φ_- have the same $z \leftrightarrow z^{-1}$ and $z \leftrightarrow \zeta(z)$ symmetries as Φ (see (i)), but they cannot be obtained through the algorithm described in ***v*** because their analytic structure is fundamentally different. They have an additional branch cut joining the previous two cuts ($\zeta^{\pm 1}\left(\mathbb{S}^1\right)$, see FIG. C.1). The appearance of this branch cut is topological and is the essence underlying the difficulty in computing superradiant decays in the system at hand.

x. An additional surprise is the center of the continuum $\omega = 0$, which is a branch point in the middle of the branch cut. This again can be appreciated in FIG. C.1, where two paths with different winding around this center lead to very different functions, although the paths end at similar frequencies. Obtaining an asymptotic expansion around $\omega = 0$ is very difficult, even with computer assistance and despite having a closed formula for the Φ function and its analytic extensions. The reason is the intricate ω-dependence of the function, which makes the problem intractable by ordinary methods. However, we can prove that

$$\begin{aligned}\mathrm{sl}(z)\Phi(\omega,z) =& \frac{1}{4}+\frac{i}{\pi}\log\left(\mathrm{sl}(z)\frac{z-1}{z+1}\right)+\frac{i}{\pi}\frac{z(z^2+1)}{(z^2-1)^2}\omega\log\omega+\frac{4i+(\pi-6i\log 2)(z+z^{-1})}{2\pi(z-z^{-1})^2}\omega\\ &+\frac{4-\left(z+z^{-1}\right)+\left(z+z^{-1}\right)^2-\frac{1}{4}\left(z+z^{-1}\right)^3}{\pi i\left(z-z^{-1}\right)^4}\omega^2\log\omega+O(\omega^2)\end{aligned} \tag{C.13}$$

by comparison to the logarithmic z-derivative of (C.6), which splits in simple summands. As we can see from the $\log\omega$ terms, Φ is responsible for the logarithmic corrections to the decay. Analogously one can find the behavior for $\omega \simeq -2$,

$$\begin{aligned}\Phi(\omega,z) =& \frac{2}{\pi}\arctan\left((1+\sqrt{2})\frac{\sqrt{3-2\sqrt{2}-z}}{\sqrt{3+2\sqrt{2}-z}}\right)-\frac{1}{2}+\frac{z(1+z)}{\sqrt{3-2\sqrt{2}-z}\sqrt{3+2\sqrt{2}-z}}\frac{(\omega+2)}{2\pi}\\ &+\frac{z(z+1)\sqrt{3-2\sqrt{2}-z}\sqrt{3+2\sqrt{2}-z}}{16\pi(z-1)^4}\left(\frac{1}{2}+i\pi+4\log 2-\frac{8z(1-4z+z^2)}{(1-6z+z^2)^2}-\log(\omega+2)\right)(\omega+2)^2\\ &+O\left(\log(\omega+2)(\omega+2)^3\right).\end{aligned} \tag{C.14}$$

Using (C.14) together with the symmetry (C.9), we find as well the behaviour for $\omega \simeq +2$

$$\begin{aligned}\Phi(\omega,z) =& \frac{2z\log\left(\frac{\omega-2}{16}\right)}{\pi(1-z)\sqrt{z+2\sqrt{2}+3}\sqrt{z-2\sqrt{2}+3}}+\frac{2}{\pi}\arctan\left(\left(\sqrt{2}+1\right)\frac{\sqrt{z-2\sqrt{2}+3}}{\sqrt{z+2\sqrt{2}+3}}\right)-\frac{1}{2}\\ &-\frac{\frac{(z+1)^2\log\left(\frac{\omega-2}{16}\right)}{z^2+6z+1}-\frac{4z}{(z+1)^2}}{\sqrt{z+2\sqrt{2}+3}\sqrt{z-2\sqrt{2}+3}}\frac{z(\omega-2)}{2\pi(z-1)}\\ &+\left(\frac{\left(z^4+28z^3+38z^2+28z+1\right)\log\left(\frac{\omega-2}{16}\right)}{\left(z+2\sqrt{2}+3\right)^{5/2}\left(z-2\sqrt{2}+3\right)^{5/2}}+\frac{2\left(z^4+4z^3-18z^2+4z+1\right)}{(z+1)^4\sqrt{z+2\sqrt{2}+3}\sqrt{z-2\sqrt{2}+3}}\right)\frac{z(\omega-2)^2}{32\pi(z-1)}\\ &+O\left(\log(\omega+2)(\omega+2)^3\right).\end{aligned} \tag{C.15}$$

Appendix D

Constructive proof of the connection between Φ and C_σ

This appendix reproduces another one from [70] verbatim.

By design, $C_\sigma(z)$ and $\frac{1}{2}\delta^2 C_\sigma(z)\Phi(z)$ have a similar analytic structure with the same increment every two Riemann sheets (see FIG. 3.24). As a result, $C_\sigma(z) - \frac{1}{2}\delta^2 C_\sigma(z)\Phi(z)$ can be thought of as having only two Riemann sheets. The sum of these two sheets gives $r_\sigma(z) := 2C_\sigma(z) - \delta^2 C_\sigma(z)(\Phi(z) + 1/2) + \delta C_\sigma(z)$ (equivalent to Eqn. (3.102)), which is a meromorphic function by construction.

The functions generating $r_\sigma(z)$ all obey certain symmetry rules for the inversion $z \leftrightarrow 1/z$ and for $z \leftrightarrow \zeta(z)$, which in terms of r_σ read as

$$r_\sigma\left(\frac{1}{z}\right) = r_\sigma(z)\sigma z \tag{D.1}$$

and

$$r_\sigma\left(\zeta(z)\right) = -\frac{1+\sigma/\zeta(z)}{1+\sigma/z} r_\sigma(z) + \gamma_\sigma(z), \tag{D.2}$$

where

$$\gamma_\sigma(z) = \tfrac{\delta^2 C_\sigma(z) - 2\delta C_\sigma(z)}{\zeta(z)+\sigma}\left(\tfrac{\delta\omega-\sigma}{1+\sigma/z} + \tfrac{\zeta(z)-\zeta^{-1}(z)}{2\nu_{-,\sigma}(z)}\right). \tag{D.3}$$

These symmetries can be imposed in any ansatz $f_\sigma(z)$ for $r_\sigma(z)$ through the affine projectors (in the space of meromorphic functions)

$$\begin{cases} \mathcal{P}_{inv}\{f_\sigma\}(z) := \left(f_\sigma(z) + \frac{\sigma}{z} f_\sigma\left(\frac{1}{z}\right)\right)/2 \\ \mathcal{P}_\zeta\{f_\sigma\}(z) := \frac{f_\sigma(z)}{2} - \frac{1}{2}\frac{1+\sigma/z}{1+\sigma/\zeta(z)}\left(f_\sigma(\zeta(z)) - \gamma_\sigma(z)\right). \end{cases} \tag{D.4}$$

Furthermore, joining the asymptotic expansions for the components of $r_\sigma(z)$, one obtains

$$r_\sigma(z) = 2\sigma g \frac{1+2g\tilde{C}_{1,2}}{(\omega-2\Delta)z} + 2g\tfrac{1+2g\tilde{C}_{1,1}(\omega-2\Delta)-2\sigma(\omega-\Delta)+2g\tilde{C}_{1,2}(1-\sigma\omega)}{(\omega-2\Delta)z^2} + O\left(\frac{1}{z^3}\right). \tag{D.5}$$

This allows expressing $r_\sigma(z)$ as a rational function resulting of the sum of all of its 12 poles, which are simple and match those of $\delta^2 C_\sigma(z)$ (see TAB. 3.2). However, thanks to the multiple symmetries of r_σ, not all of them need to be computed. It is sufficient to compute the three roots $\{z_{\sigma i}\}_{i=1}^3$ of the polynomial $(z^2+2\Delta z+1)(z-\sigma)-4g^2z$, since the remaining ones are given by $1/z_{\sigma i}$, $\zeta(z_{\sigma i})$ and $1/\zeta(z_{\sigma i})$. Thus one can take $f_\sigma(z)$ to be a sum of three simple poles located at $z_{\sigma i}$ and, when assigned with the appropriate residues, $r_\sigma = \mathcal{P}_\zeta\{\mathcal{P}_{inv}\{f_\sigma\}\}$ (equivalent to the Eqn. for r_σ in TAB. 3.2), because the projectors force the correct asymptotic behavior and the rest of the poles on the function. The particular choice of these $z_{\sigma i}$ is intentional, as they correspond with poles of $\delta^2 C_\sigma(z)$ but not of $C_\sigma(z)$, $\delta C_\sigma(z)$ or $\Phi(z)$, which helps to calculate their residues (leading to the expression for $\alpha_\sigma(z)$ in TAB. 3.2).

Comparing the leading order of $r_\sigma(z\to\infty)$ as given by TAB. 3.2 and (D.5) we get

$$g\sigma\frac{1+2g\tilde{C}_{1,2}}{\omega-2\Delta} = (2g\tilde{C}_{1,1}-\sigma)\sum_{i=1}^{3}\alpha_\sigma\left(z_{\sigma i}\right), \tag{D.6}$$

which can be interpreted as two linear equations ($\sigma=\pm1$) with two unknowns ($\tilde{C}_{1,2}$ and $\tilde{C}_{1,1}$). The solutions are the expressions for $2g\tilde{C}_{1,1}$ and $2g\tilde{C}_{1,2}$ in TAB. 3.2.